REPORT DOCUMENTATION PAGE

The public reporting burden for this collection of information is estimated to average 1 hour per response, including the time for reviewing instructions, searching existing data sources, gathering and maintaining the data needed, and completing and reviewing the collection of information. Send comments regarding this burden estimate or any other aspect of this collection of information, including suggestions for reducing the burden, to the Department of Defense, Executive Service Directorate (0704-0188). Respondents should be aware that notwithstanding any other provision of law, no person shall be subject to any penalty for failing to comply with a collection of information if it does not display a currently valid OMB control number.
PLEASE DO NOT RETURN YOUR FORM TO THE ABOVE ORGANIZATION.

1. REPORT DATE (DD-MM-YYYY)	2. REPORT TYPE		3. DATES COVERED (From - To)
03/31/2007	FINAL		4/1/04 TO 3/31/07

4. TITLE AND SUBTITLE

LONG-TERM DURABILITY AND INTEGRITY OF BUILT-IN PIEZOELECTRIC BASED ACTIVE SENSING NETWORK IN STRUCTURES

5a. CONTRACT NUMBER

FA9550- 04 - 1- 0150

5b. GRANT NUMBER

NA

5c. PROGRAM ELEMENT NUMBER

NA

6. AUTHOR(S)

LANZARA, GIULIA; KIM, YUJUN; HA, SUNGWON; YOON, YOUNGKI AND CHANG, FU-KUO

5d. PROJECT NUMBER

NA

5e. TASK NUMBER

NA

5f. WORK UNIT NUMBER

NA

7. PERFORMING ORGANIZATION NAME(S) AND ADDRESS(ES)

LELAND JUNIOR STANFORD UNIVERSITY
651 Serra Street
Stanford, CA 94305

8. PERFORMING ORGANIZATION REPORT NUMBER

28752 AF CHANG

9. SPONSORING/MONITORING AGENCY NAME(S) AND ADDRESS(ES)

AIR FORCE OFFICE OF SCIENTIFIC RESEARCH
875 NORTH RANDOLPH STREET
SUITE 325, ROOM 3112
ARLINGTON, VA 22203-1768

10. SPONSOR/MONITOR'S ACRONYM(S)

AFSOR/PKC

11. SPONSOR/MONITOR'S REPORT

AFRL-OSR-VA-TR-2013-0900

12. DISTRIBUTION/AVAILABILITY STATEMENT

PUBLIC DOMAIN

13. SUPPLEMENTARY NOTES

NONE

14. ABSTRACT

Piezoelectric actuators (PZT) are widely used for Structural Health Monitoring Systems (SHM) and are mostly surface mounted or embedded into a structure with a polymer adhesive layer. The long-term durability and integrity of piezoelectric-based active sensing networks surface-mounted on metallic structures is studied. Numerical and experimental investigations based on nanotechnologies were conducted to characterize and improve the durability, performance and integrity of structures with integrated piezoelectric materials.

A Spectral Element based code (SEM) equipped with a coupled electro-mechanical field solver has been developed to simulate ultrasonic Lamb wave propagation in 3-D structures with built-in piezoelectric sensors. An experimental investigation showed that the integrity of the PZT/structure interface is critical for the performance of PZT actuators. The electro-mechanical coupling between PZT actuators and a hosting aluminium plate was found to vary with the interface debonding.

The design of a carbon nanotube coated piezoelectric actuator (C-PZT) is presented. The C-PZT actuator has its electrode silver paste coating repla

15. SUBJECT TERMS

Built-in Piezoelectric Based Active Sensing Networks, Structures with Integrated Piezoelectric Materials;

16. SECURITY CLASSIFICATION OF:			17. LIMITATION OF ABSTRACT	18. NUMBER OF PAGES	19a. NAME OF RESPONSIBLE PERSON
a. REPORT	b. ABSTRACT	c. THIS PAGE			Fu-Kuo Chang
U	U	U		94	19b. TELEPHONE NUMBER (Include area code) 650-723-3466

Long-term durability and integrity of built-in piezoelectric-based active sensing network in structures

Final Report

March 31, 2007

By
Giulia Lanzara, Yujun Kim, Sungwon Ha, Youngki Yoon and Fu-Kuo Chang
Department of Aeronautics and Astronautics
Stanford University, Stanford , CA 94305

fkchang@stanford.edu
Tel: 650 723-3466

20130919114

SUMMARY

Piezoelectric actuators (PZT) are widely used for Structural Health Monitoring Systems (SHM) and are mostly surface mounted or embedded into a structure with a polymer adhesive layer. The long-term durability and integrity of piezoelectric-based active sensing networks surface-mounted on metallic structures is studied. Main focus is given to the characterization and improvement of the durability, performance and integrity of structures with integrated piezoelectric materials. Both mechanic-based and material-based approaches were conducted.

The mechanic-based approach is based on numerical simulations with a Spectral Element based code (SEM). The SEM method in time domain is first introduced to the field of Structural Health Monitoring where fundamental understanding of Lamb wave propagation and the interaction between diagnostic waves and damage, as well as between built-in, piezoelectric-based sensors and the host structures, are critical. A spectral element-based code equipped with a coupled electro-mechanical field solver and interface program to link with commercial pre/post-processing software has been developed to simulate ultrasonic Lamb wave propagation in 3-D structures with built-in piezoelectric sensors. The code is verified by comparison with experimental results. Performance of the code is examined in terms of solution convergence as compared with finite element method. Furthermore, the potential of this code to be integrated with the diagnostic methods for damage detection is examined.

The material based approach is based on experimental studies performed on a: (a) conventional PZT/structure interface which is a critical element for the performance and reliability of the SHM system; and (b) Carbon nanotube coated PZT (C-PZT) interface which was proposed and developed in this research.

An experimental and numerical study was performed to investigate the effects of interface debonding on the performance of piezoelectric (PZT) ceramic actuators for structural health monitoring (SHM) systems. Interface degradation of PZT actuators may occur over time during the in-service life of the structure compromising the performance and reliability of the SHM system. Energy losses and signal changes should be understood to guarantee the reliability of the SHM systems during the life-time of the structure. Here we present the first systematic study on the performance of PZT actuators with a partially degraded interface. The electro-mechanical

coupling between PZT actuators and a hosting aluminium plate was found to vary with the interface debonding over a wide frequency range affecting the amplitude and phase of the actuator's signal. A signal delay and an amplitude decrease were observed for increasing debonding area, and for different debond shape and location underneath the PZT actuators. These changes were found to be dependent on the actuation frequency with respect to the PZT resonance frequency. The spectral element-based code, developed in the mechanic-based approach, was used to verify the experimental results by simulating the propagation of ultrasonic Lamb waves in an aluminum plate with built-in piezoelectric sensors/actuators.

Conventional PZT ceramics are sandwiched between two silver paste electrodes which have been shown to produce a weak interface bond between the PZT ceramic and the adhesive paste. The design of a carbon nanotube coated piezoelectric actuator (C-PZT) is presented. The C-PZT actuator has its electrode silver paste coating replaced with a carpet of pre-aligned carbon nanotubes (PACNTs). The resulting interface between the C-PZT actuator and a metal substrate is reinforced by a high-density array of oriented CNTs nanoelectrodes (CNTs-NEA). This report presents a unique design method and a potential fabrication process for the integration of uniformly dispersed and oriented CNTs-NEA into the adhesive bondline. The proposed design consists of inserting a Pre-Aligned CNTs (PACNTs) carpet into the adhesive polymer, constraining the carpet to the PZT surface (C-PZT) prior to embedding it into the polymer and making use of the capillarity effect of the CNTs carpet to fully absorb the adhesive polymer. Low- and high-temperature processes were developed to fabricate the C-PZT. The high-temperature process consists of growing CNTs directly onto a polycrystalline PZT, while the low-temperature one consists of transferring aligned CNTs from an alternative substrate onto the surface of a polarized PZT. The microscopic characterization shows that CNTs are fully dispersed and oriented into the adhesive polymer. An investigation was conducted to assess the bondline integrity of a C-PZT actuator mounted on a hosting structure. Mechanical tests were performed to characterize the shear strength of the bondline between C-PZT actuators and the substrate. The test results were compared with shear strengths of the bondlines made of pure non-conductive adhesive and adhesive with randomly mixed CNTs. The comparison showed the PACNTs coating on PZTs could significantly enhance the interfacial shear strength. Through the microscopic examination, it was evident that the ratio between the CNTs length (Lc) and the bond thickness (H) significantly influenced the bond strength of C-PZT

actuators. Three major interface microstructure types and their corresponding failure modes for specific Lc/H values were identified. The study also showed that failure did not occur along the interface between the PZT ceramic element and the CNTs coating.

TABLE OF CONTENTS

Nomenclature

D_i = electric displacement vector components

E_i = electric field vector components

ε_{ij} = strain tensor components

F_i^{ext} = external force vector components

F_i^{int} = internal force vector components

h_q = 1D Lagrange interpolations

K_{ij} = dielectric stiffness tensor components

$\hat{K}_{ij}$ = piezoelectric stiffness tensor components

M_{ij} = X component of the resultant pressure force acting on the vehicle

Q = electric charge

ρ = density

σ_{ij} = stress tensor components

t_i = time index during navigation

u_i = displacement vector components

$\ddot{u}_j$ = acceleration vector components

V = electric potential

I. MECHANICS BASED APPROACH

Even though the Structural Health Monitoring (SHM) system that deduces in-situ "health" through active sensors and real-time data processing has met great success in integrating and automating to perform real-time inspection and damage detection [1,2,3] major challenging issues considered by industry as bottlenecks that prevent the SHM technology from being adequately and effectively implemented in the market remain. Of all the issues, the most critical one is the development of an efficient and accurate analytical tool. Especially, in the case of the elegant system with a built-in, piezoelectric-based sensor network, major concerns about the use of the tool are accurate analysis of the integrated system, as well as the creation of a design architecture, which is necessary for constructing an optimized system in structures that does not rely upon the current primitive trial-and-error approach. However, because a key mechanism in detecting damage in plate-like structures is based on the complicated physics of Lamb wave propagation and its scatter at damage[3], analytic solutions are no longer practically feasible. Numerical approaches have attracted substantial attention as a semi-analytical method of overcoming this complexity and are at the base of the presented study.

I.1. The Spectral Element Method in Time Domain to Analyze Lamb Wave Propagation in Structures with Piezoelectric Sensor Networks

In the field of SHM, numerical methods such as the finite element method (FEM), the finite difference method (FDM) and the boundary element method (BEM) have been employed in the study of how such stress waves behave in structures and interact with defects[4,5,6,7,8].

A common feature of these numerical methods is abbreviated to time and spatial discretizations. The approximations induce inherent errors in the numerical solution. In the case of ultrasonic wave propagation, the major numerical challenge is to minimize numerical dispersion error[9]. If the error of phase and group velocities resulting from the numerical dispersion is accumulated through time and space, the numerical simulation yields useless solutions completely different from the real situation. Therefore, the success of numerical analysis strongly depends on minimization of the error, which requires sufficient discrete spatial

resolution per minimum wavelength. FEM, which is one of the most efficient simulation techniques for obtaining a solution to wave propagation problem in structures, has served as a primary computational tool for understanding stress wave propagation and its scatter at in-homogeneities. Use of the FEM has been encouraged by competitive advantages for modeling of geometrical complexity, material anisotropy and a traction-free boundary condition as compared with FDM and BEM. However, from a practical viewpoint, the diagnostic Lamb waves employed to detect damage in plate-like structures have less than several millimeters as a minimum wavelength. In the case of even non-guided waves, explicit FEM recommends more than twenty elements per minimum wavelength to obtain a solution with a less than 1.0% dispersive error[9]. Thus, finite element analysis for guided wave propagation requires spatial discretizations of less than a few tenths of a millimeter to compute an accurate solution. It follows that FEM for three-dimensional practical problems require impractical computational resources, such as computing time and memory. This is the main reason practical use of FEM in the field of Lamb wave-based SHM has been restricted.

The Spectral element method (SEM) in the time domain is an alternative to the existing numerical methods in the field of Lamb wave-based SHM. The SEM first developed in the mid 1980's[10] is a weighted residual method like FEM. Main features of the SEM are a subdivided whole domain, called elements and high-order interpolation with particular quadrature rules. SEM by use of Lengendre formulation shows an important numerical feature to diagonalize inertia terms, which results in far fewer arithmetic operations. Furthermore, the SEM has an exponential rate of solution convergence and conserves the advantages of FEM mentioned above, which significantly enhances the capability to simulate wave propagation [11]. Consequently, numerical analysis by use of the SEM leads to drastic reduction of the required computational resources. The fields of acoustics and seismology have enjoyed the advantages of the SEM[12,13,14,15]. However, despite its excellent features, a number of researchers with an interest in numerical simulation of Lamb wave-based SHM have essentially ignored the SEM. In the case of time domain analysis, well-developed commercial FEM codes have been preferred due to their accessibility. In our estimation, such trends retard the application of the SEM to the field of SHM. On the other hand, in the frequency domain SEM has been introduced to damage detection technology[16]. The SEM in the frequency domain spectrally formulates finite elements by use of the Fourier synthesis of many infinitely long wave trains of different frequencies[17].

However, in the context of computational efficiency, time domain analysis for wave propagation is intrinsically a better choice. Thus, in this report, the SEM refers to spectral element method in time domain.

Most endeavors to numerically simulate Lamb wave propagation have focused on host structure itself: ultrasonic wave propagation in the structure and interactions with damage. But, the success of such a SHM system relies heavily on a built-in sensor network design and integration of sensors with the structure. In addition, the selection of diagnostic waves and a method of signal interpretation needs to be optimized in a way that the highest damage detection capability can be achieved with the minimal number of sensors to increase the practicality and reduce the cost of these systems. Therefore, it is essential to establish a fundamental understanding of the wave interactions not only between diagnostic waves and damage, but also between sensors and host structures. Achieving this level of understanding requires a numerical modeling for piezoelectric sensors along with host structures.

The purpose of the present work is to introduce the SEM in time domain to the field of Lamb wave-based SHM. Sec. II discusses a spectral element formulation in time domain, based on the coupled electro-mechanical equations for piezoelectric material. As a solution procedure for the coupled equation, the simultaneous employment of an explicit time integration scheme for the semi-discrete dynamic equations and Gauss elimination method for the static electric field is presented. Furthermore, as a pre/post-processor to grant access to the geometrical complexity of host structures, an interface program which links to well-known commercial CAD/CAE code was developed. The interface programs automatically transfer the generated finite element data into spectral element data, and vice versa. In Sec. III, a comparison of the numerical solutions with experimental results verifies the accuracy of the SEM-based code. In Sec. IV, to illustrate the efficiency and accuracy of the SEM-based code, the problem under consideration is stated and then a comparison between the SEM and the FEM is conducted. Sec. V examines the potential ability of this code to detect damage using a sample model. Sec. VI summarizes our conclusions.

I.2. Spectral Element Formulation

In the same way as the FEM, the SEM is an approximation method called the weight residual method[18]. In a fixed rectangular Cartesian coordinate system, let σ_{ij}, u_j, $\ddot{u}_j$, D_i, ρ be the stress, displacement, acceleration, electric displacement and density, respectively. Then, on the basis of the physical equation of equilibrium, the strong form of the boundary value problem known to govern the behavior of a host structure with piezoelectric sensors is stated as follows[19]:

equilibrium equations:

$$\sigma_{ij,i} = \rho \ddot{u}_j \quad \text{in } \Omega^{S+P} \tag{1a}$$

$$D_{i,i} = 0 \quad \text{in } \Omega^P$$

boundary conditions:

$$u_i = \bar{u}_i \quad \text{on } S_u^{S+P} \tag{1b}$$

$$\sigma_{ij} n_i = \bar{t}_j \quad \text{on } S_t^{S+P}$$

$$V = \bar{V} \quad \text{on } S_V^P$$

$$D_i n_i = Q \quad \text{on } S_Q^P$$

where superscripts "S" and "P" mean domain of the host structure and piezoelectric sensors, respectively. Furthermore, subscript "u", "t", "V" and "Q" indicate surfaces prescribed by displacement, traction, electric potential and electric charge, respectively. Summation is implied on the repeated indices unless stated otherwise, and a comma indicates partial differentiation with respect to the coordinate direction. Hereafter, under the assumption of three-dimensional problem, the lower case Roman indices i, j and k are used to indicate the 1, 2 and 3 directions.

Based on the principle of virtual work, the spectral element formulation evolves from transformation of the strong form (1a, b) into the weak form called weight residual formulation[19]:

$$\int_{\Omega^{s+p}} (\sigma_{ij} \delta\varepsilon_{ij} + \rho \ddot{u}_i \delta u_i) d\Omega - \int_{\Omega^p} D_i \delta E_i d\Omega = \int_{S_t^{s+p}} \bar{t}_i \delta u_i dS + \int_{S_Q^p} Q \delta V dS \tag{2}$$

To transfer this weak form into the spectral element equation, the same procedures which formulate a typical finite element equation are followed: the whole domain is sub-divided into many small sub-domains called elements, and then low-order interpolation functions and Gauss quadrature rules are applied to the element. Contrary to the classical finite element

approximation, the SEM approximates the field variables in elements using a high order one-dimensional Lagrange polynomial and its tensor product. For example, the displacement vector can be written as follows[15]:

$$u_i(\xi,\eta,\zeta) = \sum_{p=0}^{N}\sum_{q=0}^{N}\sum_{r=0}^{N} h_p(\xi)h_q(\eta)h_r(\zeta)d_i^{pqr} \tag{3}$$

where ξ, η and ς indicate a local coordinate system, and $h_p(\xi)$ is an N-th order 1D Lagrange interpolation function at (N+1) Gauss-Lobatto-Legendre (GLL) points[15], which show uneven distribution of nodal spaces (see Fig. 1). Use of the Gauss-Lobatto-Legendre quadrature leads the integral Eq. (2) to the coupled spectral element equations, which means mechanical force and electrical charge equilibrium at each node:

$$M_{ij}\ddot{d}_j = F_i^{ext} - F_i^{int} \quad \text{in } \Omega^{S+P}$$

(4a)

$$\hat{K}_{ij}d_j - K_{ij}\phi_j = P_i \quad \text{in } \Omega^{P} \tag{4b}$$

where M_{ij} is lumped mass matrix , $\ddot{d}_j$ is acceleration vector, F_i^{ext} and F_i^{int} are external and internal force vectors, respectively. In the static equilibrium Eq. (4b), d_j and ϕ_j are nodal displacement and electric potential vectors. Furthermore, P_i is electric charge vector, and $\hat{K}_{ij}$ and K_{ij} are the piezoelectric stiffness matrix and the dielectric stiffness matrix, respectively.

Due to Legendre formulation, the mass matrix in Eq. (4a) leads to a naturally diagonal matrix. Furthermore, in the context of features for wave propagation, the explicit time integration scheme, such as the central difference method, is the best choice for calculating the ordinary differential Eq. (4a) in the time domain. As a strategy for solving the coupled Eq. (4a,b) simultaneously, in each time step, the mechanical fields such as acceleration, velocity, displacement and stress are estimated on the basis of electric potential and mechanical fields obtained from the previous time step. And then using the estimated displacements and the Gauss elimination algorithm, the static equation for the electric field (4b) provides the new electric potentials at the current time step. At the next time step, the obtained displacements and electric potentials are used again as the field variables of the previous time step. All these procedures are iterating to the end-time step.

I.3 Code Verification

I.3.1 Statement of the Problem

A square aluminum alloy plate (thickness = 1.02 mm, width and height = 508 mm), as shown in Fig. 2(a), is used to perform the SEM-based code verification using comparison to experimental results. Four identical piezoelectric transducers are mounted on one side of the plate as shown in Fig. 2(a). Table 1 shows location of the piezoelectric transducers on the plate.

The electro-mechanical properties of the piezoelectric materials (APC850) are available from American Piezoceramics, Inc.[*]. The piezoceramic element used is a disk with 0.25 mm thickness and 6.35 mm diameter. The experiment is made using pitch-catch setup, in which one of the transducers acts as an actuator to generate Lamb waves and the other transducers receive the propagating Lamb waves. The peak voltage of the excitation is kept at 50 volts. In the experiment, PZT 2 as an actuator excites a five peak tone-burst wave with a center frequency of 100 kHz as shown in Fig. 2(b).

According to Lamb wave dispersion equation[3], at this frequency-thickness value, there are only fundamental symmetric and anti-symmetric mode due to excitation below the cut-off frequency of the first anti-symmetric mode. The more dispersive anti-symmetric wave mode has a wavelength of 9.5 mm, and the symmetric wave mode has a wavelength of 53.0 mm.

In numerical analysis, spatial resolution on numbers of node per minimum wavelength is a key factor to obtaining accurate solutions. The mesh configuration is shown in Fig. 2(c). In this case, the 3D spectral element has 5 mm x 5 mm x 1 mm as maximum size and 5th order Lagrangian interpolation in the element. The total number of nodes and elements are 1,656,360 and 11,040, respectively. This configuration gives about ten nodes per wavelength along the propagation direction. The reason such resolution is employed is discussed in Sec. IV, below. In order to sub-divide the whole domain into elements as shown in Fig. 2(c), the FEM-based commercial code ABAQUS/CAE[†] is used as a pre-processor to discretize complex geometry of structures. The finite elements formed out of the pre-processor are turned into the spectral element using the author's interface program. As a boundary condition, the plate is assumed under traction-free condition. Furthermore, the excitation in the form of electric voltage is

---

[*] American Piezo Ceramics, Inc (http://www.americanpiezo.com)

[§] ABAQUS, Inc (http://www.hks.com)

applied to nodal points on the top surface of actuator PZT 2 in steps with respect to time, as shown in Fig. 2(b). All calculations are performed using a personal computer: Pentium IV 2.66 GHz CPU, 512 MB RAM and Compaq Visual Fortran 6.5[‡].

1.3.2   Results and Discussions

The SEM-based code quite accurately simulates the response of sensor measurements in a pitch-catch mode as shown in Fig. 3, where the measured sensor signals were compared with the simulated results in response to a five peak wave excitation generated at PZT 2. As previously stated, only two fundamental modes are observed in this figure. Furthermore, the anti-symmetric mode with relatively slower velocity and larger signal strength shows more dispersive features as compared to the symmetric mode. The good agreement between experimental results and numerical solutions verify that the SEM-based code with coupled explicit time marching and static solving scheme is capable of simultaneously solving the coupled electro-mechanical fields for Lamb wave simulation. The efficiency and accuracy of this method is discussed in the next section. In this code, the sensor output as volts is the mean of the nodal voltages obtained from solving the coupled Eq. 4(a, b) on all nodes on the PZT sensor surface.

I.4 Code Performance

I.4.1 Statement of the Problem

In order to study the efficiency and accuracy of the spectral element analysis for ultrasonic Lamb wave propagation, the solution convergence rate through the increase of the spatial resolution is examined by comparing with the finite element analysis performed by the author's explicit FEM code. Both of the author's codes employ the same algorithm to solve the coupled electro-mechanical field. The only difference between the two codes is the fact that the SEM uses various high order interpolations and GLL quadrature, whereas the FEM is based on linear interpolation and usual Gauss quadrature, as discussed in Sec. II. Thus, decreasing finite element size is the only way to improve the spatial resolution, whereas, in addition to decreasing spectral element size, the use of higher order interpolation enhances the resolution. Furthermore, there are two integration schemes in FEM. In the context of computational cost, a reduced integration

scheme for explicit FEM is a better choice than full integration. In contrast, the full integration scheme is better than the reduced integration in terms of solution accuracy[9]. In this study, both reduced and full integration schemes are employed to investigate the two aspects of efficiency and accuracy.

As a test model, let's assume there is thin aluminum plate with two surface mounted piezoelectric transducers as illustrated in Fig. 4(a). The thin plate has a sufficiently large dimension in the X_2 direction compared with the dimensions in the X_1 and X_3 direction (508 x infinity x 1.02 mm). The piezoelectric transducers with X_3 poling direction are running parallel to the X_2 direction (6.35 x infinity x 0.25 mm). Therefore, this example can be considered to be in the state of plane strain deformation under uniform voltage input on the transducer upper surface, wherein the displacement in the X_2 axis disappears identically to zero. This simplification makes it easy to examine the effect of spatial resolution in numerical methods without loss of generality. Typical mesh configurations of FEM and SEM for the plane strain problem are shown in Fig. 4(b) and 4(c). For the sake of visualization, the figures are enlarged nearby one piezoelectric transducer. Furthermore, the SEM-based and FEM-based codes have only a three-dimensional element. To embody the plane strain state using the 3D element, a very thin element dimension along the X_2 direction is assumed and all X_2 direction degrees of freedom are constrained. Using one of two piezoelectric transducers as an actuator, a five peak tone-burst wave with a center frequency of 100 kHz, was excited.

I.4.2 Results and Discussions

The profile of sensor signals is shown in Fig. 5(a), in which a smaller strength symmetric mode is followed by a higher strength anti-symmetric mode. The SEM-based solution is in quantitative accord with FEM based results. However, in the context of numerical dispersion error, while the solutions match almost perfectly for the fundamental symmetric mode, a small discrepancy of phase/group wave velocities is observed in the slower fundamental anti-symmetric mode, as shown in Fig. 5(b). In order to investigate the efficiency and accuracy of numerical methods, the discrepancy versus the spatial resolution is examined from quantitative viewpoints as shown in Fig. 6. In this figure, the SEM exhibits on exponential convergence rate as compared with the FEM. In terms of the solution convergence, the SEM has an excellent

advantage over the FEM in simulation of the ultrasonic Lamb wave propagation. Furthermore, as shown in this figure, reduced-integration based FEM underestimates the group velocity, and full integration-based FEM overestimates it. Both FEM solutions asymptotically converge to a solution as the resolution increases. The solution as the element size goes to zero ($h \rightarrow 0$) is easily calculated by Richardson extrapolation[20]. According to the mathematical approach for FEM[21], the numerical dispersion error in linear FEM is decreases with h^2. Under the assumption of asymptotic error expansion, the improved solution of the arrival time obtained from finite element analysis is calculated as follows:

$$Y(0) = \frac{4Y(h/2) - Y(h)}{3} + O(h^p), \quad p > 2 \tag{5}$$

For full integration:

Y(h)=115.88, Y(h/2)=116.30 => Y(0) = 116.44

For reduced integration:

Y(h)=116.65, Y(h/2)=117.280 => Y(0) = 116.44

The solution accuracy of SEM and FEM is estimated on the basis of the value shown in Table 2. To obtain a solution with less than 0.5% dispersive error, the FEM requires more than forty nodes per minimum wavelength. Table 3 shows the comparison of computational resources. The SEM reduces the computational memory by more than a factor of twenty in terms of total nodal numbers, compared with the FEM. Furthermore, the FEM costs more than ten times the computational time, compared with the SEM.

I.5 Code Feasibility to Damage Detection

I.5.1 Statement of the Problem

To monitor the scattered Lamb wave induced by the crack, a damage detection procedure using a typical pitch-catch and pulse-echo method is performed with the aid of the SEM-based code. Consider the same aluminum plate, as previously mentioned in Sec. III. In addition, the plate has a through-thickness circular hole (center at X_1= 237 mm and X_2=279 mm; 10 mm diameter) and a through-thickness crack (4, 8 or 12 mm) originating from the hole edge as seen in Fig. 7(a). The Lamb wave sensitivity to cracks strongly depends on the excitation frequency. A five cycle tone-burst waveform with a driving center frequency of 450 kHz is used for the

actuation signal as shown in Fig. 7(b). In this frequency range, the symmetric Lamb wave mode, which is more sensitive to the presence of through-thickness cracks in isotropic structures than the anti-symmetric wave mode[3], has a much higher amplitude as compared with the anti-symmetric mode. Furthermore, the wavelength of the symmetric mode is about 12 mm, which is sensitive enough to detect 4 mm cracks. A typical mesh configuration is shown in Fig. 7(c). The maximum 3D element size is 5 mm x 5 mm x 1 mm. In addition, the Lagrange interpolant in each element is 5th order. According to the discussion in Sec. 4, in terms of the symmetric wave mode, this nodal resolution reduces the dispersion error to under 0.05%. Total number of nodes and elements are 1,671,720 and 11,141, respectively.

I.5.2 Results and Discussions

The SEM-based code is able to embody the pulse-echo concept in addition to the typical pitch-catch method. In terms of the pulse-echo algorithm, the programmed electric voltage first excites a PZT actuator, and then the function as an actuator is artificially stopped at a fixed time step. Secondly, the element as a sensor starts sensing a reflected wave from damage and boundaries. Fig. 8(a) shows the sensor signals based on the pitch-catch method when PZT2 and PZT4 are used as an actuator and sensor, respectively. The first arrival symmetric wave mode shows higher signal strength as compared with the anti-symmetric wave mode. In terms of the symmetric wave mode, this driving frequency greatly enhances the signal-to-noise ratio compared to the case of 100 kHz center frequency, as shown in Fig. 3. Fig. 8(b) is the sensor signal when PZT2 and PZT4 are used as an actuator/sensor, respectively, based on the pulse-echo method. The time-of-flight of the first/second arrival waves confirms that it is a symmetric wave mode originating from the hole/crack and plate edge, respectively.

In order to clearly identify only the scatter waves induced by the crack, both wave propagation simulations for the plate (shown in Fig. 7) with and without the crack are performed and the results are numerically subtracted. Fig. 9(a) describes the forward scattered signals obtained from path PZT2-PZT3. The scattered signal strength induced at a relatively longer crack is higher. Furthermore, there is no phase shift in the first arrival scattered signals because the crack is located at a short distance from the direct wave path. Fig. 9(b) shows the simulation result of the scattered wave due to a crack when PZT2 is used as a pulse-echo element. The scattered waves, which arrive faster as increases the crack length, confirm that it originates from a crack.

The wave developments at different time frames in the model with an 8 mm crack are shown in Fig. 10. To draw the wave developments, the interface program is used, which transfers the SEM-based output solution into the input data for the commercial software Tecplot[§]. It's shown that the symmetric and anti-symmetric waves are generated at PZT2 actuator and propagated outward. These figures show the symmetric waves partially reflected and transmitted to the backward and forward directions, respectively, after the first arrival at the hole/crack. Furthermore, the faster symmetric waves totally reflected at the plate boundary are mixed with the slower anti-symmetric waves. The wave mixtures induce the complicated wave development as time progresses. Fig. 11 shows only the propagating scattered waves from the crack tip at 20 μsec and the scattered wave propagating to neighboring sensors at a later time. In order to easily observe the scattering at the crack, Fig. 11 (a) is enlarged nearby the hole. These figures clearly show that the scattered signal is induced at the crack as mentioned earlier. This offers the potential ability of this SEM-based code to detect damage. Furthermore, The SEM-based code will be used to optimize key parameters such as sensor shape, size, locations and input diagnostic waveform to achieve the maximum damage detection capability with a minimal number of sensors.

I.6 Interface Adhesive Layer Effect

In section I.3, the SEM code was verified without modeling an interface adhesive layer at 100 kHz excitation frequency which is much lower than the resonance frequency of piezoelectric transducers used in the experiment. In the case of an excitation frequency close to the resonance of the piezoelectric transducer, the effects of the adhesive layer are much more prominent. As a result, the simulation doesn't match well with an experimental result. Fig. 12 shows the SEM simulation and an experimental result at 400 kHz excitation with the same configuration as Fig. 3 (a). The experimental sensor signal has larger amplitude and more peaks compared with the SEM simulation. It is assumed that low stiffness of the adhesive layer (about 5% of aluminum) cannot constrain the resonance behavior of piezoelectric transducer, thus causing these phenomena.

[§] Tecplot, Inc (http://www.tecplot.com)

To verify this assumption, 2-D plane strain model as shown in Fig. 13 is used because 3-D model requires a lot of computation and memory due to an extremely small mesh size for the thin adhesive layer. The 2-D model has same propagation distance as the 3-D model. A model without adhesive is compared with those with a 50μm and 100μm adhesive layer. As the thickness of adhesive layer increases, larger amplitude and more peaks occur in both symmetric(S0) and anti-symmetric(A0) mode similar to the 3-D results shown in Fig. 12.

To achieve accurate SEM simulation without modeling adhesive layer for 300 KHz and 400 KHz excitation, a piezoelectric transducer with a smaller diameter which has higher resonance frequency should be used. Also, more study on adhesive layer modeling is required to simulate wave propagation with an excitation close to the resonance frequency of a piezoelectric transducer.

II.   MATERIAL BASED APPROACH

One of the major concerns in aeronautical structures is their maintenance to guarantee safety, performance and reliability during manufacturing and the in-service life of the structure. This issue is usually approached with standard non-destructive inspection methods which can only access limited areas of the structures and have high maintenance costs. Structural Health Monitoring (SHM) systems are a recent alternative approach that has the potential to satisfy scheduled and non-scheduled inspection/maintenance tasks in a cost-effective manner. At the core of SHM technology is the development of self-sufficient systems utilizing built-in distributed sensor/actuator networks that are integrated with the host structures for the continuous monitoring, inspection and damage detection with minimal labor involvement. The aim of SHM is not only to detect structural discrepancies and determine the extent of damage, but also to determine effects of structural usage and provide an early indication of physical damage. Piezoelectric (PZT) based SHM systems are among the most widely used for active and passive control systems, and have PZT sensors/actuators permanently bonded to the structure with an interfacial adhesive layer which has the primary role of coupling the PZT ceramics to the structure for stress/strain transfer[22,23]. The PZTs network becomes part of the structure and therefore subjected is to the same environmental conditions as the structure (such as temperature variations, vibrations, strain, load, chemical attack etc.). The PZT sensors/actuators bondline (i.e. bonding layer at the interface with the host structure) was found to crack and debond under environmental stresses causing a loss of performance in the SHM system[24,25,26,27]. A debonding or a crack in the interface will reduce the control capabilities and so its effects should be included in the SHM algorithms. However the response of PZT sensors/actuators with a degraded interface is still not fully understood.

Here are presented the first systematic study to characterize the performance of PZT actuators with a degreaded interface and a novel interface design based on carbon nanotube technologies.

II.1 Influence of Interface Degradation on the Performance of PZT Actuators

Today it is not possible to include, in the algorithms, the effects of an interface debonding or crack. This is because of lack of experimental studies that address the effects of debond on the response of PZT actuators, and because of very little analytical works that have been done to include in the models the PZT actuator bondline. Most analytical studies in fact use electromechanical impedance and wave propagation techniques and disregard the interfacial adhesive layer[28, 29, 30, 31,32,33]. Kim and Chang[34] have proposed an effective Spectral Element Method (SEM) based code to simulate the response of built-in PZT sensors/actuators in structures considering the interfacial adhesive layer. It was shown that the performance of PZT actuators is affected by the interface thickness. This behavior was found to be sensitive to the actuation frequencies relative to the natural resonance frequency of the PZTs, which is in agreement with experimental[32] and numerical results[35]. Fewer investigations consider damage in the actuator/sensor bondline[36, 37]. Kumar and Ikeda interpreted a PZT debonding as a reduction of the electro-elastic coupling stiffness[38]. However, in order to be able to correctly ascertain the performance and reliability of SHM systems during its entire life-time, it is first necessary to clearly understand the response of PZT sensors/actuators with a degraded interface.

Presented here is a systematic experimental and numerical study of the effects of interface degradation (debonding) for PZT actuators mounted on a metal structure. Main focus is given to the debonding size, extension, shape and location in the interface. It was found that the electro-mechanical coupling between PZT actuators and the hosting structure is strongly affected by a partial debonding and that this effect is influenced by the actuation frequencies with respect to the natural resonance frequency. These results can be used as a template in SHM algorithms and guarantee the reliability of built-in systems during the in-service life of a structure.

II.1.1 Problem Statement

Interface degradation may occur over time in the bondline between piezoelectric (PZT) actuators and the hosting structure, compromising the performance and reliability of Structural Health Monitoring (SHM) systems. In Figure 14 is shown a typical bondline configuration for a PZT actuator bonded to a metal plate with a thin conductive adhesive layer.

The objective of the study is to characterize the effects of local debonding/degradation of the interface on sensor data integrity and reliability under dynamic excitation in acoustic-ultrasound range. The study was performed both experimentally and numerically.

II.1.2 Experimental Study

An experimental investigation was performed to characterize the influence of interface degradation on the performance of PZT actuators surface mounted onto a metal structure. Major focus was given to the effects of bondline degradation on the signal of PZT actuators. The effects of degradation size, shape and location underneath the PZTs were investigated.

II.1.3. Test Setup and Procedure

The analysis of the bondline integrity of PZT actuators was performed by mounting PZTs onto a metal structure. The electro-mechanical coupling between the PZTs and the structure was achieved with an interfacial conductive adhesive layer. In Figure 15 is shown a scheme of the test setup. Five PZT ceramics discs were bonded to 520.6mm side square aluminium (Al) plates in the pattern shown in Figure 15. The center disc was used as the sensor and the four peripheral discs were used as actuators and placed at a distance of 255mm from the sensor. The peripheral discs were set at a distance of 80mm from the edges of the plate to avoid undesired boundary effects in the study. The PZT sensor disc was fully bonded to the plate as shown in Figure 14, while the actuator discs were bonded to the plate according to specific interface designs discussed in section II.1.4. The PZT sensor/actuators and the metal plate were simultaneously grounded and connected with a Smart Suitcase (Acellent Technologies) which had a built-in function generator and amplifier. A narrow band five-burst diagnostic signal was generated from each actuator by applying a voltage across the thickness of the PZT discs. Expansions and contractions were generated within the PZT actuators, transferring elastic wave energy (Lamb waves) into the substrate. These waves propagated into the Al plate and were transmitted to the PZT sensor which expanded and contracted giving rise to a voltage across its thickness. The voltage was detected and analyzed. The five cycle tone-burst waveforms were set with center frequencies ranging from 100KHz to 500KHz.

II.1.4 Bondline Designs

The interface degradation was investigated as partial debonding of PZT actuators from a host substrate. For this purpose, several interface designs were chosen in order to represent different bonding conditions. Particular attention was given to the debonding area, shape and location underneath the PZT actuators. A PZT disc (9.5mm in diameter and 1.24mm thick) fully bonded to a supporting Al plate had a total contact area of $17.7mm^2$ (A_1) with a 50μm thick adhesive interface. This was taken as the reference PZT bondline for the study.

Two sets of samples were designed to investigate the effect on the PZT disc signals due to: 1) interface debonding and debonding area increase (Set I), 2) debonding shape and location (Set II). In Figure 16 is the schematic of Set I. These samples are representative of PZT actuators with a partially degraded interface and were designed to investigate the coupling effect due to an increase in interface degradation (debonding area increase). For this purpose, an asymmetric side debonding, starting from an edge of the PZT interface and propagating toward the center was chosen as the case study (Figure 16). Debonding areas were set to: 10% (contact area A_2 $15.39mm^2$), 30% (contact area A_3 $11.97mm^2$), and 50% (contact area A_4 $8.55mm^2$), with respect to the A_1 contact area in a fully bonded PZT. The effect of debonding shape was studied by means of samples in Set II, where a constant 20% debonding area (contact area A_5 $13.58mm^2$) was varied in shape and the fully bonded PZT was used as a reference actuator. The debonding shapes are shown in Figure 17 and are defined as: 1) Type S2: centered debonding, 2) Type S3: two side debonding and, 3) Type S4: edge debonding. The center debonding was located in the center of the PZT actuator, the two side debonding started at two opposite sides of the bond interface and propagated toward the center, and finally the edge debonding involved the entire perimeter of the PZT bondline. The interface thickness in Set I and Set II was kept constant at 50μm.

II.1.5 Bondlines Fabrication

PZT discs were bonded to the Al plates with CW2400 two-part conductive epoxy adhesive (ITW Chemtronics) in order to maintain electrical contact with the metal structure. Isopropyl alcohol was used to clean the bonding areas after slightly polishing the Al surface to remove the superficial oxide layer on the plate. The major issue in the fabrication process was the control of the contact areas. A Teflon mask was used for this purpose and was cut in the shape of the

desired debonding area. The mask was applied onto the PZT surface before spreading on the conductive adhesive. The PZT was then placed onto the Al plate and was bonded by applying a uniform pressure. The adhesive was left to cure for several days under room temperature conditions.

II.1.6. Numerical Study

A spectral element method (SEM)[34] was used to analyze the interface degradation of piezoelectric sensor/actuators operating in acoustic-ultrasonic frequencies. The main feature of the SEM code is that it adopts high-order interpolation functions with particular quadrature rules enhancing the solution convergence rate and reducing the required computational time and memory space[34].

The effects of interface debonding were studied with a model based on a simplified 2-D strain condition as shown in Figure 18a. The model was based on a thin Al plate with surface mounted piezoelectric discs. The 1mm thick aluminum plate has sufficiently large dimensions in the x_2 direction compared with the dimensions in the x_1 and x_3 directions. The piezoelectric sensors with the x_3 poling direction are running parallel to the x_2 direction. Therefore, this study can be assumed to be in the state of plane strain deformation under PZT actuation, wherein the displacement in the x_2 axis disappears. To embody the plane strain state using the 3D element, very thin element dimensions along the x_2 direction were assumed and all x_2 direction degree of freedom were constrained. The PZT ceramics were assumed to be 6mm wide (x_1 direction) and 0.25mm thick (x_3 direction). Five node numbers through thickness are set and then the numbers increase along the wave propagation direction. The bondline thickness was set to 100 μm. In all cases, sensors, actuators, inputs, and structural conditions were identical in all the simulations, except that an asymmetric debonding (Figure 18b) was located in the actuators bondline with 0%, 10%, 25%, 33% and 50% debonding areas. A five cycle tone-burst waveform with a center frequency ranging from 100 kHz to 500KHz was used to actuate the PZT and generate a fundamental symmetric and anti-symmetric Lamb wave in the aluminum plate that was detected by the PZT sensor.

The electro-mechanical properties of the piezoelectric material type 850 were available from American Piezoceramics Inc., and typical Al properties (Young's Modulus = 69 GPa, Poisson's ratio = 0.33, density =2700 kg/cubic meter) were used for the numerical computation.

Calculations were performed using a personal computer: Pentium IV 2.66 GHz CPU, 512 MB RAM and Compaq Visual Fortran 6.1. The Young's modulus, Poisson's ratio and density of the conductive epoxy were assumed to be 2.66 GPa, 0.33 and 1100 kg/ cubic meter respectively.

II.1.7 Results and Discussion

Reported here is the experimental and numerical response of PZT actuators with a degraded interface, under dynamic excitation in acoustic-ultrasound range. It is shown that energy losses and signal changes may occur due to interface degradation and that these changes depend on the actuation frequencies in respect to the PZT resonance frequency. These results suggest that it is important to consider the interface degradation to guarantee the reliability of the response in SHM systems. Here the interface degradation is assumed to be a local debonding of the interface between the PZT ceramics and the hosting structure. The effects of debonding extent, location and shape underneath PZT actuators are also presented.

II.1.7.1 Experimental Results

Figure 15 shows a scheme of the experimental test setup. The Al plate is simply supported at its base and insulated from external vibrations. The PZT sensors and actuators were mounted on the plate with the pattern described in section II.1.3 and according to the interface designs described in section II.1.4. A top view image of a PZT disc is shown in Figure 19b. Typically, PZTs are sandwiched between silver paste electrodes on each side which supply a uniform charge across the surface of the PZT. The bottom electrode layer was electrically connected to the grounded Al plate with a conductive adhesive interface which was designed and fabricated with the procedure described in section II.1.4 and II.1.5. The upper electrode was soldered and connected to the Smart Suitcase. The Al plate was grounded. In Figure 19c is a Scanning Electron Microscope (SEM) image of a conductive adhesive interface which is made out of two mixed parts (part A and part B). An Electron Microscopy characterization was performed to measure the interface thickness of the PZT actuator surface mounted to the Al plate. For this purpose, a sample specimen was built and cut along a vertical plane (orthogonal to the bondline plane) to have a direct view of the interface. In Figure 19b is an SEM image of the cut specimen which shows from the top to the bottom: a) the PZT actuator, b) the interface and, c) the Al plate. The reference interface was measured to be 7μm thick. The study involved analyzing the sensor

signals (PZT sensor in the center of the plate as in Figure 18) due to independent actuations of the 4 neighboring PZT actuators.

II.1.7.1.1 Effects of the Interface Debonding

The effect of a debond and of the debond extension underneath an actuator on the actuator's ability to generate and propagate diagnostic signals was studied. An asymmetric interface debond was found to lead to energy losses which are dependent on the extension of interface damage and on the actuation frequency.

The reference actuator signal was compared with the signals generated by actuators having a constant thickness and a varying contact area. The set of samples in the analysis was Set 1 (Figure 16). An asymmetric side was growing toward the center of the PZT disc reaching a maximum 50% debonding area. In Figure 20 are reported the results of tests performed on PZTs having a 10%, a 30% and a 50% debonding area (interface: Type A_2, Type A_3 and Type A_4) for an actuation frequency of 300KHz. The signal's phase was affected by a debonding area increase. A signal delay was observed with increasing debonding area as shown in Figure 20, which reached an 18% delay in the case of 30% debonding. The sensor signal amplitude was observed to decrease linearly with increasing debonding area reaching a 62% decrease for a 50% debonding. The amplitude change was also found to be sensitive to the selected actuation frequency. The analysis for a frequency range of 100KHz to 500KHz is reported in Figure 21. A 100% amplitude in the graph corresponds to a fully bonded PZT actuator (no debonding, contact area A_1) and is compared with amplitudes of PZT actuators with 10%, 30% and 50% debonding area (A_2, A_3, A_4). The test results show that there is a linear signal amplitude decrease for higher actuation frequencies (250KHz and 300KHz) reaching a 73% amplitude decrease at 250KHz and 50% debonding area (PZT-Type A4). The response was different at lower actuation frequencies (between 150KHz and 200KHz). For a 30% debonding and frequencies below 300 kHz within the selected test range, the actuator suffered most significantly from energy loss in signal transmission. At low frequencies the signal amplitude decreased until it reached a 30% debonding size. This phenomenon is suspected to be associated with the natural resonance frequency of the bonded actuators which in this case is 210KHz. When a PZT actuator is fully bonded to a thin metallic structure (e.g. contact area A_1), shear strain motions are predominant and generate Lamb waves within the hosting structure. However, out-of-plane motions are also

involved and are transferred into the structure due to energy coupling and boundary effects. The result is a Bessel-like vibration mode. The behaviour changes when a PZT actuator is partially debonded (e.g. contact areas A_2, A_3 and A_4). In these cases, the bonded areas still follow a Bessel-like vibration pattern, while the motion in the debonding area is characterized by a modal vibration similar to the one of a cantilever. This affects the displacements in the debonded region which are higher in comparison to the ones of the bonded area and result in stress concentration at the singular points as later discussed in section II.1.7.2. The reduced coupling between the debonded PZT actuator and the structure results in a reduced displacement in the bonded region and so in a reduced signal amplitude.

II.1.7.1.2 Effects of Debonding Shape

In section II.1.7.1.1 it was shown that a partial debonding of the interface of a PZT actuator surface mounted on a thin Al plate affects the sensor signal amplitude and phase for a wide frequency range. Here is discussed the effect of different debonding shapes and location underneath the PZT actuators on the signal. The samples in the analysis are the ones of Set II where the debonding area was set to 20% while the shape and location underneath the actuators was made to change (Figure 17). The test was performed with the same approach described in section II.1.7.1.1. The sensor signals were recorded and compared with the reference signal of a fully-bonded PZT actuator. In Figure 22 is shown the effect of different debonding shapes for a given debonding area. The plot shows the measured sensor signals corresponding to an actuator input at 250 KHz which is around the resonance frequency of the PZT actuator. It is clear that the amplitude of sensor signals was affected by the debonding shape, but the phase of the signal did not change as obviously as the amplitude. The highest phase amplitude change was observed to be only 0.75% for a side debonded PZT actuator. Figure 23 shows the effect of debonding on the sensor signal amplitude at a 250 KHz actuation frequency. The signal amplitude of the reference PZT is taken as 100% (reference) and the amplitudes of the other debonded PZTs are plotted against this reference value. The edge debonding induced the smallest amplitude drop (12%) among the three debonding shapes compared. Actuators with debonding from two opposite sides suffered the most significant decrease in amplitude (24%) probably due to stress concentrations at the singular points (see section II.1.7.2).

II.1.7.2 Numerical Study and Comparison with the Experimental Analysis

The results of a simplified two-dimensional SEM model, which was used to validate the experimental results by studying the effect of a debonding underneath the PZT actuators, are presented here. An asymmetric side debonding, extending toward the center of the PZT actuator was investigated. In Figure 24a is shown the sensor signal over time for a fully bonded PZT and partially debonded PZTs with 10%, 25%, 33% and 50% debonding areas actuated at a 100KHz frequency. The sensor signals changed in terms of amplitude and phase when the PZT actuators were debonded from the Al plate, according to the experimental results. The signal amplitude varies with increasing asymmetric debonding size. It is also shown that the observed phenomenon depends on the actuation frequency. This can be seen by comparing Figure 24a and Figure 24b that show the plot of signal amplitude vs. time in the case of a 100KHz and 500KHz actuation frequency, respectively. In this case, an increase in sensor signal strength with a 50% debonding size was observed at a 500KHz frequency. This is in agreement with the experimental results discussed in section II.1.7.1.1, where it was shown that both amplitude and phase of the sensor signal were strongly affected by the increase in the debonding area and that these changes were also sensitive to the excitation frequencies. In particular, the experimental results clearly showed the decrease of sensor signal with an increase in the debonding area. However, at some excitation frequency ranges, after a drop of the sensor signal strength caused by the debonding, a further increase of the debonding area resulted in an enhancement of the sensor signal strength. The numerical simulation confirmed such behaviour as shown in Figure 24b, where, with increasing debonding size, the sensor signal strength first decreased and then increased.

In order to clearly observe the changes in the sensor signal strength because of the interface debonding, maximum amplitude of the sensor signal measured against the asymmetric debonding size is described in Figure 25. The maximum amplitudes are normalized by the maximum amplitude of a fully-bonded PZT (0% debonding area). The decrease/increase trends of the maximum amplitude with debonding area size are shown in excitation frequency ranges between 100kHz and 500kHz, according to the experimental analysis. At excitation frequencies lower than the PZTs natural frequency, the numerical trend is in agreement with the experimental results showing a drastic drop in the maximum signal amplitude for a 33% debonding area and showing a maximum amplitude increase for higher debonding areas (50%

debonding). This numerical result can be observed in Figure 25a, 25b and 25c between 100KHz and 300KHz and can be compared with the experimental study in Figure 21 (between 150KHz and 200KHz). This frequency range offset between the numerical and experimental result is due to the fact that the natural resonant frequency of PZTs settles at 210KHz and 330KHz for the experimental and numerical study respectively.

Furthermore, the numerical simulation showed that at frequencies 100KHz and 200KHz much lower than the resonance frequency (330KHz), the maximum sensor signal amplitude for a 50% debonded PZT is amplified with respect to the fully bonded PZT. While for frequencies closer to the resonance frequency (300KHz and 400KHz), a 50% debonding area is characterized by a signal amplitude lower than the fully bonded PZT (0% debonding). This result is in agreement with the experimental data, where the signal strength of a 50% debonded PZT excited at a frequency near the resonance frequency (210KHz) is lower than the signal strength of the fully bonded PZTs (0% debonding). At frequencies higher than the resonance frequency, both experimental and numerical data show a maximum signal strength decrease. However, in these cases it was observed that the numerical data predicted a different "trend" in comparison with the experimental data. A maximum drop of signal strength for low debonding areas (10%) was recorded but further increase in the debonding area showed an increase of the signal strength. The different trend between the experimental and numerical data at frequencies higher than the resonance frequency, is explained by the fact that as the wavelength of the stress waves becomes closer to (in the order of magnitude) or smaller than the size of the actuators and sensors, the interface properties can have a significant effect on the responses of sensors and actuators. The SEM model used in this analysis was based on a simplified two-dimensional model which loses accuracy at higher frequencies.

As discussed in section II.1.7.1.1, a PZT with a debonded interface can be interpreted as a complex structure with a region that is fully bonded to the structure and another region that is debonded and behaves like a suspended cantilever. In Figure 26 is reported the stress analysis of a 50% asymmetric debonded actuator interface. The analysis was performed with the SEM-based code. In Figure 26a is shown the actuation signal (voltage) vs. time at 200KHz. The analysis was performed at 12μsec which is highlighted in the signal curve. In Figure 26b and 26c are shown the inter-layer shear stress distribution and the normal stress distribution, respectively. This result clearly shows that stress concentrations occur at singular points like the bonded free edges.

These stress concentrations may be the cause of energy losses and thus of a strength reduction in signal amplitude.

II.2 Carbon Nanotubes Coated Piezoelectric Actuators

Recent development of sensor technology for structural health monitoring (SHM) requires bonding or integrating sensors onto the structures. Bondline integrity of these sensor interfaces critically affects the performance of the underlining structural health monitoring systems. Piezoelectric ceramics (PZT) are widely selected for such an application[39,40] and are normally coupled to the structure through a thin adhesive layer. Piezoelectric elements could be used as both an actuator to expand and contract generating elastic waves into the structure and as a sensor to measure dynamic strains of the structure. Obviously, a loss of interfacial integrity between the PZTs and the structure would result in a reduced sensor/actuator signal strength, which can have a detrimental effect on the SHM systems[41].

Normally a PZT is sandwiched between two silver paste layers (SP) and bonded to the structure with a thin polymer adhesive (Figure 27) layer. The SP layers play the role of electrodes that are used during the polarization and the inservice life of the PZT actuators. PZTs are normally polycrystalline in nature, which means they do not have piezoelectric properties in their original state. The piezoelectricity is normally induced in these materials via a poling procedure which consists of applying high dc electric fields using the SP layers as electrodes. The SP electrode (about 6μm thick) is made out of silver and glass particles. The paste is spread onto the PZT and fired on at high temperatures (560°C). The problem is that the resulting electrode is weakly bonded to the PZT and can easily be peeled off causing debonding of the PZT from its supporting substrate. Therefore it is desirable to reinforce the interface between the PZT and the SP electrode.

Furthermore, the latest sensor network technologies are working toward the integration of smaller and smaller actuators and sensors (down to the microscale) into large networks[42,43]. Toughening or reinforcing the bondline strength of microscale sensors and actuators on structures is becoming a major challenge.

It has been demonstrated in the literature[44] that the mechanical properties of materials at the interface can be enhanced by inserting a filler material uniformly dispersed into the adhesive. The filler material must satisfy four main requirements: a) large surface area per unit mass, b) good dispersion, c) alignment and d) interfacial stress transfer. Carbon nanotubes (CNTs)[45] are considered to be an ideal filler material for mechanical reinforcement because of their interesting

mechanical properties and their extremely large interfacial area. Polymer/CNTs composites (e.g.[44,46,47]) have shown many promising results.

In this report a new design is presented to reinforce the bondline of PZT actuators with CNTs. Fabrication techniques were developed for the realization of the proposed design and will be discussed in this report together with interface design and the mechanical study of the CNTs-based interface.

II.2.1 Design and Realization

II.2.1.1 Introduction

CNTs composites have shown promising results in recent years (e.g.[44,48,49]), however uniform dispersion and alignment of CNTs in the hosting matrix is still one of the major problems. CNTs have the tendency to agglomerate, bundle together and entangle, leading to defects in the polymer composites[50,51]. Single CNTs should be isolated, individually coated with the polymer and oriented in a desired direction[44]. The technique that is mostly in use today to produce CNTs composites is to disperse CNTs in a hosting material before aligning them. Usually dispersion is achieved by energetic agitation of CNTs in solvents and in the hosting polymer (e.g.[51,52,53,54,46,55]), and alignment is achieved with the use of electrospinning[56,57,58,59,60] and magnetic fields[61,62,63] melt processing[64], mechanical stretching[65], shear[66], extruding[67] and spin casting[68]. Even though these approaches have shown a lot of improvement, results are still not fully satisfactory. Alternative solutions need to be investigated in order to truly align and disperse CNTs in a hosting polymer.

In this report a unique design of a carbon nanotube-coated PZT (C-PZT) is presented. The fabrication approach is based on pre-aligning and constraining CNTs onto the bondline prior to embedding them into the polymer adhesive. The advantage of this approach is that it can be easily scaled up to larger areas and to a broad range of bonding surfaces, which makes it suitable for structural as well as electronic applications.

II.2.1.2 Problem Statement

In this investigation, it is proposed to develop a new conductive coating made out of oriented carbon nanotubes (CNTs) in order to replace the SP electrode of standard PZTs and improve the

bondline integrity (figure 28). The approach is to develop appropriate fabrication techniques to insert oriented CNTs into the bondline and to conduct mechanical tests to evaluate the interfacial strength of a CNTs-coated PZT actuator (C-PZT) mounted on a hosting structure.

In section II.2.1[72], the focus of the discussion will be on the fabrication techniques. The testing and the test results will be presented separately in section II.2.2[69].

II.2.1.3 Method of Approach

The major tasks in the development of the CNT-reinforced interface include: (1) design of the CNTs film carpet; (2) fabrication of CNT-reinforced interface. The main idea of the interface design is to eliminate the weak link in the bond and reinforce the adhesive layer. With this in mind, one of the two SP electrodes is replaced by a high density nano-electrode array of aligned Carbon Nanotubes (CNTs-NEA), which simultaneously play the role of being an electrode as well as a reinforcing filler material. A scheme of the interface design is shown in Figure 27b. CNTs are uniformly dispersed and oriented into the adhesive polymer with their longitudinal axis perpendicular to the PZT surface.

The main challenge in the fabrication process is to achieve a uniform dispersion and alignment of CNTs in the bond adhesive. Here is presented a new approach to control CNTs orientation, dispersion and distribution in an adhesive bond. The key elements of the approach are: (1) integrate and constrain a Pre-Aligned CNTs (PACNTs) film into the adhesive polymer, as schematically shown in Figure 29, and (2) make use of the strong capillarity effect that characterizes the CNTs carpet. In this way the adhesive polymer is fully absorbed by the CNTs nanochannels, wetting each single CNT and maintaining their orientation; moreover CNTs migration and aggregation during the embedding and curing process is avoided (Figure 29b). With this in mind, the first step is to coat one of the two surfaces which are part of the bond (PZT for this specific application) with a thin film of aligned CNTs, thereby constraining the CNTs tips to the PZT (Figure 29a). The next step is to drop a polymer adhesive onto the film to bond the other surface (metal structure in this case).

There are two possible approaches that could lead to a polarized PZT coated with a CNTs carpet: (1) direct CNTs growth onto a *polycrystalline PZT* surface, or (2) coat a *polarized PZT* with a CNTs carpet. In the first case the PZT polarization can be achieved after the growth process through the CNTs-NEA, while in the second case the PZT polarization can be achieved by

means of a sacrificial silver paste electrode which is then removed and replaced by the CNTs-NEA, at room temperature.

A high- and a low-temperature process were developed for the first and the second method, respectively. The high-temperature process consists of growing aligned CNTs directly onto a polycrystalline PZT surface, while the low-temperature approach consists of transferring a film of oriented CNTs at room temperature from a substrate onto a polarized PZT with the help of an ultra-thin conductive adhesive layer. In this way electrical contact between the PZT and the PACNTs film is maintained. A schematic of the process for the realization of the C-PZT is represented in figure 30.

II.2.1.4 Fabrication Process

Piezoelectric disks with silver paste electrodes were selected as the baseline PZT material. PZTs (material type 850) with a diameter of 6.35mm and thicknesses of 250μm (t-PZT) and 750μm (T-PZT) were used for the low-temperature process. PZTs with 9.5mm diameter and a thickness of 1.24mm were used for the high-temperature study.

Several substrate types were investigated. The substrates in analysis for the two fabrication approaches are shown in Figure 31g and 31b. The standard substrate is a PZT coated with the silver paste electrode. The second type is a bare PZT and the third is a bare PZT coated with an AmSi or SiO_2 layer. The bare PZT is made by peeling off the original silver paste electrode. Peeling for T-PZTs is achieved via mechanical polishing using a diamond foil on a rotating plate, while for t-PZT it is achieved by etching the silver paste in a nitric acid bath. The etching process is chosen to avoid further and uneven PZT thinning. In this case only the SP electrode is brought into contact with the acid in order to minimize chemical variations in the PZT material. The Amorphous Silicon (AmSi) layer was deposited with an e-beam evaporation system, and a Plasma Enhanced Chemical Vapour deposition process was adopted to deposit the SiO_2 layer. For the low-temperature method a 1μm thick AmSi layer was deposited, while for the high-temperature approach variable AmSi and SiO_2 thicknesses were deposited in order to study and optimize the CNTs growth on the PZT surface. Thicknesses ranged from 78Å to 1μm for the SiO_2 layer, and from 500nm to 1μm for the AmSi one. Iron catalyst nanoparticles (24Å) were evaporated onto the as-prepared substrates and oriented multiwalled Carbon Nanotubes (MWNTs) were grown with a Thermal Chemical Vapour Deposition (CVD) process in a 50mm

diameter horizontal quartz tube furnace. Oxygen-free Argon is injected to purge the air and the temperature was increased and stabilized at a pre-set value (700°C) for 10 minutes. Ethylene gas was used as the hydrocarbon source and was diluted with Hydrogen/Argon for higher temperature growths. Argon/Hydrogen was flown again prior to lowering the temperature to cool down the sample. The same procedure was adopted to grow MWNTs forests on silicon chips that had been previously cleaned with Piranha and Hydrochloric Acid. However, in this case the temperature was raised up and stabilized to a pre-set value of 700°C. Ethylene gas decomposed at high temperature, forming a forest of oriented MWNTs on the Fe catalyst nanoparticles. The MWNTs were weakly bonded to the silicon chip.

A conductive adhesive (silver adhesive –CG) layer was spread onto the PZT surface and thinned down to 50nm-1μm (Figure 31h). The silicon chip, coated with the MWNTs forest, was reversed on top of the PZT substrate (or vice-versa) and the two parts were slowly brought into proximity with each other. As soon as contact was made, the Si chip was instantly removed, effecting the transfer of the MWNTs film onto the PZT surface (Figure 32 and 30). The transferred PACNTs were either pre-patterned on the Si chip before printing (Figure 33a) or were patterned to the desired shape after printing (Figure 33b). Patterning, before printing, was achieved by growing CNTs only on preselected areas by selectively depositing Fe nanoparticles. This was done with the help of a shadow mask (Figure 33e and 33f) or with a standard photolithography process (Figure 33c and 33d). Aligned CNTs were then grown on the patterned catalyst area (Figure 33g). Patterning after printing was achieved with a thin Kapton mask coated with a Silicone layer that was brought in contact with the tips of the transferred PACNTs (Figure 33c) and then lifted off (Figure 33d).

After patterning, the CG layer was either cured at room temperature or cured on a hot plate for 10 minutes at 120°C. In this way the CNTs tips were constrained onto the PZT substrate.

The PZT actuator was then bonded to a metal structure (iron cubes with 2mm sides) with a non-conductive structural adhesive (NC) polymer (Hysol EA 9396). Several challenges made the bonding process a difficult step: 1. contact area control, 2. bond thickness control, 3. uniform dispersion and orientation of the CNTs in the hosting adhesive. The approach is represented in Figure 34. The contact area was controlled with a Teflon mask (Figure 34a) which was placed around the PACNTs film. A small amount of adhesive was dropped onto the film (Figure 34b). The metal was mounted on a micro-manipulator, placed on top of the PACNTs carpet and slowly

brought into contact with the C-PZT (figure 34c). The bond thickness was controlled by controlling the vertical displacement of the micro-manipulator and by monitoring its gap from the PZT substrate. This method could be adapted to large metal areas by mounting the PZT, rather than the metal, onto the micro-manipulator and by dropping the adhesive polymer onto the metal instead of the C-PZT.

II.2.1.5 Results and Discussion

Here are discussed the low- and high-temperature processes that were developed to insert a high density array of oriented CNTs in a structural bond. The low-temperature approach consists of printing a CNTs film from one substrate to any other substrate with a low-cost, simple and reliable technique. It has the potential to be used for small and large area applications. The high-temperature process consists of growing a thin film of aligned CNTs directly on one of the two surfaces which are part of the bond.

The next sections provide a step-by-step analysis and discussion of the developed processes, which include: (5.1) PZT substrate preparation results, (5.2) realization of the polycrystalline C-PZT with the high temperature process, (5.3) realization of the polarized C-PZT with the low-temperature process, (5.4) integration into adhesive polymer: dispersion and alignment.

II.2.1.5.1 PZT substrate preparation results

Here are discussed the results of the chemical treatment and mechanical polishing approach that are adopted to peel the silver paste (SP) electrode that coats standard t- and T-PZTs respectively. Particular focus was given to the effect of the adopted process on the chemical content and microstructure of the PZT (Lead-Zirconate-Titanate) material. The chemical treatment was optimized by running experiments in: (a) Nitric acid and; (b) Nitric acid followed by Hydrofluoric acid (HF) baths for a variable time (up to 2 hours). The main result of this study is that only Nitric acid can be used to peel the SP electrode. In this case no meaningful variation of the PZT microstructure and of the PZT elemental content was observed. The PZT surface was affected by the HF solution and this effect was stronger for longer etching times. Figure 35 shows the X-Ray Intensity vs. Energy for an untreated PZT, and for a PZT treated in HF for two hours (Figure 35a). The analysis shows a change in the PZT elemental content. In particular, a 194% and 176% relative decrease in *Ti* and *Zr* content, respectively, and the appearance of the *F*

peak are observed in the case of treated PZT. These results were confirmed by the analysis of the PZTs microstructure before and after treatment. A typical PZT morphology was characterized by a regular assembly of microscopic crystal grains (Figure 35b) which can still be recognized in PZT samples treated in Nitric acid. A drastic change was observed when PZTs were treated in an HF solution. In this case the typical PZT crystal structure turned into an amorphous morphology (Figure 35c). This effect was again observed to increase with increasing time in the HF solution.

The mechanical polishing approach was found to maintain the same PZT elemental composition, however, it caused a reduction in PZT thickness due to a smoothing and levelling effect of the crystal grains.

II.2.1.5.2 Growth of aligned CNTs on a PZT substrate

The CNTs growth process on a polycrystalline PZT surface showed that a carrier layer such as SiO_2 or AmSi was needed to enhance the growth and that the process was strongly dependent on its thickness and temperature. Figure 36a is a picture of a PZT before and after the optimized CNTs growth process. The result is a PZT coated with a high density array of oriented CNTs (C-PZT) directly grown on its surface. The picture shows a macroscopic view of the CNTs carpet which looks like an ultra-thin uniform black coating (figure 36a), while the Scanning Electron Microscope (SEM) characterization at the nano-scale showed nanotubes with diameters of about 50-90nm and with a global orientation normal to the PZT surface. The CNTs longitudinal axis was characterized by an irregular waviness along its entire length, giving rise to a total film thickness of 2μm-3μm. The result in Figures 36a and 36b shows the optimized process which was achieved on a peeled PZT coated with a 1μm thick AmSi layer. Ethylene was diluted with Hydrogen/Argon carrier gases at a growth temperature of 820°C. The grain boundaries of the ceramic surface give rise to irregularities of the CNTs carpet which can be observed in Figure 36b.

The growth dependence on the process temperature was shown in Figure 37 and 38a. The inset on the left corner in Figure 38a shows a scheme of the experimental procedure. PZTs were coated with a 1μm thick SiO_2 layer and growths were done flowing pure Ethylene at increasing temperatures (from 700°C to 800°C). The SEM characterization (Figures 37a-37f) clearly shows that the CNTs-density increases with increasing temperature from 700°C to 760°C (Figures 37a-

37d) and at 780°C (Figure 37e) fibers with diameters of about 250nm are formed. When a temperature of 800°C is reached, CNTs or fiber growth is totally lost (Figure 37f). To quantify this study, the percentage area covered by the CNTs was calculated from the SEM pictures. Results are shown in Figure 38a with the dots and with the fitting curve of the experimental data. The curve plotted the percentage area (A%) vs. temperature. It indicates that when there is no carrier layer, CNTs growth is totally inhibited. The addition of a carrier layer (SiO_2 for this case) allows CNTs growth and this effect increases with increasing temperature (up to 780°C) for a given SiO_2 thickness. CNTs growth is also affected by the thickness of the substrate carrier layer; an increasing thickness results in a density increase. The scheme on the bottom right of Figure 38a shows the experimental procedure. The growth temperature was fixed at 760°C, while the substrate thickness (SiO_2) was increased from 7.8nm to 1μm. Both SEM images (Figure 38b-38e) and the experimental curve (square marks in Figure 38a) show that the CNTs A% increases with increasing substrate thickness. The analysis of the elemental composition shows that carbon is the main element identified along with small traces of oxygen that can be attributed to oxidation of carbon nanotubes after the growth process.

The high temperature reached during the growth process may cause depolarization of the PZT crystals which eventually need to be polarized again after growth.

II.2.1.5.3 Printing of aligned CNTs on a PZT substrate

Best results for the realization of the MPZT was achieved with the printing method approach at room temperature. One of the advantages of this method is that PZT depolarization is avoided due to the low temperature of the process, so PACNTs can be transferred directly onto a polarized PZT. With this method, oriented CNTs were first grown on a Si chip and then were transferred on the PZT surface with the help of an ultra-thin CG layer. The process results were shown in Figure 39. A film of oriented CNTs was grown on a Si chip (Figure 39a). The CNTs axes were oriented in the vertical direction, perpendicular to the Si substrate and were uniformly distributed over the entire surface. CNTs showed a homogeneous height of 60μm and their longitudinal axes had a wavy-like shape. Iron catalyst nanoparticles were mainly located at the tips in contact with the Si substrate showing a predominant bottom-up growth process. The free tips of the CNTs film were then brought in contact with the PZT surface (coated with the CG layer). CNTs got transferred owing to the weak CNTs-Si bond and to the higher sticking force

generated by the CG. Figure 39b shows an SEM image of a polished PZT coated with a transferred CNTs film. A higher magnification of the printed film is in Figure 39c. After the transfer, CNTs kept their vertical alignment and coated uniformly the entire PZT surface. Iron nanoparticles were then localized in the free CNTs tips and can be recognized in the image as the whiter dots. A scheme of the nanoparticles location is shown in Figure 30. A top view SEM image of the edge of the CNTs film is shown in Figure 39d. Moving from the bottom to the top of the image the three overlapped layers are shown: 1) PZT grains, 2) conductive adhesive (CG) and, 3) CNTs free tips.

The result of the printing study shows that key elements for a successful transfer are the pressure applied during contact and the contact time.

The pressure applied during printing could compromise the result. CNTs are known to have, in compression, a very high deformability (up to 100%)[70]. However, plastic deformations can occur for CNTs films and these deformations may be localized at the CNTs tips for a low $Lc/\sqrt{A}$ ratio (*Lc* being the height of the CNTs and A a square extensional area of the film)[70]. Figure 39a shows an example of a CNTs film, plastically deformed due to the pressure applied during printing. The local deformation is usually uniformly spread all over the entire film area (Figure 39a). The SEM image in the inset (left up) shows a higher magnification of a *kink*-like plastic deformation localized at the tips of the CNTs film, as schematically represented in the inset in Figure 40a.

The contact time may influence the transfer result because the PACNTs film behaves as a high density array of nanochannels (Figure 40b), being the average axial distance between each single CNT in the film of the order of less than 50nm. The capillarity effect in a channel increases with the decreasing radius and so it is enhanced for the specific CNTs film in analysis. As a consequence, when CNTs are brought into contact with a viscous fluid (like the CG non-cured layer), they may absorb the fluid along the nano-channels (along the film thickness). A reduced contact time and a reduced thickness of the CG layer may reduce such an effect and enhance the transfer results. A longer contact time (order of 1sec.) could fully compromise the transfer. In this case, PACNTs would not be printed on the PZT, they would stay on the Si chip partially embedded in CG. In Figure 40b is an example of a PACNTs film, transferred onto the PZT surface and with a partial absorption of CG along the film thickness.

CNTs films were successfully transferred with conductive and nonconductive adhesive polymers, which leads to the adaptability of the proposed approach to different kinds of applications, adhesive types and bonding surfaces.

II.2.1.5.4 CNTs Alignment and Dispersion

The goal and the challenge were to reinforce the adhesive polymer with uniformly dispersed and "oriented" CNTs. With the proposed approach the NC adhesive was dropped onto the freestanding PACNTs carpet which was bonded, at its base, to the PZT surface (C-PZT), as shown in figure 34b. A thorough microscopic analysis of the samples was conducted to: a) verify and understand how the developed procedure influences the PACNTs dispersion in the adhesive, b) determine whether the PACNTs orientation was affected by the embedding process, c) determine whether the PACNTs were fully embedded into the polymer adhesive, and d) verify if migration of CNTs happened during the curing process. Figure 41 provides side views of a PACNTs carpet transferred onto a PZT surface (Figure 41a) and then embedded into the adhesive polymer (Figure 41b). These images showed that CNTs kept their original wavelike configuration, alignment, orientation and location after being embedded into the polymer. The top view image of the same sample also shows (Figure 41d) that each single CNT in the adhesive was isolated and surrounded by the polymer. This interesting result is due to the fact that: (a) the polymer was fully absorbed by the nanochannels along the entire channel length avoiding a direct loading of the CNTs due to the polymer weight, (b) the adhesive entirely filled up the nano-spaces along the CNT heights which avoided the formation of voids in the nanocomposite bond, (e) the bond between the CNTs tips and the PZT surface avoided the CNTs migration during the curing process. The final result was an adhesive reinforced with a high-density array of oriented CNTs which were fully dispersed and embedded in the hosting material. In conclusion the approach of pre-aligning and constraining CNTs prior to embedding produced an optimum result in terms of CNTs dispersion, uniformity and orientation.

II.2.2 Characterization and Testing

The silver paste electrodes are known to bc a weak link between the PZTs and the hosting structure since they can be easily peeled-off from the PZT surfaces. In section II.1 it was shown that a debond between the silver paste coat and the PZT ceramic could not only considerably affect the PZT actuating performance, but also reduce significantly the load-transfer capability of the PZT ceramic actuator to the hosting structure through the adhesive interface[71]. To reduce the risk of bondline failure or degradation at the PZT-silver paste interface, Lanzara and Chang[72,73,74,75] proposed to replace the silver paste elecctrodes with a nanoelectrode array of carbon nanotubes as described in section II.2. The design of the CNTs coated PZT (C-PZT) consists of a carpet of pre-aligned carbon nanotubes (PACNTs), transferred onto the PZT surface and oriented perpendicularly to the bondline. The PACNTs carpet is used at the same time as an electrode and to reinforce the interfacial adhesive layer of the PZT sensors/actuators. Very little study has been devoted in the literature to the use of PACNTs as an electrode as well as a reinforcing element for PZT actuators. Randomly mixed CNTs with an epoxy resin showed a 45% increase in adhesion strength compared to a graphite fiber composite interface[76]. This result showed that dispersion and alignment of CNTs in the polymer are key parameters that affect the bond shear strength significantly.

In this section, the mechanical behavior, particularly the shear strength, of the C-PZT actuator was characterized. The results for a high density array of PACNTs and randomly mixed CNTs are shown and compared with the case of an adhesive layer without CNTs. The dependence of the shear strength and the failure mechanisms on the interface microstructure is investigated.

II.2.2.1 Problem Statement

The mechanical response of a carbon nanotube-coated PZT (C-PZT) interface[Error! Bookmark not defined.] is investigated. The CNTs are used as conductive electrodes to replace the silver pastes on the PZT surfaces and as reinforcing elements for the interface. Figure 42 shows the schematic of a C-PZT where a PZT ceramic disc is bonded to a substrate with an adhesive reinforced with a pre-aligned (PACNTs) carpet. It is to be noted that the silver paste electrode was removed from the PZT surface before the PACNTs carpet was mounted. The objective of the study is to evaluate the strength of the bondline between the PACNTs and the PZT. The response of the C-PZT interface was compared with the standard one and with the one of adhesive mixed with

randomly distributed CNTs. Major focus of the mechanical tests is given to the interfacial shear strength and to the bond failure mechanisms.

II.2.2.2 Sample Design

An important aspect of this study is the design of the samples to be used to investigate the mechanical response of the bondline of a C-PZT surface mounted on a metal structure and to compare it with other bondline compositions. The major difficulty in this investigation was to test the shear strength of the C-PZT bondline avoiding PZTs failure due to their brittle nature. With this in mind, samples were designed in a way to avoid direct loading of the PZT ceramics and guide failure only into the C-PZT/metal structure interface. Figure 43 shows a scheme of the proposed sample design where a PZT disc is fully bonded to a Brass cube (10mm side) on one side and partially bonded to an Iron cube (2mm side) on the other side with Hysol EA9396 epoxy adhesive, which is a standard adhesive used in aerospace applications. The Fe cube is representative of the metal structure. The adhesive between the PZT and the Fe cube is reinforced with CNTs. With this design shear loads were applied directly to the Fe cube avoiding, as desired, direct loading of the PZT ceramic. Moreover the smaller contact area between the PZT and the Fe cube guarantees that failure occurs in that interface only.

The aim is to compare the following bondlines: 1. C-PZT fabricated with the low and the high temperature processes presented in ref.72 and bonded to the structure with the adhesive polymer; 2. standard PZT surface coated with silver paste electrodes and bonded to the structure with the adhesive polymer; 3. bondline reinforced with randomly distributed CNTs into the adhesive polymer. For this reason samples with three different PZT substrates and adhesive compositions were studied as schematically shown in Figure 44. The PZT substrates were: 1. Standard PZT; 2. Bare PZT (required for the low temperature process[72]) and 3. PZT coated with an Amorphous Silicon (AmSi) layer (required for the high temperature process[72]). The adhesive compositions were: 1. baseline adhesive (Type I); 2. adhesive reinforced with randomly mixed CNTs (Type II and III) and 3. adhesive reinforced with PACNTs (C-PZT) (Type IV). Sample types II and III differ in the volume of CNTs, which is equal to or twice that of the oriented CNTs case (Type IV). All the 12 possible combinations of substrate type and adhesive compositions were studied for a total number of 43 samples. It is to be noted that C-PZTs fabricated with the high

temperature process presented in ref. 72 were indirectly tested by testing the mechanical response of C-PZTs coated with an AmSi layer and with transferred PACNTs[72].

II.2.2.3 Sample Preparation

Piezoelectric (PZT) discs, material type 850, that are coated with silver paste electrodes were selected as the baseline PZT material. The PZTs have a diameter of 6.35mm and thicknesses of 250μm (t-PZT) and 750μm (T-PZT).

Samples were prepared by first bonding the Fe cube to the PZT and then bonding the PZT to the Brass cube. The bonding area between the PZT and the Fe cube was controlled by means of a Teflon mask which was placed onto the PZT and around the PACNTs prior to bonding the Fe cube[72]. The images of the samples during fabrication are shown in Figures 45a, 45b and 45c. The interface reinforced with PACNTs and the substrates were fabricated by the method described in ref. 72. The interface reinforced with randomly mixed CNTs was fabricated by dropping a predefined volume of adhesive polymer onto a CNTs carpet and by stirring the mixture with high energy. The mixture was then dropped onto the Teflon mask which was mounted on the PZT surface prior to bonding the PZT to the Fe cube with the method described in ref.72. In Figure 44e is a picture of the samples prior to testing.

II.2.2.4 Testing Fixtures

The primary goal of this work is to characterize the shear strength of the C-PZT actuator bondline and compare it with the one without CNTs and with randomly mixed CNTs. The major challenge is to measure the shear strength at a local scale for the very small interfacial areas involved. For this purpose, special test setups were chosen and adapted to this study by designing appropriate fixtures. The main idea is to perform tests by loading the interface, in shear, up to failure. A Micro Hardness Tester (MHT) and a Delaminator were chosen for this purpose. These instruments can apply low compressive and tensile loads and are mainly used for local analysis in very small areas. Figure 46 shows the MHT test setup. Typically a MHT consists of an indenter tip that can move in a vertical direction and apply a predefined load in compression. For this study, a 2mm diameter Tungsten Carbide (WC) flat indenter was designed in order to apply a uniformly distributed load to the Iron cube. A mechanical grip was used to hold the Brass cube tightly at its base and to keep the interface in a vertical plane (Figure 46a). The grip was

part of a movable stage which allowed the control of the sample location along the horizontal plane.

The Delaminator set-up is shown in Figure 47. The set-up consists of an actuator and a load cell placed along the same horizontal axis. The actuator can move to provide tension on the Iron cube sample while the load-cell, which is fixed at the other end and houses the sample, measures the load. Two special grips were designed and fabricated. The first grip was used to house the Brass cube sample (see Figure 47) with the help of a 3mm ϕ screw and hold the interface in a horizontal plane during the test, parallel to the loading direction. The second grip was used to apply a shear load to the Iron cube by bringing the inside edge of the grip in direct contact with the Iron cube during testing (as shown in Figure 47). These special grips are connected to the load cell and the actuator respectively with the help of 4mm pins which allow rotation of the grips around the pins axis during testing (see Figure 47).

II.2.2.5 Test Procedures

To characterize the bond shear strength of the PZT actuator interface, a shear load with increasing intensity and up to failure was applied to the Iron cube while the sample was held in the mechanical grip of the MHT and in the load cell of the Delaminator. The failure loads were recorded and the shear strength of each of the tested samples was calculated by dividing the failure loads with the corresponding contact area. Contact areas were determined by means of scanning electron microscopy (SEM) imaging and characterization. In the case of the MHT setup, the Fe cube was placed under the flat indenter prior to testing. The indenter was brought into contact with the Fe cube with a contact force of 25mN and an approach speed of 40% per min. Upon contact, a compressive linear load (shear for the interface) with increasing intensity was applied to the Fe cube (loading rate of 15000mN/min) to bring the sample up to failure. In the Delaminator setup the interface in analysis was kept in the horizontal plane parallel to the loading axis (actuator's axis). The inside edge of the grip which was mounted onto the actuator (see Figure 47), was brought into contact with the Fe cube. In this way tensile loads (shear for the interface) were applied directly to the Fe cube until reaching failure. Tests were performed at an actuator speed of 0.27μm/sec.

II.2.2.6 Results and Discussion

Here it is shown that the bondline strength of a C-PZT surface mounted on a substrate is significantly improved in comparison with a PZT coated with standard silver paste electrodes. It is also shown that failure did not occur between the PZT and the PACNTs coating. In this study emphasis is given to the bond shear strength, to the failure mechanisms and to the influence on the failure mechanisms of the fibres length relative to the bond thickness (Lc/H). The analysis is also extended to different kinds of CNTs-reinforced interfaces, in order to understand how the adhesive composition, fibres orientation and dispersion influence the mechanical response.

II.2.2.6.1 Shear Strength

The results of the normalized shear strength for each adhesive type (Type I to Type IV) are reported in Figure 48. The normalization is done with respect to the average shear strength of the baseline adhesive (Type I). The results clearly show that when CNTs are randomly mixed with the adhesive, the overall improvement of the shear strength is not significant compared to the baseline adhesive case (comparison of Type II and III with Type I). On the other hand, when oriented PACNTs are used to reinforce the bond, a significant improvement of the shear strength is observed with a peak value of 274% (Type IV). In this case however, the experimental data shows a wide variation suggesting that the CNTs orientation and distribution inside the bond might be playing a major role, as discussed later (see Section II.2.2.6.2).

II.2.2.6.2 The Influence of CNTs Orientation and Distribution

The SEM analysis of the samples after failure shows that samples with different composition have different morphology at the nano- and microscale and this influences their mechanical response (see Figure 49). When CNTs are randomly mixed with the adhesive polymer (20% CNTs volume fraction) (Figure 49a), they tend to migrate inside the polymer and entangle during the mixing and curing process. The entangling effect is enhanced by the CNTs' strong electrostatic attraction and by the polymer flow at low viscosity during the high temperature curing process. This results in the formation of micro-agglomerates and of microdefects spreading all over the bond thickness (see arrows in Figure 49a). The entangling effect increases with increasing CNTs volume fraction (Figure 49b). A 30% CNTs volume fraction gives rise to an ultra-viscous adhesive polymer layer prior to curing and to an increase in agglomerates density over the bond thickness after curing. The adhesive polymer surface becomes rough

because of microagglomerates sticking out in an irregular manner. This results in a further weakening of the interface as shown by the experimental data in Figure 48 (Type III).

The adhesive morphology changes completely when a PACNTs film is inserted in the adhesive polymer (Figure 49c, 49d). In this case, CNTs are constrained at the base, which helps to avoid migration during the embedding and curing process. Moreover, the strong capillary effect of the nanochannals in the PACNTs carpet enables uniform flow of the polymer in the nanochannels along their entire length of the CNTs and at the same time, keeping each single CNT isolated and fully coated with the polymer. CNTs keep their original wavelike configuration at the nanoscale (Figure 49c) during the embedding and curing process (Figure 49d). The result is that CNTs are uniformly aligned and dispersed in the adhesive polymer layer as previously discussed[72].

II.2.2.6.3 Shear Strength Dependence on the PACNTs Microstructure

Here it is shown that the length of the PACNTs relative to the bond thickness plays a major role in effectively reinforcing the bondline. To investigate the causes of the large variation of shear strength values in the case of PACNTs, (shown in Figure 48a), the PACNTs bond microstructures after failure were studied. Particular emphasis was given to the bond thickness (H) and the PACNTs length (Lc).

Three main microstructure types were identified and are schematically shown in Figure 50: a) PACNTs that are shorter than the bond thickness ($Lc/H<1$); b) PACNTs that are longer than the bond thickness (in the range of $1<Lc/H<3$); or c) PACNTs that are much longer than the bond thickness ($Lc/H>3$). When the PACNTs are shorter than the bond thickness, an adhesive layer reinforced with CNTs and of thickness Lc, is in direct contact with the PZT, while a very thin bare adhesive layer of thickness Δ is in direct contact with the metal surface (where $\Delta=H-Lc$). When the PACNTs are longer than the bond thickness ($Lc/H>1$), the global and local deformation of the PACNTs film is influenced by the bonding process. The PACNTs tips in contact with the metal may locally fold, increasing the CNTs density in that region. As a consequence, the CNTs density along the bond thickness is non-uniform. In Figure 51, the effect of the local deformation is shown for $Lc/H=1.1$. The PACNTs film after transfer and prior to embedding and bonding is shown in Figure 51a. In this case CNTs are vertically aligned. Once the adhesive is dropped onto the PACNTs and the C-PZT is bonded to the metal structure, the

CNTs bend and their tips fold locally in the areas of contact with the metal substrate. The typical example of a deformation is represented by the solid black line. Figure 51c shows a closer view of the folding effect at the metal interface. The dependence of this folding effect on the Lc/H ratio is studied. The CNTs density and the folding effect at the metal interface increases with increasing Lc/H ratio ($Lc/H>>1$) as shown in Figure 50. The density increase is found to lead, in extreme cases, to the loss of bond formation between the PZT and the metal structure. Two representative cases are shown in Figure 52, left and right panels, for $Lc/H = 1.2$ and 3.6, respectively. The folding effect is observed in both cases (see arrows in the upper panels), and appear to be stronger for the sample with larger Lc/H ratio (right panels). For the 1.2 ratio value, the PACNTs are fully embedded and isolated from each other in the adhesive polymer layer while for the 3.6 ratio value, because of the larger folding effect, the resulting CNTs density at the adhesive-metal interface is larger leading to partially exposed CNTs in that interface (top view picture in Figure 52 – on the right panel). This microscopic analysis suggests that the variation of the Lc/H ratio leads to a non-uniform distribution of the CNTs along the bond thickness H. It is likely that this is the key aspect to explain the mechanical response of the PZT-metal bond.

II.2.2.6.4 Failure Modes and their Correlation with the Interface Microstructure

Here it is shown that bondline failure in the C-PZT samples, does not occur in the interface between the PZT ceramic and the PACNTs coating. However it is shown that the bondline failure mechanisms and the shear strength are directly correlated to the Lc/H ratio. The dependence of the shear strength on the Lc/H ratio in the case of PACNTs is shown in Figure 53. From the microscopic analysis of the failure mechanisms, a clear correlation is identified between the mechanical response and the adhesive layer microstructure discussed above.

More specifically, four different regions were identified corresponding to four different failure modes. These failure modes are found to be directly related to the Lc/H ratio, which gives rise to a different distribution of CNTs along the bond thickness, and hence to a different mechanical response. The direct relation between the mechanical response, the failure mechanisms and the geometry is schematically represented in Figure 53 (ZONE I to IV). It is observed that when $Lc/H<1$, the failure occurs in the Δ layer (ZONE I of Figure 53). When the ratio is $1<Lc/H<3$, there are two failure mechanisms (ZONE II and III): (a) cohesive failure involving the entire

bond (ZONE II) or; (b) failure of the support layers (ZONE III). Finally, all samples with *Lc/H>3* are characterized by an adhesive failure mechanism (ZONE IV).

When PACNTs are shorter than the bond thickness, the bond is characterized by the layered microstructure described in section II.2.2.6.3 and schematically shown in Figure 53 (ZONE I). In this case, cohesive failure is restricted to the top layer of thickness Δ (weaker bondline) above the CNTs leaving intact the PACNTs layer below. An example of this failure mechanism is shown in Figure 54. The highlighted zone represents the contact area between the PZT (Figure 54a) and the metal (Figure 54b) prior to failure. Adhesive polymer spots, as thick as the Δ layer, are found on the metal surface and are highlighted in the picture, while the bulk of the reinforced adhesive layer (thickness of *Lc*) is left onto the PZT surface. A higher magnification of a hole on the PZT surface (Figure 54b) shows the CNTs tips inside the adhesive polymer which suggests that failure occurs in the Δ layer only.

Optimal results are observed when PACNTs are longer than the bond thickness with Lc/H values between 1 and 3 (ZONE II). In this case, the bond is made up of a reinforced adhesive along its entire thickness (Figure 53b) and the CNTs density in contact with the metal surface increases with the PACNTs length *Lc*. The highest shear strength improvement is observed when the PACNTs length is twice as long as the bond thickness and bare T-MPZT are bonded to the metal cube. In this case multiple fractures along the entire bond thickness *H* and length are observed giving rise to cohesive failure of the interface. Figures 55a and 55b are SEM images showing the contact area between the PZT (Figure 55a) and the metal surface (Figure 55b) as highlighted. The multiple fractures are shown with the curves that are drawn for better visualization. Fractures in the PZT and metal particularly match to each other. The fractured surfaces are mainly in multiple layers and orientations and have CNTs extending out of them (Figure 55c). CNTs may slow down fracture propagation, keeping the edges of a propagating fracture (figure 56b) joined until their breaking and/or pull-out from the adhesive polymer occurs (Figure 55c). On the contrary, when a fracture occurs in a baseline adhesive it rapidly propagates undisturbed in the bond until complete failure is reached (Figure 56a). This behaviour can also be observed in the Displacement vs. Time curves (Figure 56) of a bare and a PACNTs-reinforced adhesive which shows a failure delay if PACNTs are part of the bond.

For the *Lc/H* ratio in the range 1 to 3, in the case of t-PZTs or T-PZTs coated with an AmSi layer (as needed for the high-temperature fabrication process[72]), very low shear strength values

are recorded which is due to the fact that the failure mechanism is characterized by peeling off of the AmSi substrate without involving either the bond or the interfaces. Similarly, when the C-PZT is made out of a t-PZT, the bond failure occurs for PZT peeling as shown in the scheme in Figure 57. This is because of the fact that the PZT surface, which is made up of an aggregation of crystal grains, may peel-off with the bond. The consequence of this failure mechanism as observed is that, after failure, the entire reinforced bond is attached to the metal (Figure 57b and 57d) and its upper surface is coated with a layer of PZT crystals (Figure 57c and 57e). It is unclear why PZT grains peeling was observed in t-PZTs only and not in T-PZTs, but it is suspected to be associated with the chemical treatment performed on t-PZTs[72].

When CNTs are much longer than the bond (ZONE IV) excessive folding of CNTs may weaken the interface in contact with the metal due to a much higher CNTs density in that interface. The density effect can be seen in Figure 58c where the contact interface with the metal is shown. The shear strength is very low for all the analyzed substrates of this type.

The normalized shear strength (*S/So*) was plotted vs. *Lc/H* ratio by fitting the experimental data that showed an actual bond failure (zone I, II and IV). The resulting Gaussian fitting curve is representative of the mechanical response of the C-PZT-metal bond as a function of the bond nano/microstructure (*Lc/H*). These preliminary results show that the *Lc/H* ratio is a key factor for truly reinforcing the bond shear strength with a high density array of oriented CNTs and could potentially be used to predict and design structural bonds with enhanced interfacial strength. A complete understanding of the observed phenomena is under investigation and more studies are being performed to control the bond thickness in relation to the CNTs length during manufacturing. The study of the long term durability and signal analysis of the designed C-PZT sensor/actuator is in progress.

III. CONCLUSIONS

The SEM-based code has been developed. The code is able to solve a coupled electro-mechanical field for piezoelectric materials. Furthermore, as a solution strategy, the code employs explicit time integration scheme for elasto-dynamic solver and Gauss elimination for static electric fields. This study allows us to make the following conclusions:

1) The SEM has excellent advantages over the FEM in numerical analysis of the ultrasonic Lamb wave propagation.

2) The numerical simulation of the wave propagation by the SEM-based code on the aluminum plate is verified by the experimental results.

3) The SEM-based code can simulate the scatter waves induced by a crack.

4) The SEM-based code has shown its feasibility to SHM applications as a simulation tool to optimize the key parameters of damage detection such as sensor shape, size, locations, diagnostic waveform, etc.

The results of an experimental and numerical study of the effects of interface debonding on the performance of PZT actuators were presented. The bonding conditions were found to be a key parameter in the reliability of PZT actuators. A bond degradation can lead to energy losses which could compromise the response of the structural health monitoring (SHM) systems if not taken into account properly. In this study local asymmetric and symmetric interface debonding were considered and compared with the case PZT actuators fully bonded to an aluminium plate. Tests were performed over a wide frequency range (100KHz and 500KHz) and a simplified two-dimensional Spectral Element Method-based code was used to validate the study. Major findings of the experimental and numerical results were:

- Partially debonded interfaces are subjected to an overall decrease in the signal amplitude and a signal phase delay for increasing debonding areas.

- A 30% asymmetric debonding suffered most significant energy loss around the natural resonance frequencies of the PZT actuators.

- Variations in debonding shape and location underneath the PZT actuators lead to signal strength variations (the most significant signal amplitude drop was found for a peripheral interface debonding).

- A partial asymmetric interface debonding lead to stress concentration between the PZT layer and the metal structure.

These findings give a systematic template that can be used in the SHM algorithms to compensate for and address energy losses due to the PZT interface degradation during the in-service life of a structure.

A new design to reinforce the bondline of PZT actuators to a metal substrate was also presented. The key of this design is to replace the silver paste electrode of a standard PZT disc with a high-density array of oriented carbon nanotubes (CNTs carpet) that acts as electrodes as well as reinforcing elements at the interface. The report focuses on the method used to insert the CNTs carpet into the bondline. The approach consists of inserting a carpet of Pre-aligned CNTs (PACNTs) into the adhesive and making use of the capillarity properties of the CNTs carpet to fully absorb the adhesive polymer. This is done by coating one of the two bonding surfaces (PZT for this specific application) with the PACNTs carpet and constraining the carpet to the surface. A low- and a high-temperature process was investigated in order to coat the PZT surface with the PACNTs carpet (C-PZT). The microscopic analysis of the as-produced samples shows that with this approach CNTs can be fully dispersed and oriented into the adhesive polymer. The low-temperature method has the advantage that it can be used for materials with low-temperature capabilities, and can be generalized and scaled-up to larger areas for structural as well as electronic applications.

It was also shown that the bondline strength of a C-PZT surface mounted on a substrate is significantly improved. The experimental study shows that the interfacial shear strength can be significantly improved with the proposed bondline design and that failure did not occur between the PACNTs coating and the surface of the PZT ceramic. It is also shown that the shear strength and failure modes are very sensitive to the nature of the bonded surfaces, to the interface microstructure and to the ratio of CNTs length (Lc) to the bond thickness (H). Variations in the Lc/H ratio causes a variation to the interface microstructure which influences the shear strength and failure modes.

V. LIST OF FIGURES

Table 1 Sensor locations

	Coordinate (mm)	
	X_1	X_2
PZT 1	177.8	330.2
PZT 2	177.8	177.8

PZT 3	304.8	355.6
PZT 4	355.6	177.8

Table 2 Comparison of solution accuracy

SEM		FEM		
resolution		resolution	full integration	reduced integration
19	116.44(0.00%)	95	116.30(0.12%)	116.65(0.18%)
15	116.45(0.01%)	76	116.22(0.19%)	116.76(0.27%)
11	116.46(0.03%)	48	115.88(0.48%)	117.28(0.72%)
9	116.40(0.04%)	38	115.55(0.76%)	117.78(1.15%)

Table 3 Comparison of computational resources

	SEM	FEM
		reduced integration
Total Numbers of active D.O.F.	6768	224648
Computational Time	250 sec	4280 sec

(a)   (b)

Figure 1. Comparison between finite element and spectral element (a) linear finite element (b) 6-th order spectral element

(a)   (b)

(c)
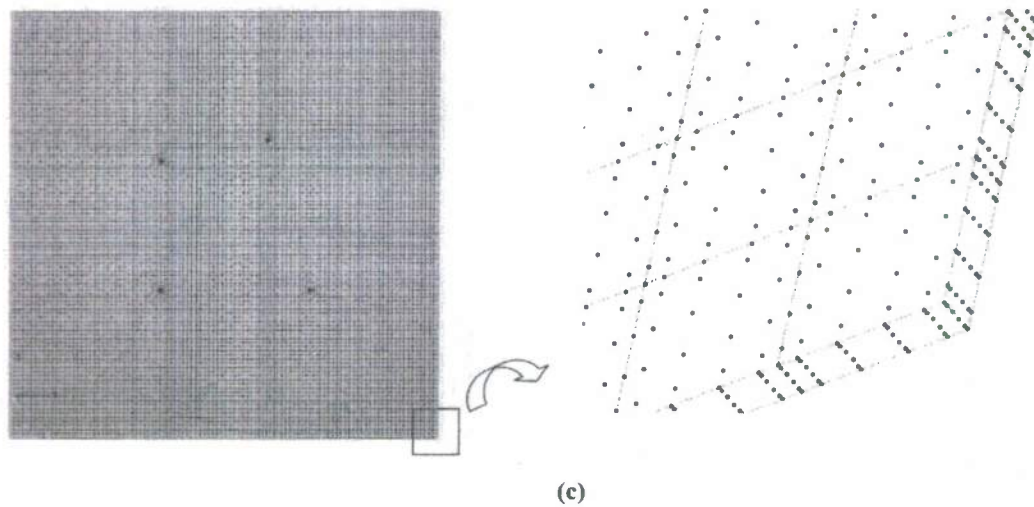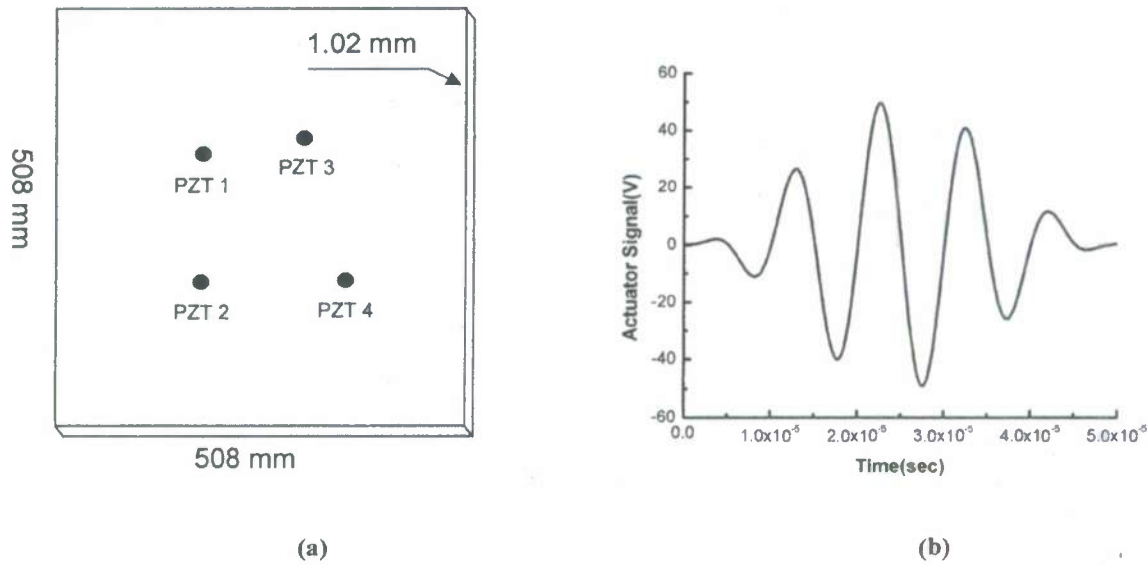
Figure 2. Square aluminum plate with 4 piezoelectric transducers on one side (a) geometric configuration, (b) excitation signal (100kHz) at PZT 2 , (c) mesh configuration-elements & nodes
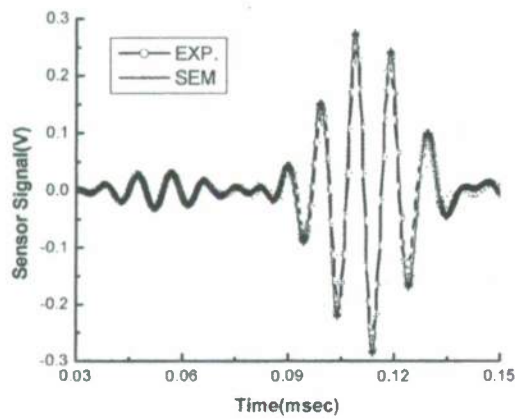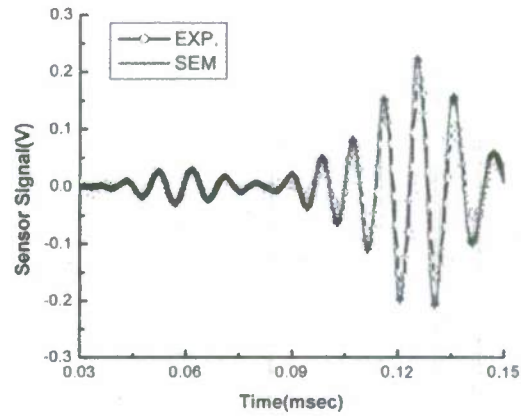
(a)   (b)

Figure 3. Sensor signals at (a) PZT 1, (b) PZT 4
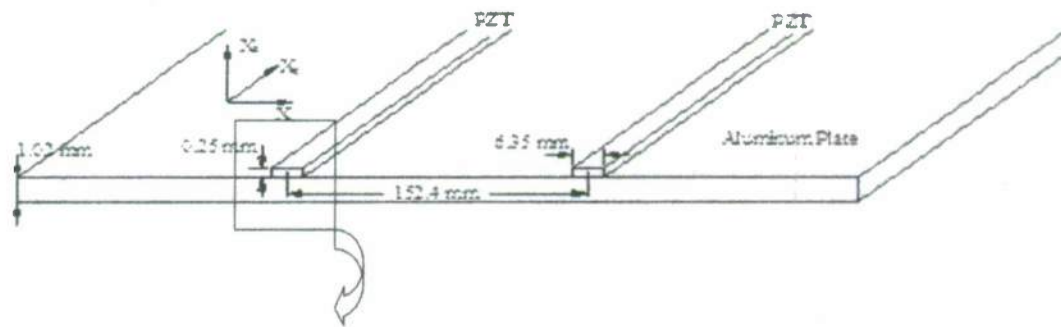
(a)
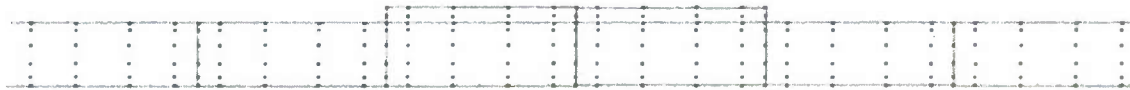
(b)

(c)

Figure 4. Configuration of geometry and mesh to study the code performance: (a) geometric configuration, (b) mesh configuration for finite element analysis, (c) mesh configuration for spectral element analysis

(a)   (b)
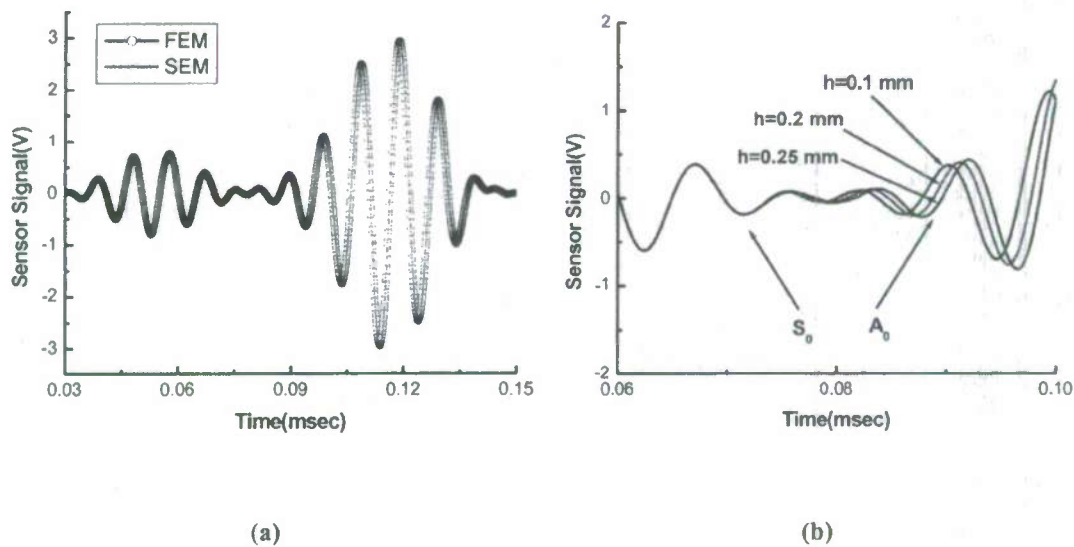
Figure 5. Sensor signals (a) comparison between FEM and SEM, (b) error of wave velocity in FEM
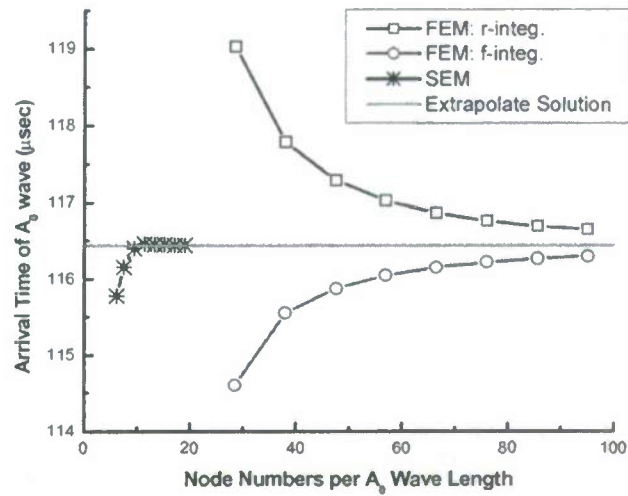
Figure 6. Solution convergence
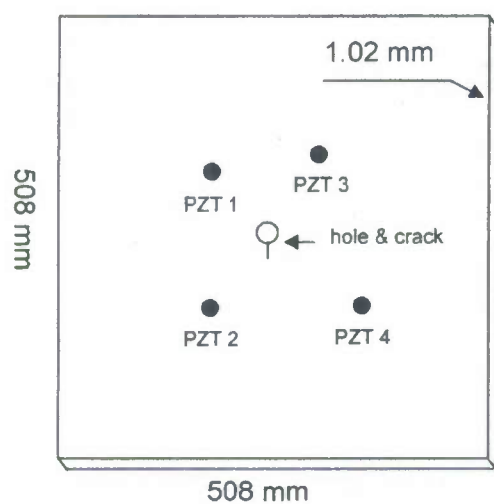
(a)
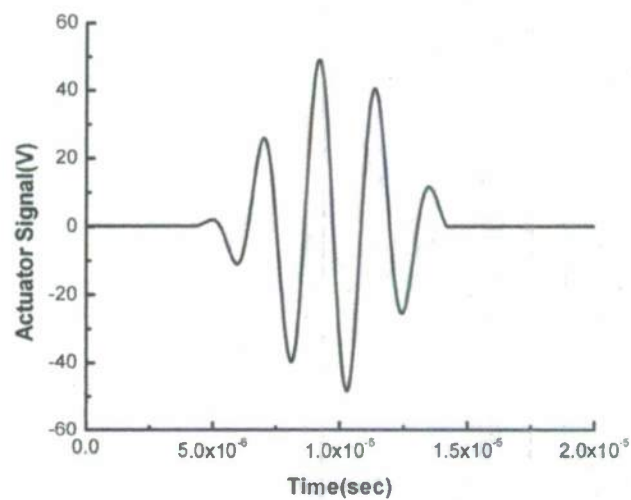
(b)
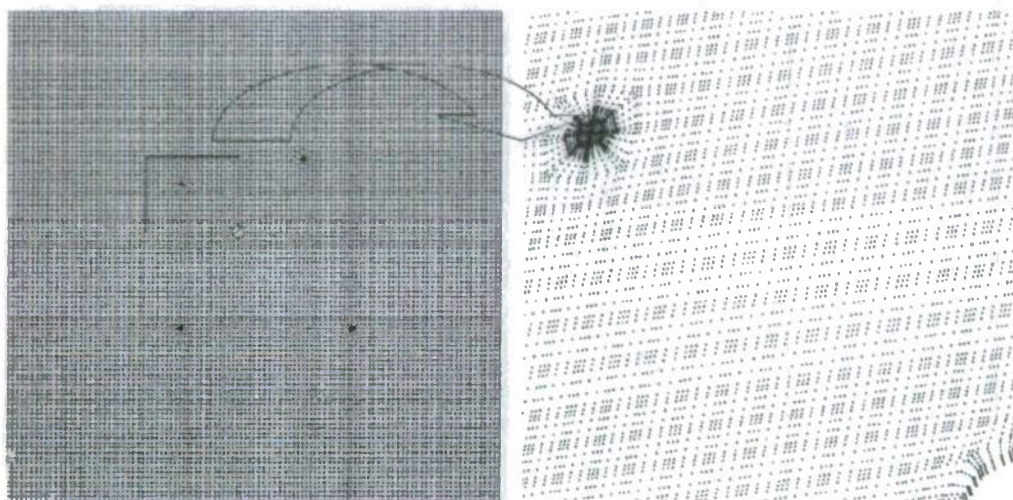
(c)

Figure 7. Square aluminum plate with hole/crack and 4 piezoelectric transducers on one side (a) geometric configuration, (b) excitation signal (450kHz), (c) mesh configuration-elements & nodes
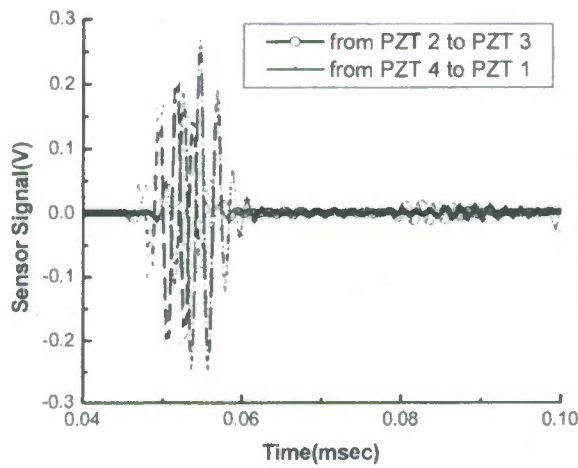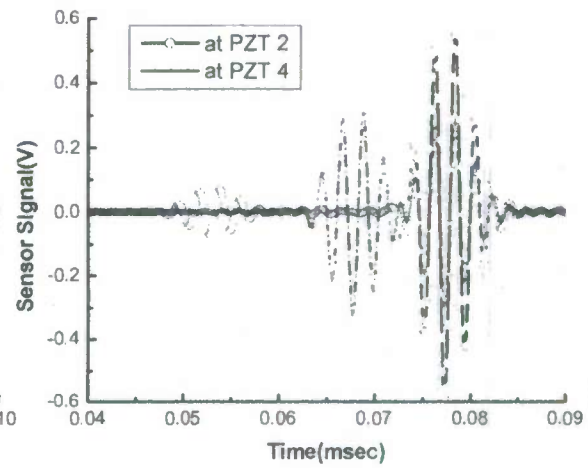
(a)　　　　　　　　　　　　　　　　(b)

Figure 8. Sensor signals obtained from (a) pitch-catch method (b) pulse-echo method
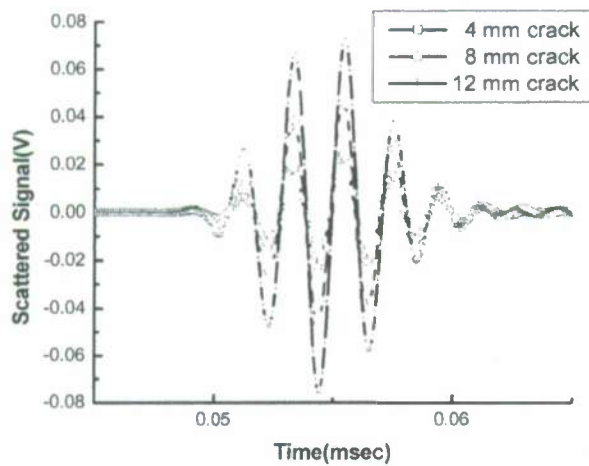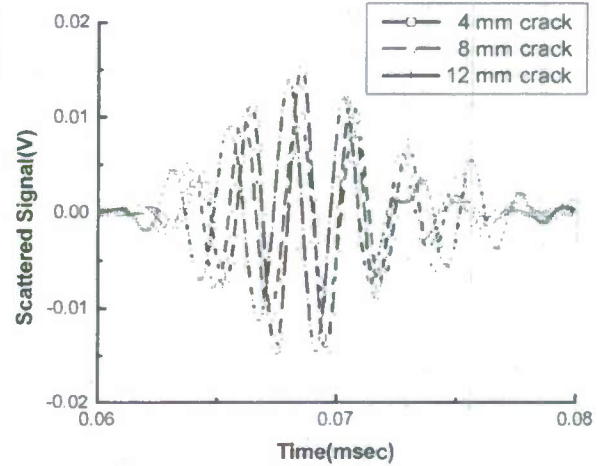
(a)　　　　　　　　　　　　　　　　(b)

Figure 9. Scatter signals of (a) pitch-catch from PZT4 to PZT1 (b) pulse-echo at PZT4

(a)
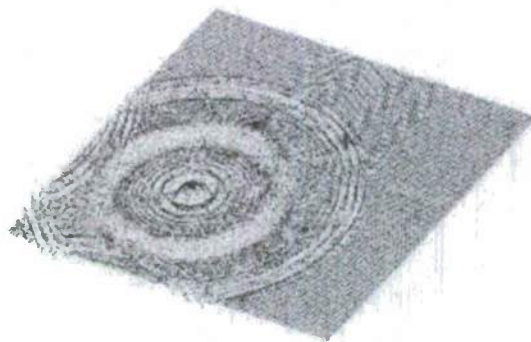
(b)

(c)
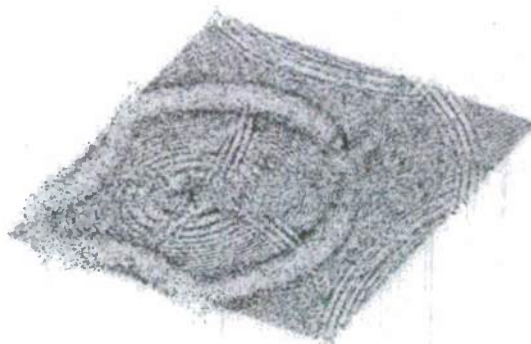
(d)

Figure 10. Wave developments at (a) 40 μsec, (b) 50 μsec, (c) 60 μsec, (d) 80 μsec
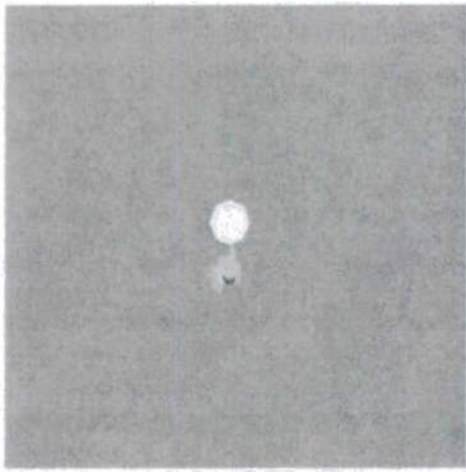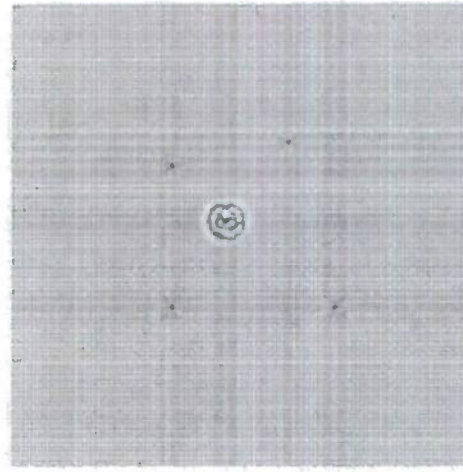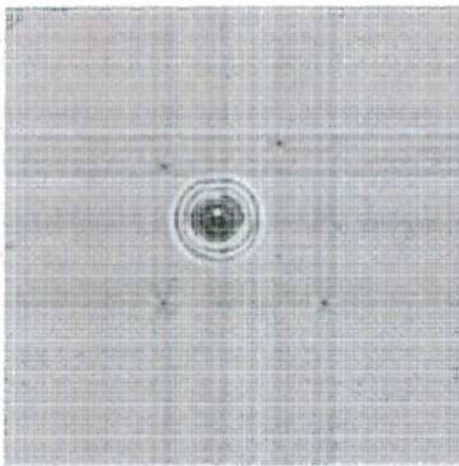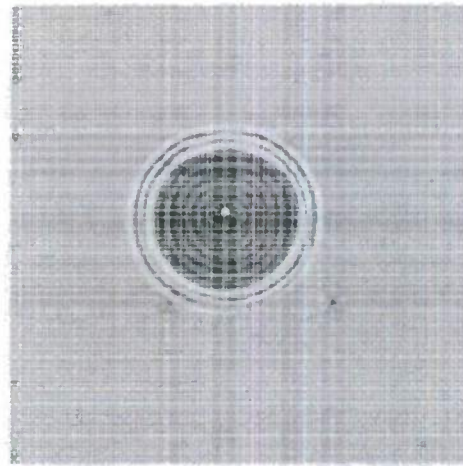
Figure 11. Scatter wave developments at (a) 20 μsec, (b) 25 μsec, (c) 30 μsec, (d) 40 μsec
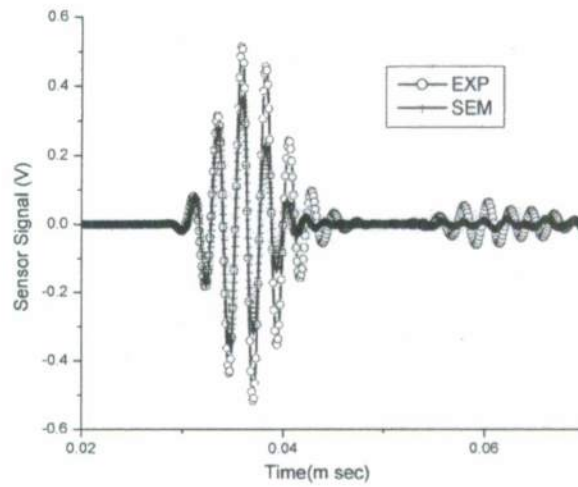
Figure 12. Sensor signals at PZT 1 (refer to Fig. 2) with 400 kHz excitation
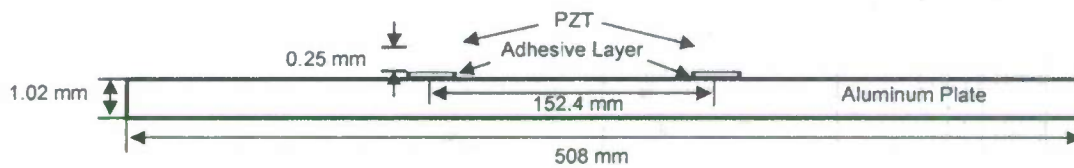
(a)
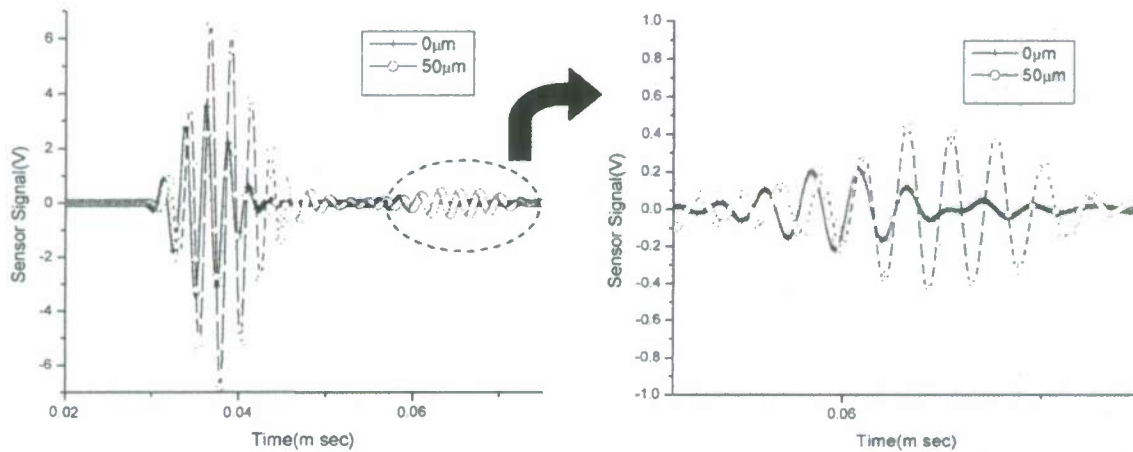
(b)

Figure 13. (a) 2D plain strain model configuration,

(b) sensor signal at 400 kHz excitation for 0μm, 50μm, adhesive layer thickness models (left), A0 mode (right)
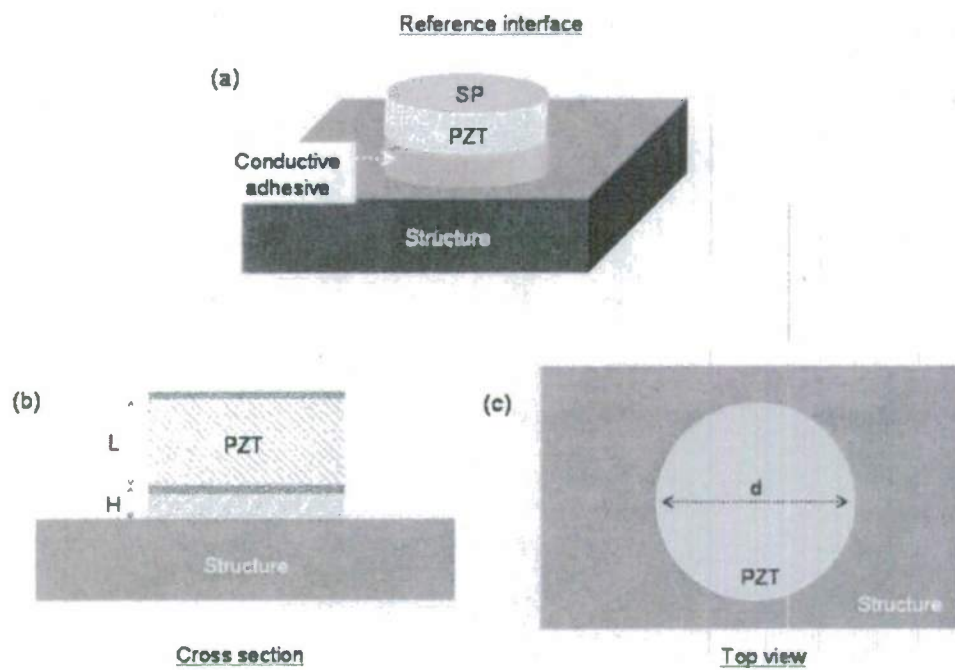
Figure 14. Reference interface of a PZT surface mounted to a structure. a) Cross section; b) Top view.
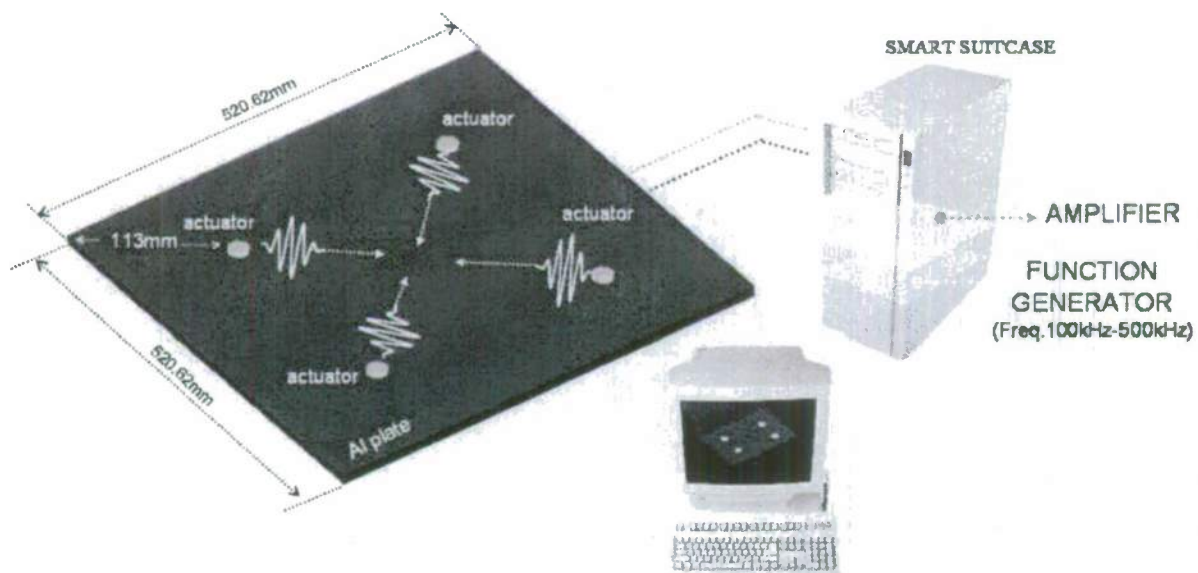
Figure 15. Test setup.
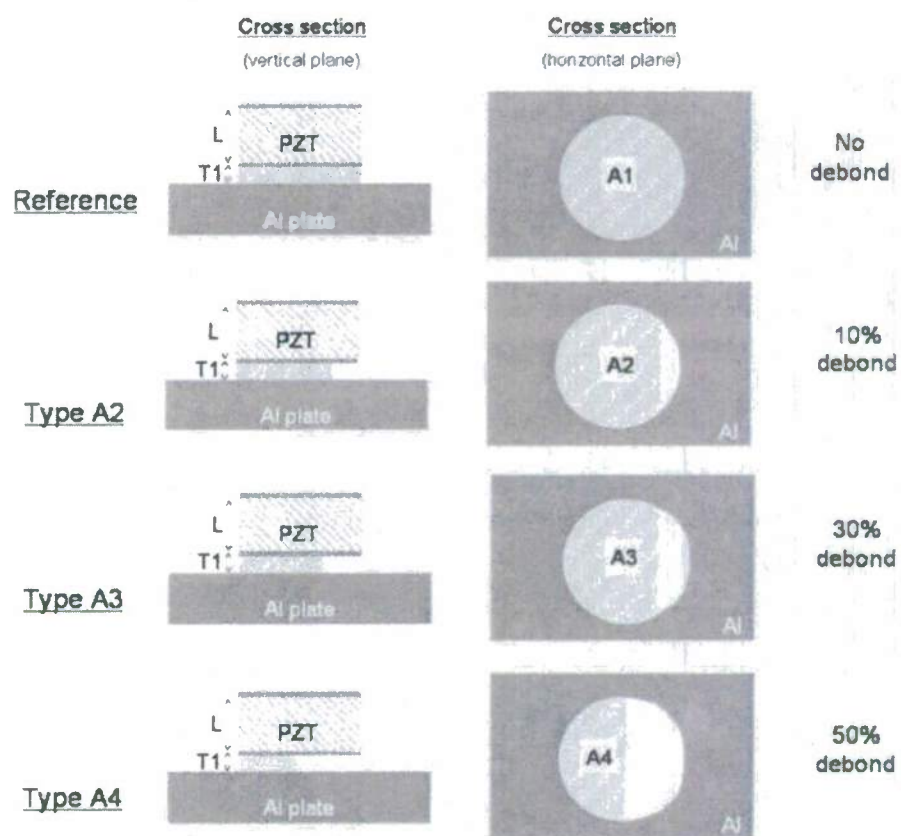
Figure 16. Set I of samples representative of an increasing debond area.
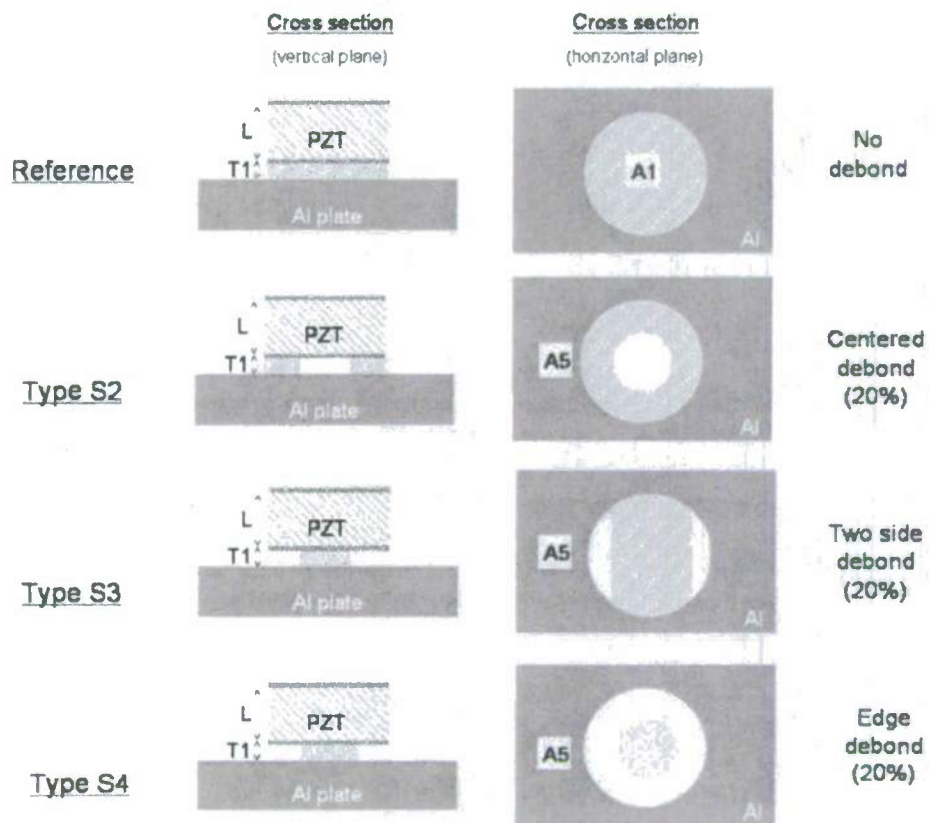
Figure 17. Set II of samples representative of different debond shapes and location.
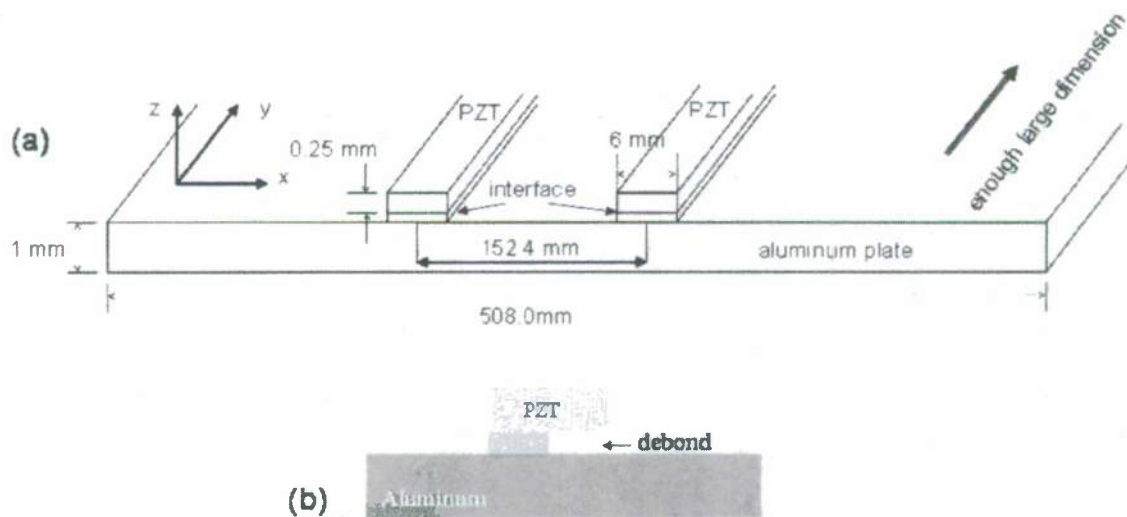
Figure 18. (a) Model to study the effect of interface debond; (b) asymmetric debond at actuator's interface.
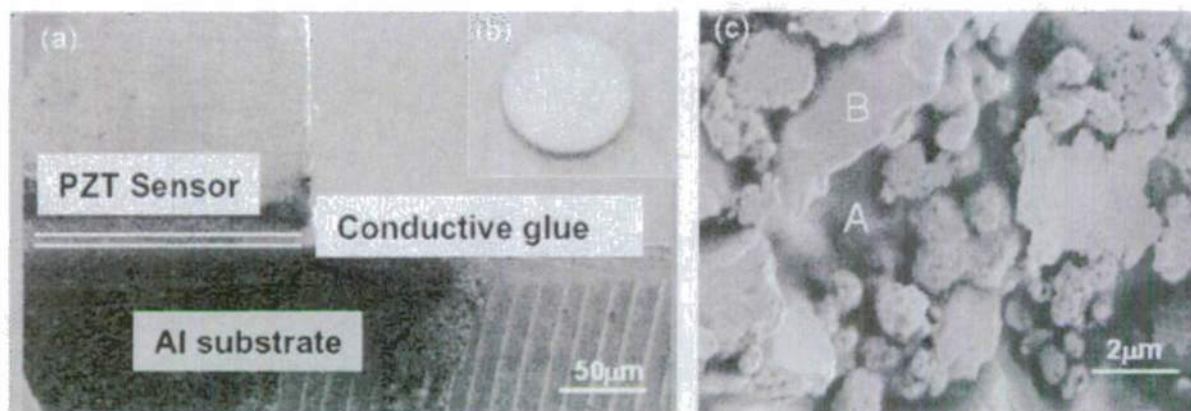
Figure 19. (a) SEM image of a PZT bonded to the Al substrate; (b) Picture of a PZT actuator; (c) SEM image of a conductive adhesive interface.
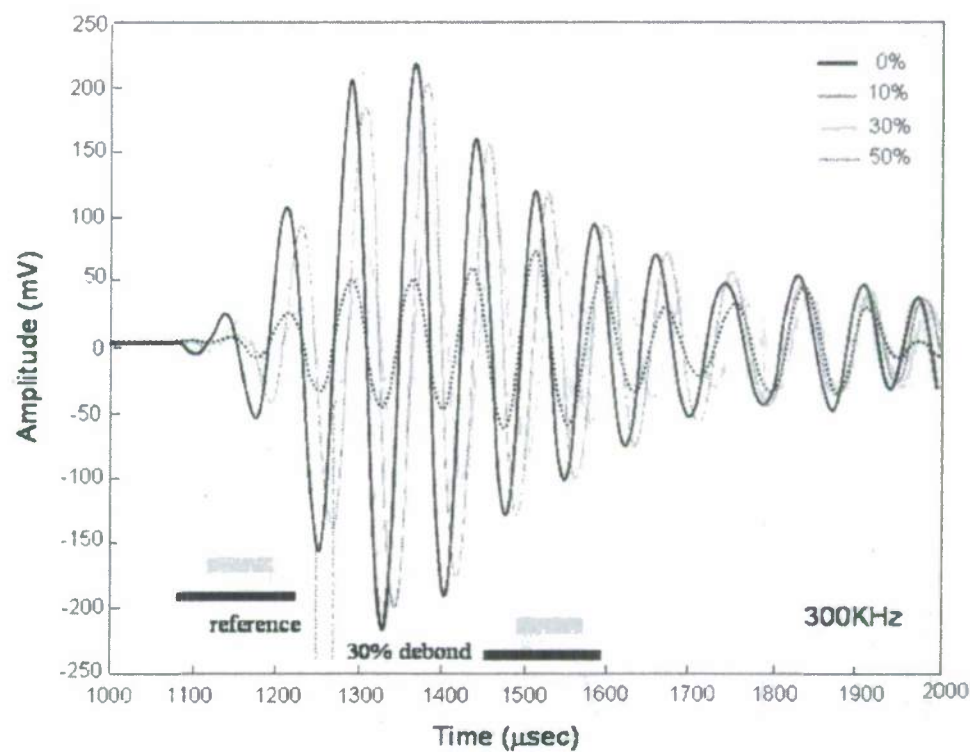
Figure 20. Sensor signal amplitude variation vs. Time.
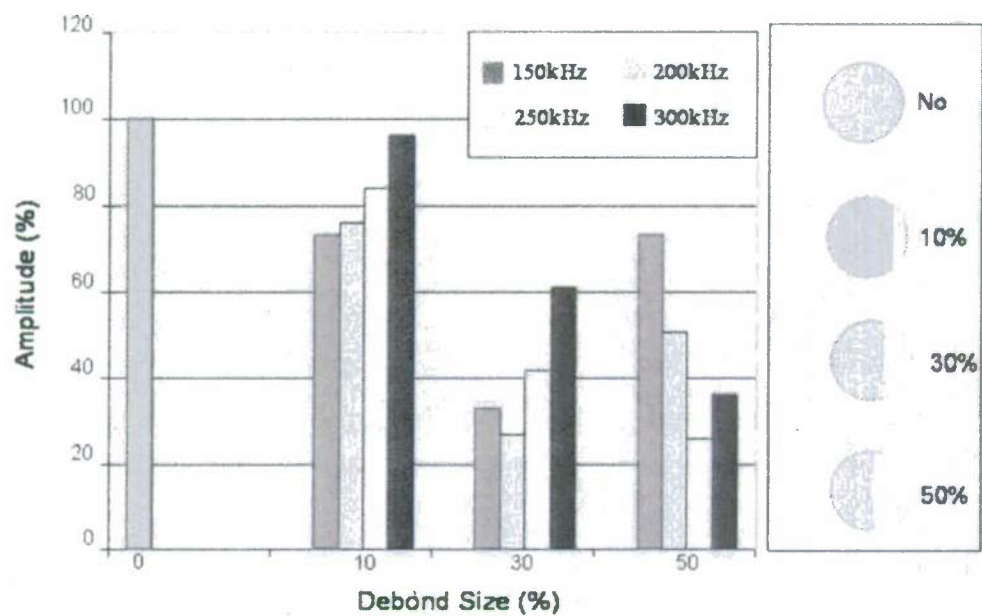
Figure 21. Amplitude variation for different debond sizes.
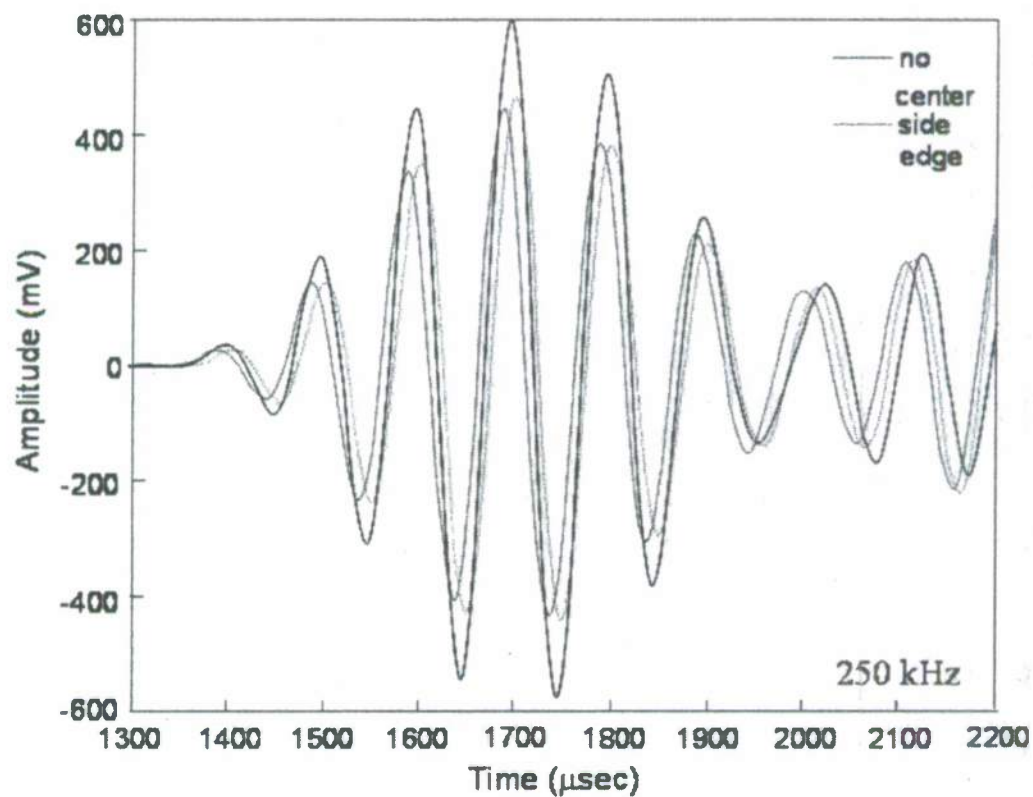
Figure 22. Sensor signal due to different debond shapes at 250KHz actuation frequency.
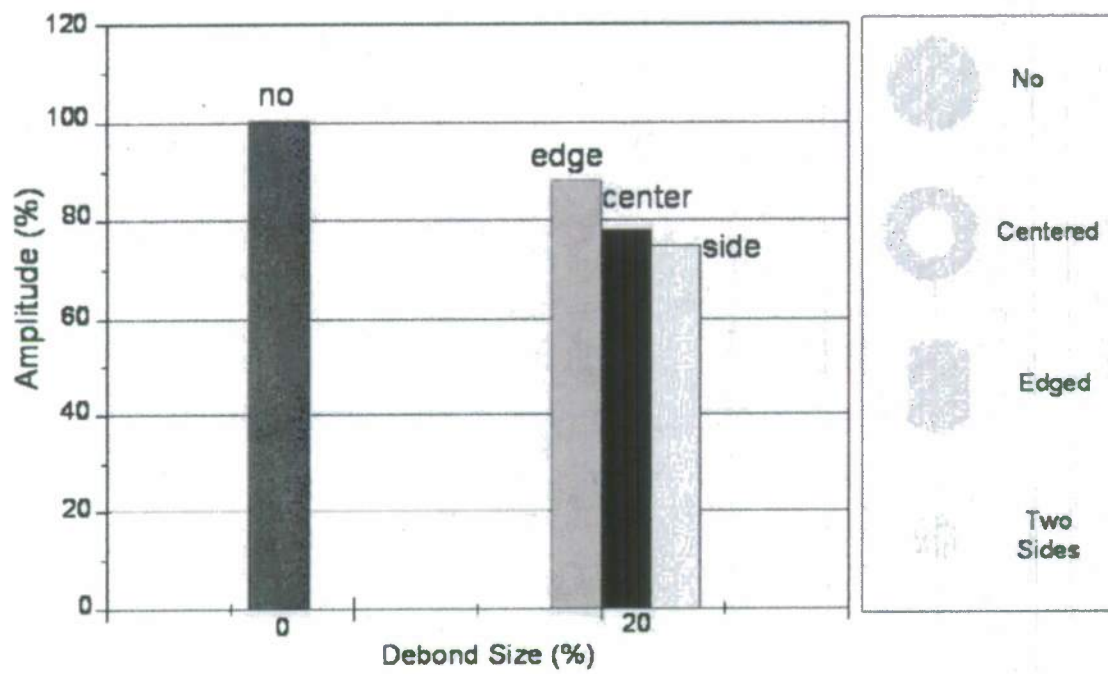
Figure 23. Effect of debond shape.
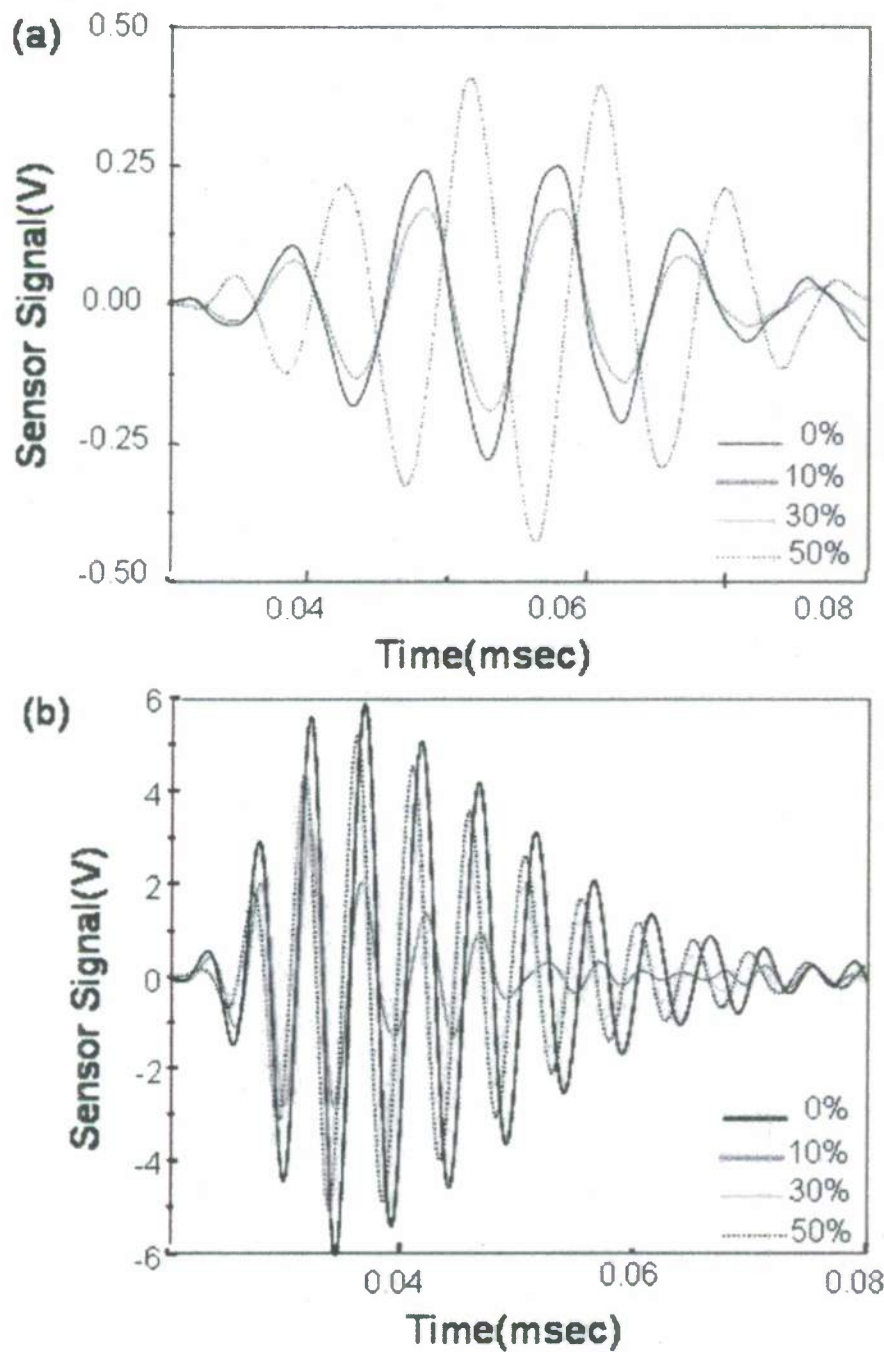
Figure 24. Sensor signal change in terms of debond size, (a) 100KHz actuation frequency, (b) 500KHz actuation frequency.
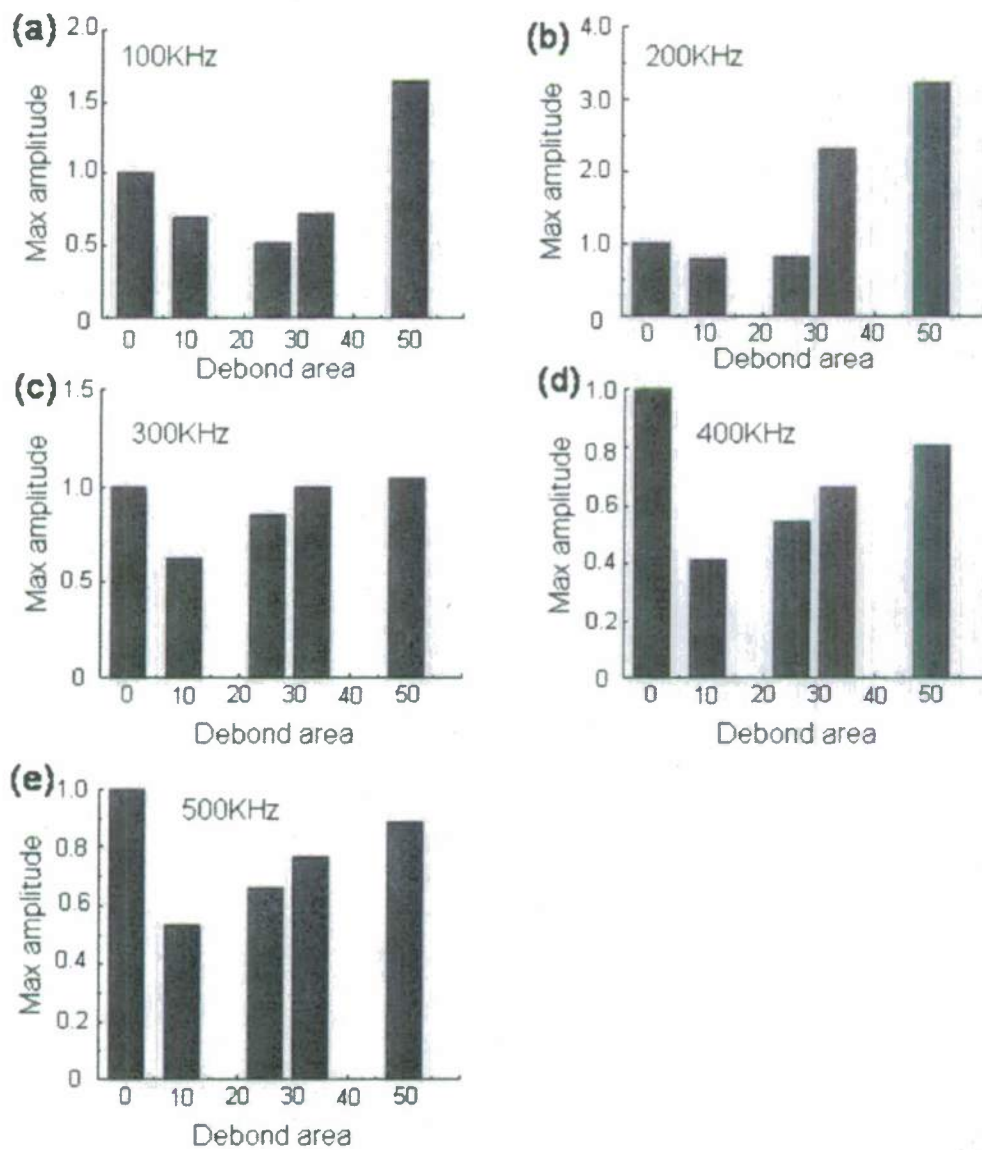
Figure 25. Maximum amplitude of sensor signal vs. debond size at different actuation frequencies.
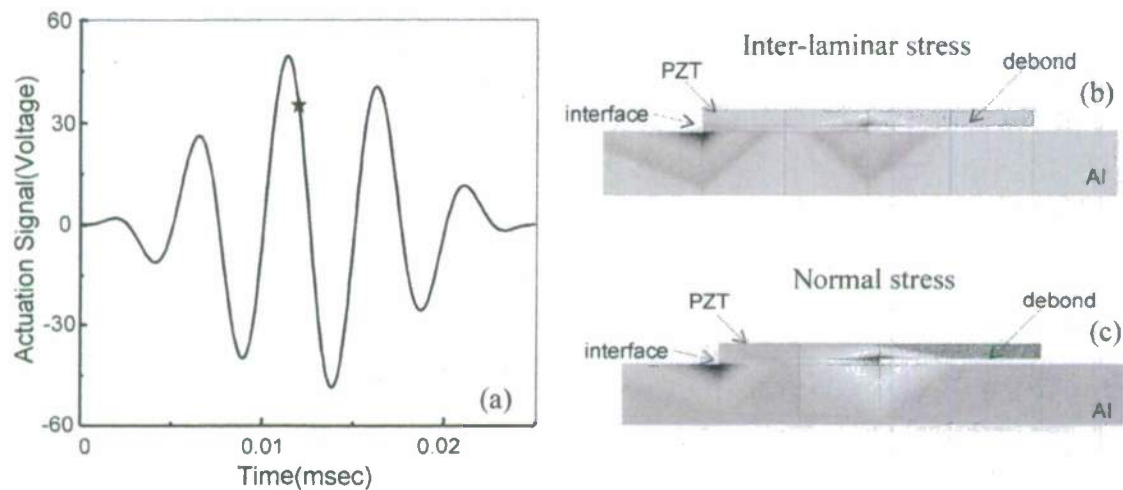
Fig.ure 26. Stress concentration at singular points: (a) actuation signal (200KHz), (b) inter-layer shear stress distribution at 12μsec, (c) normal stress distribution at 12μsec.
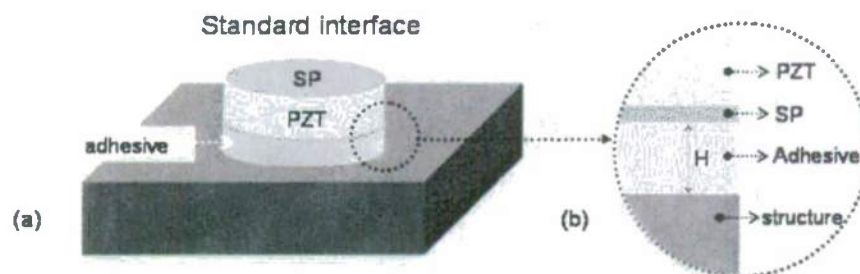
Figure 27. Standard interface: (a) PZTsurface bonded to a structure with a polymer adhesive layer, (b) details of the interface.
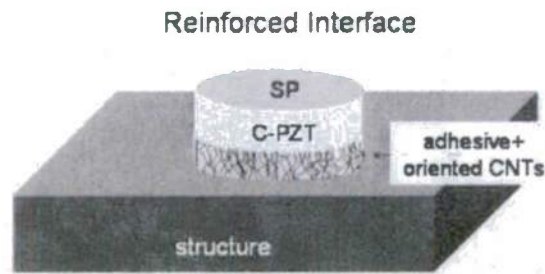
Figure 28. Interface reinforced with oriented CNTs.
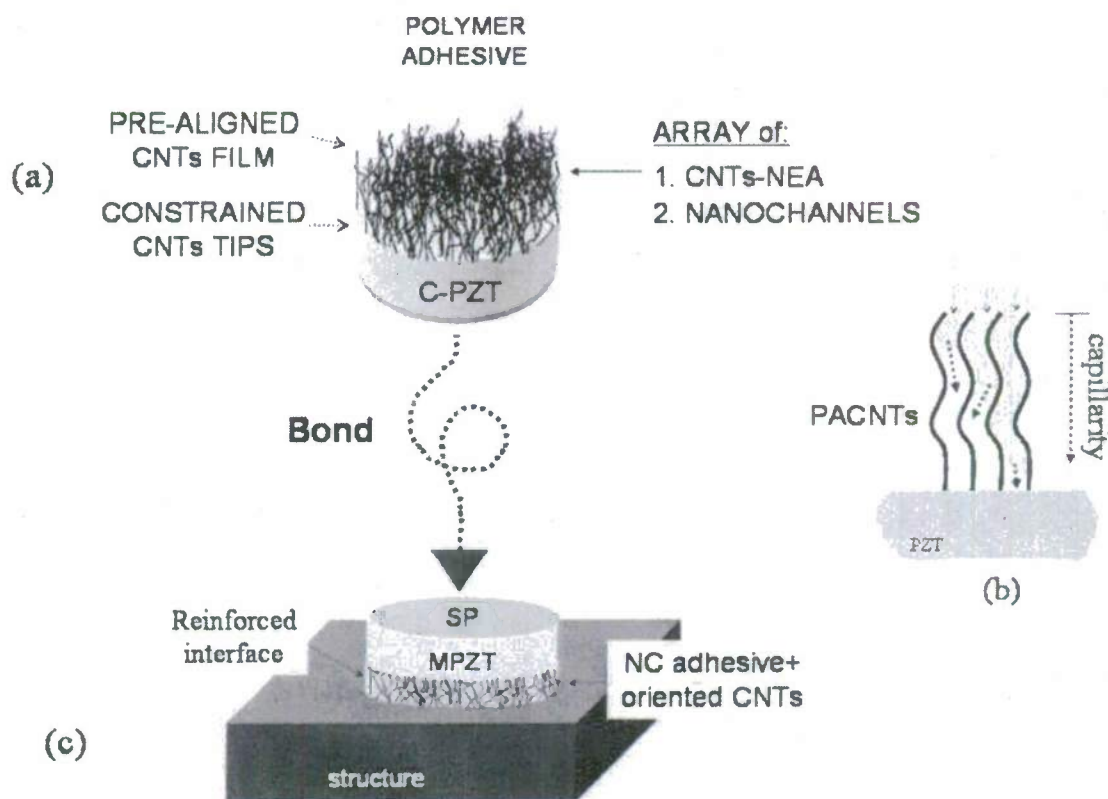
Figure 29. Scheme of the C-PZT design and fabrication approach.
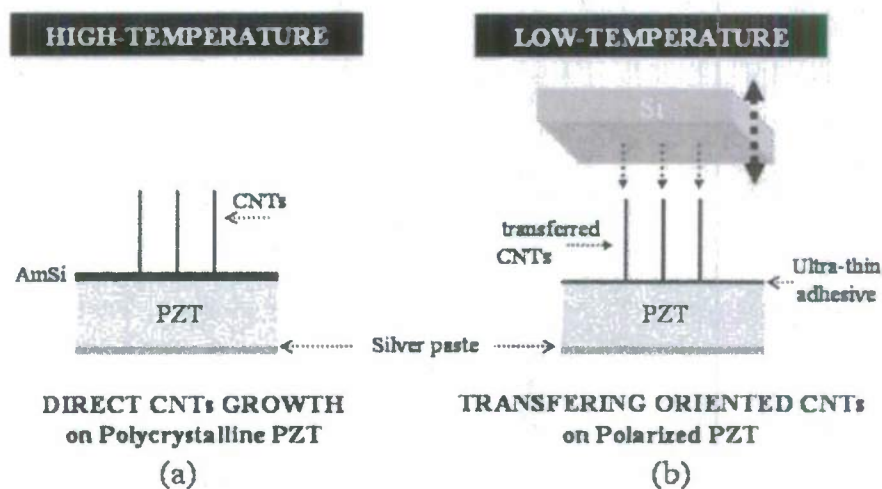
Figure 30. Schematic of the low and high temperature process for PZT coating with a PACNTs carpet: (a) high-temperature process, (b) room temperature process.
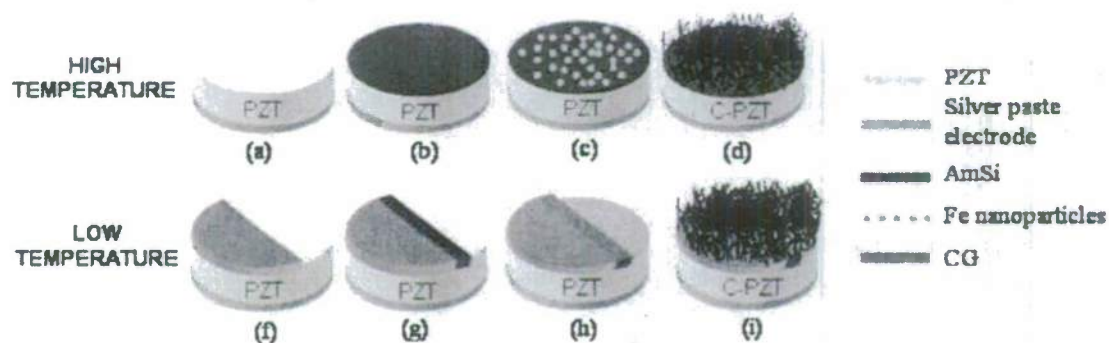
Figure 31. Scheme of the high and low temperature process for the realization of an MPZT. High temperature: (a) PZT peeling, (b) AmSi layer coating (c) Fe nanoparticles deposition, (d) CNTs growth. Low-temperature process: (f) PZT peeling, (g) AmSi deposition, (h) CG coating, (i) CNTs transfer.
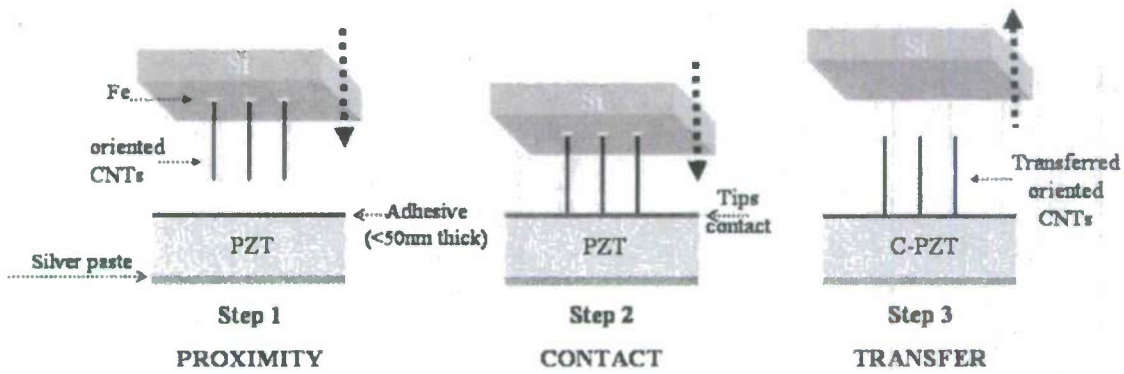
Figure 32. Transfer method.
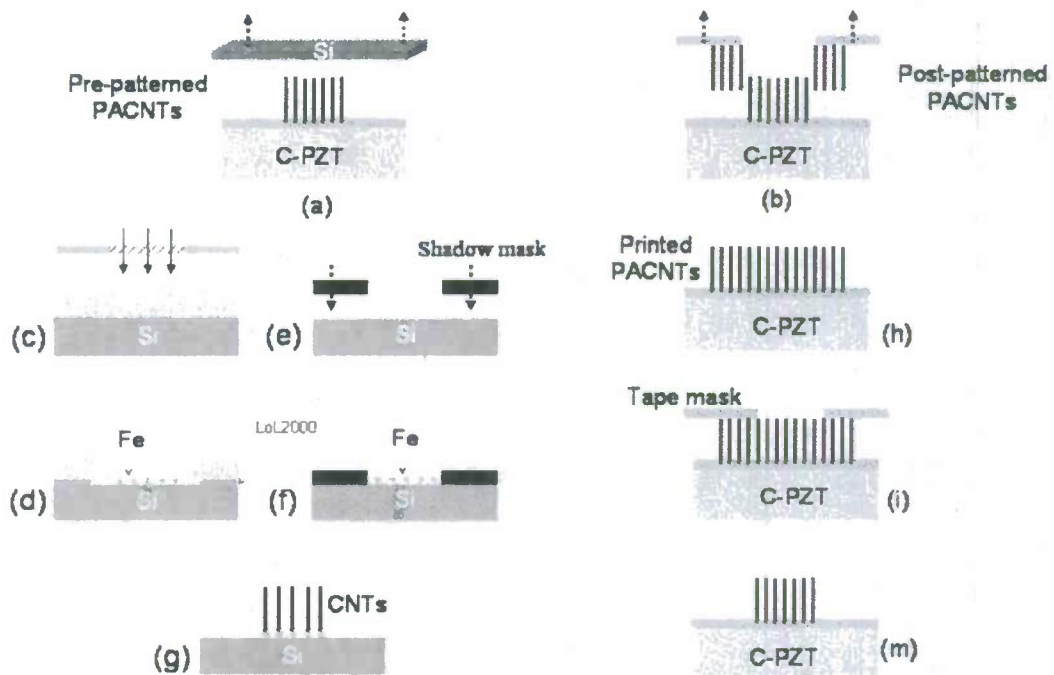
Figure 33. Scheme of the patterning process.
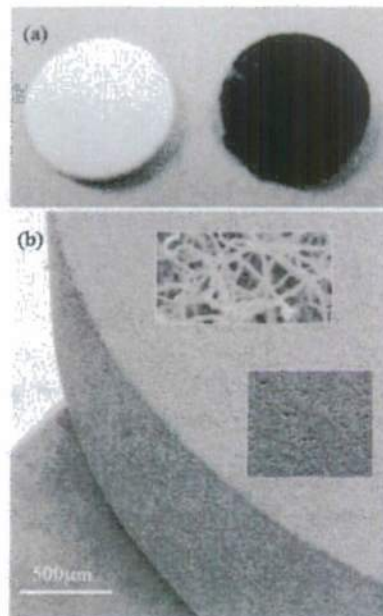
Figure 36. C-PZT: results from the high-temperature approach: (a) picture of a PZT before and after CNTs growth, (b) SEM image of the PZT after CNTs growth.
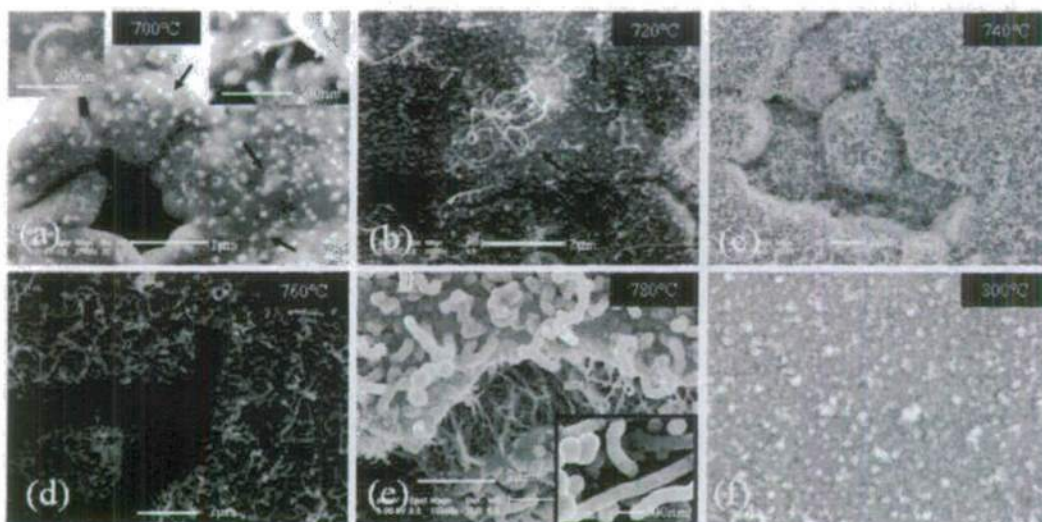
Figure 37. SEM images of CNTs growth results vs. increasing temperature. The substrates are PZT (diameter of 10mm and thickness of 1mm) coated with a SiO_2 layer.
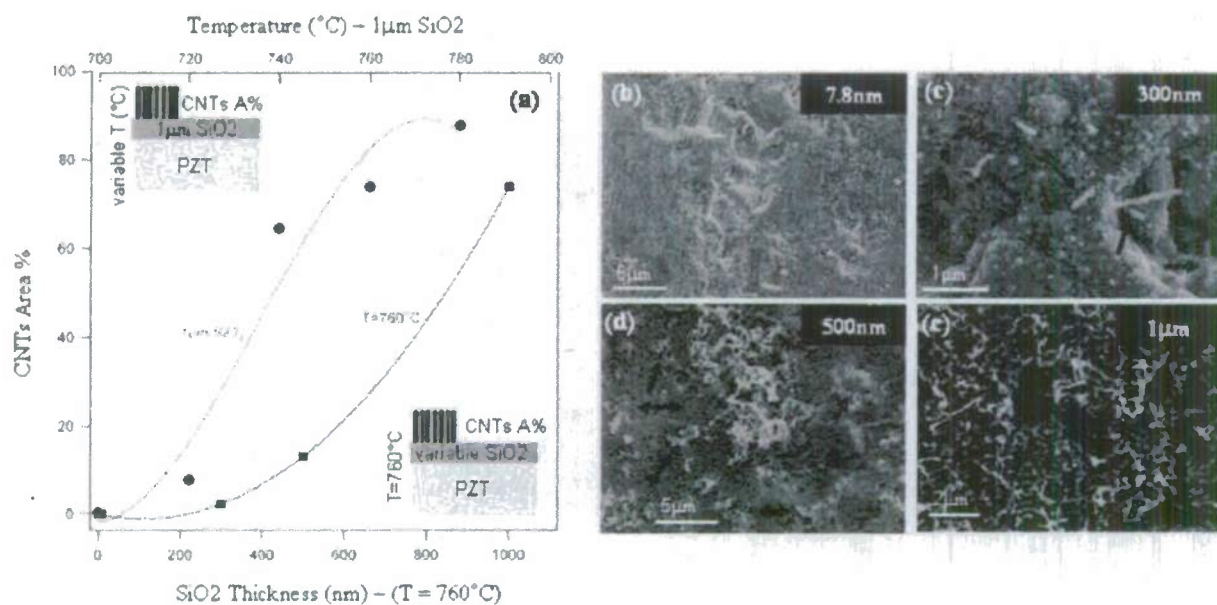
Figure 38. (a) Experimental results for CNTs growth on PZT with increasing temperature and increasing thickness. (b),(c),(d),(e) SEM images of PZT samples grown at 760°C and with increasing SiO$_2$ layer thickness.
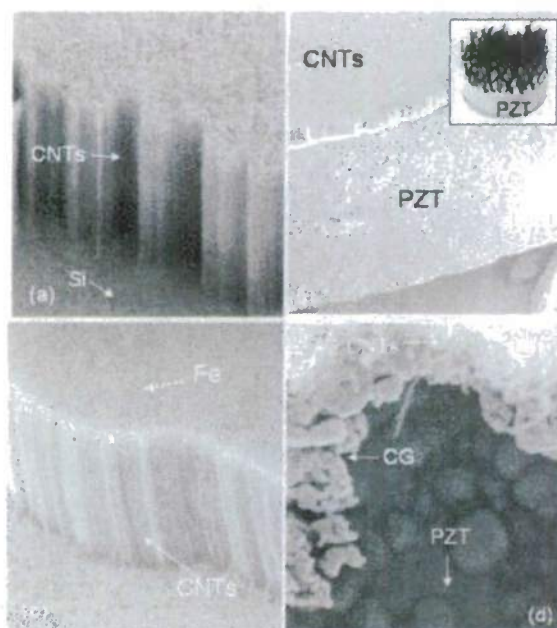
Figure 39. C-PZT: results of the low temperature approach: (a) carpet of oriented CNTs grown on a Silicon chip, (b) CNTs carpet transferred onto a bare PZT surface, (c) higher magnification of the transferred CNTs, (d) top view of the edge of the CNTs carpet. The image shows: the PZT grains, the CG layer and the CNTs carpet.
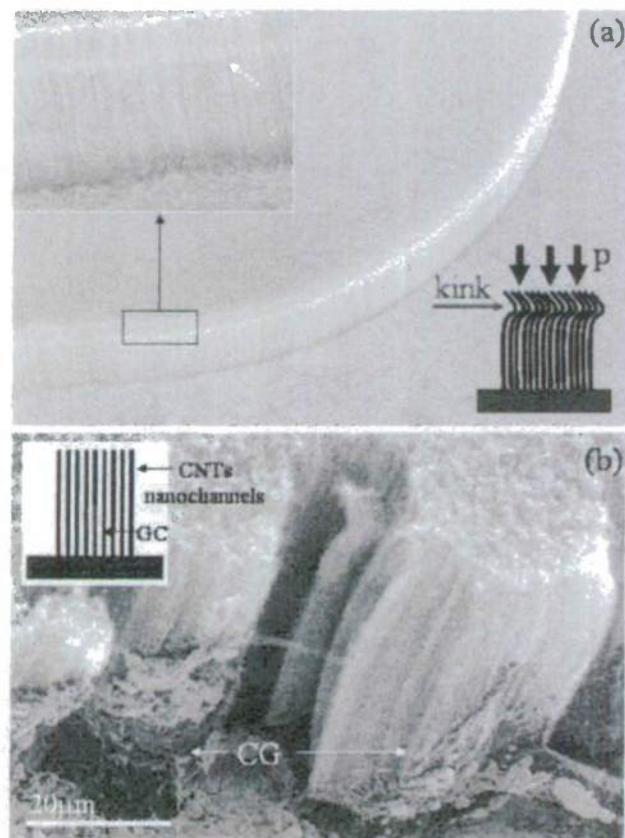
Figure 40. Key elements for the printing process: (a) plastic deformation due to excessive pressure (p), (b) CG absorption.
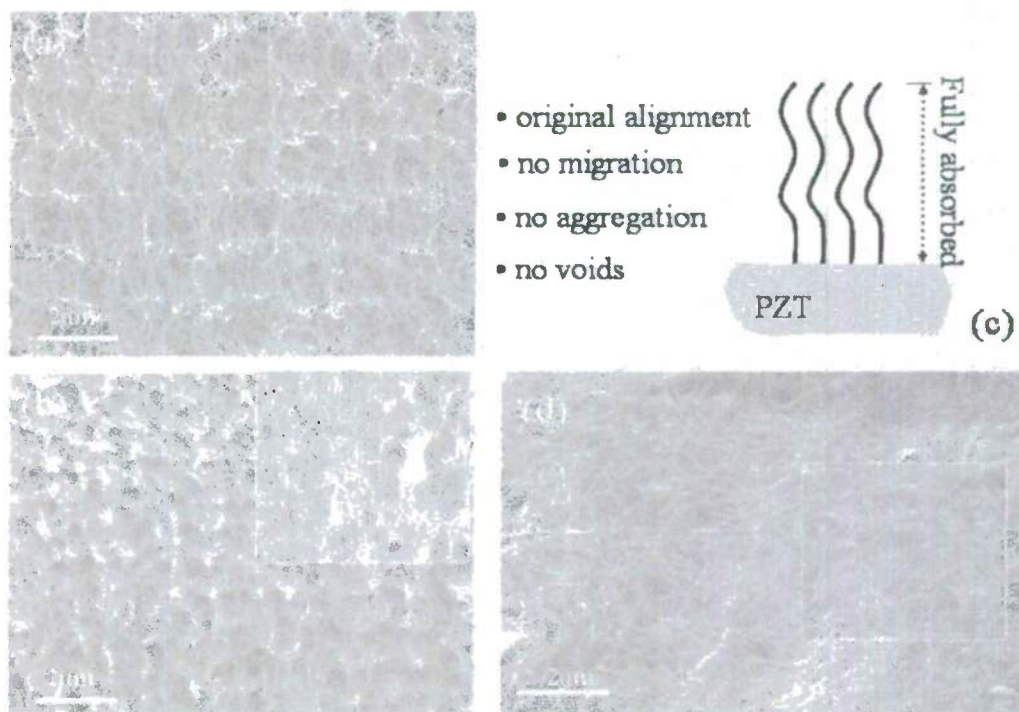
Figure 41. (a) Wavelike configuration of a PACNTs carpet transferred onto a PZT surface, (b) carpet embedded into the adhesive polymer, (c) scheme of the embedding result, (d) top view of the embedded CNTs carpet.
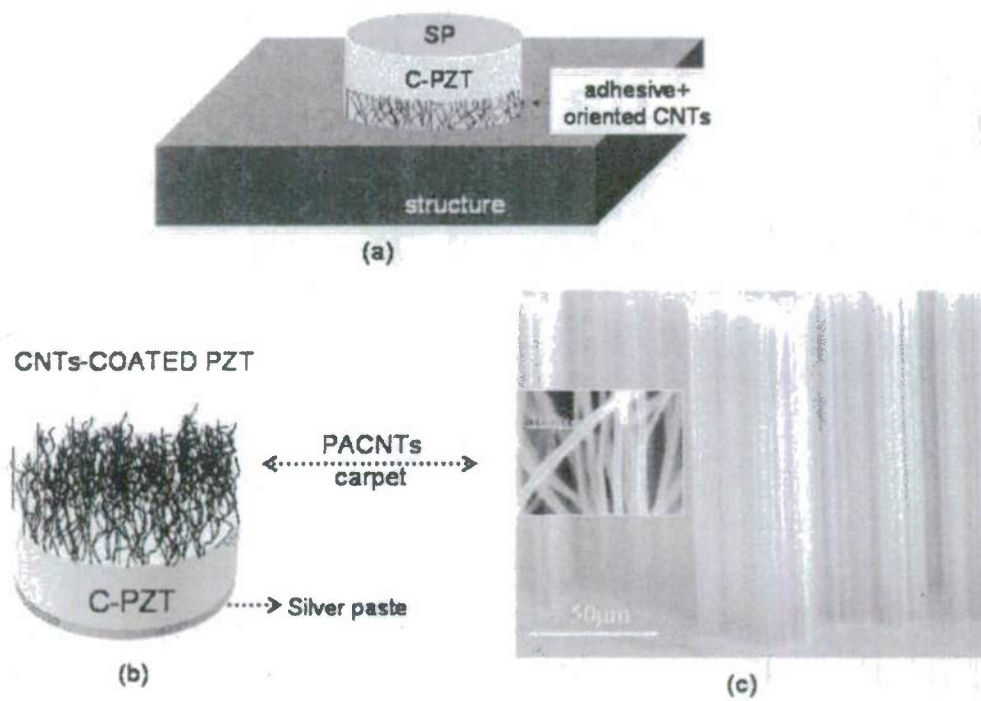
Figure 42. (a) Interface integrated with a PACNTs carpet. (b) PZT coated with a PACNTs carpet, (c) SEM image of a PACNTs carpet
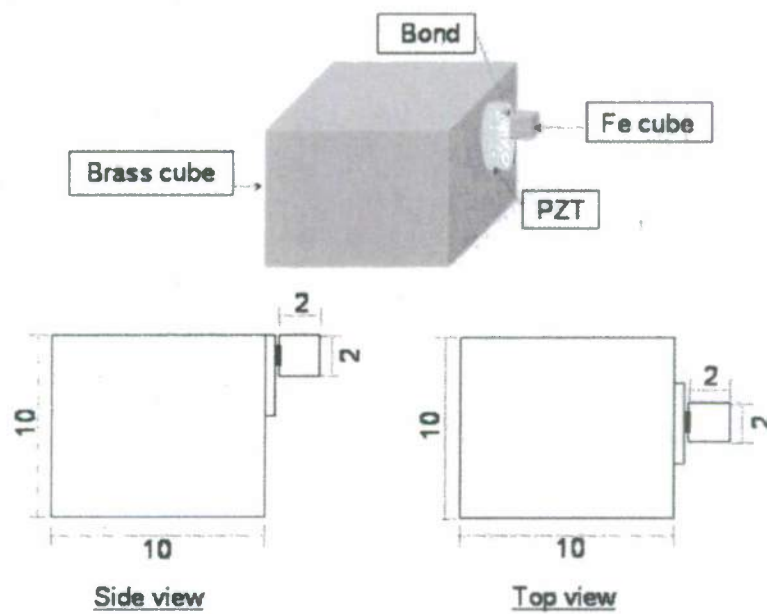
Figure 43. Samples design.
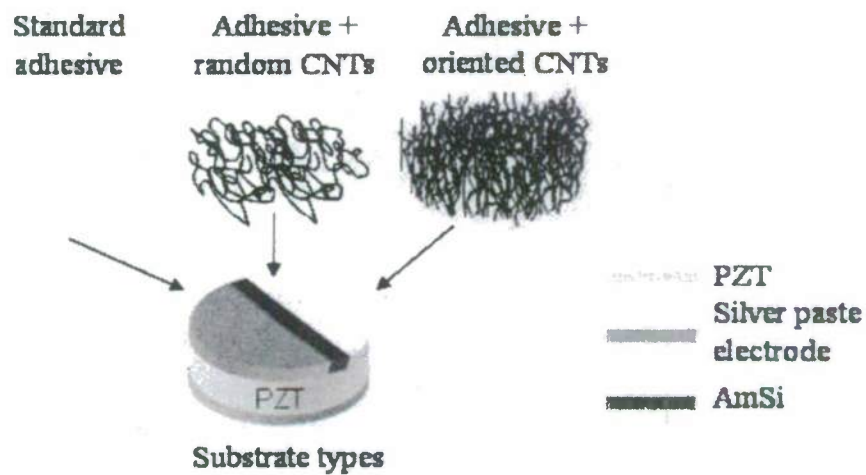
Figure 44. Substrate types and adhesive compositions.
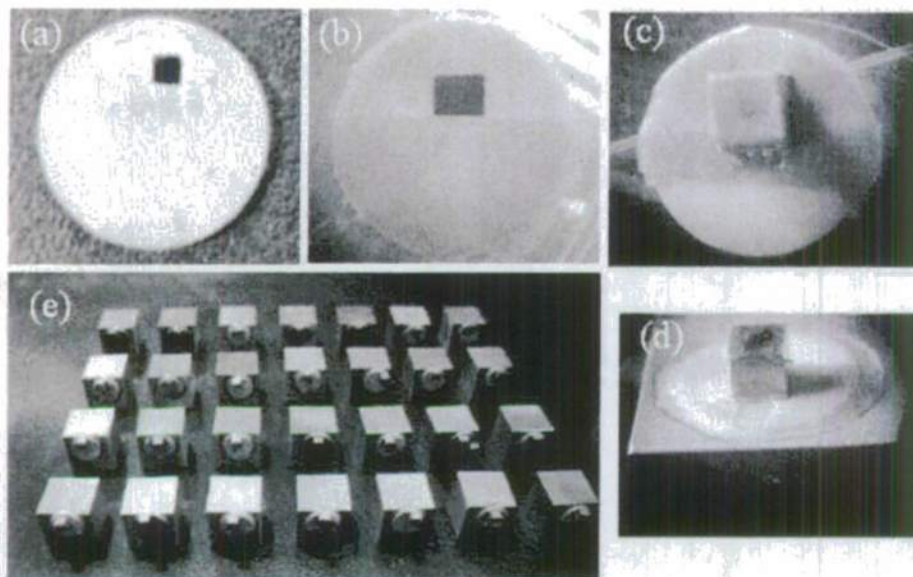
Figure 45. Samples preparation: (a) pre-patterned oriented CNTs transferred onto the PZT surface, (b) Teflon mask to confine the area of post-patterned CNTs, (c) iron cube bonded to the PZT, (d) PZT bonded to the Brass cube, (e) example of the as fabricated samples.
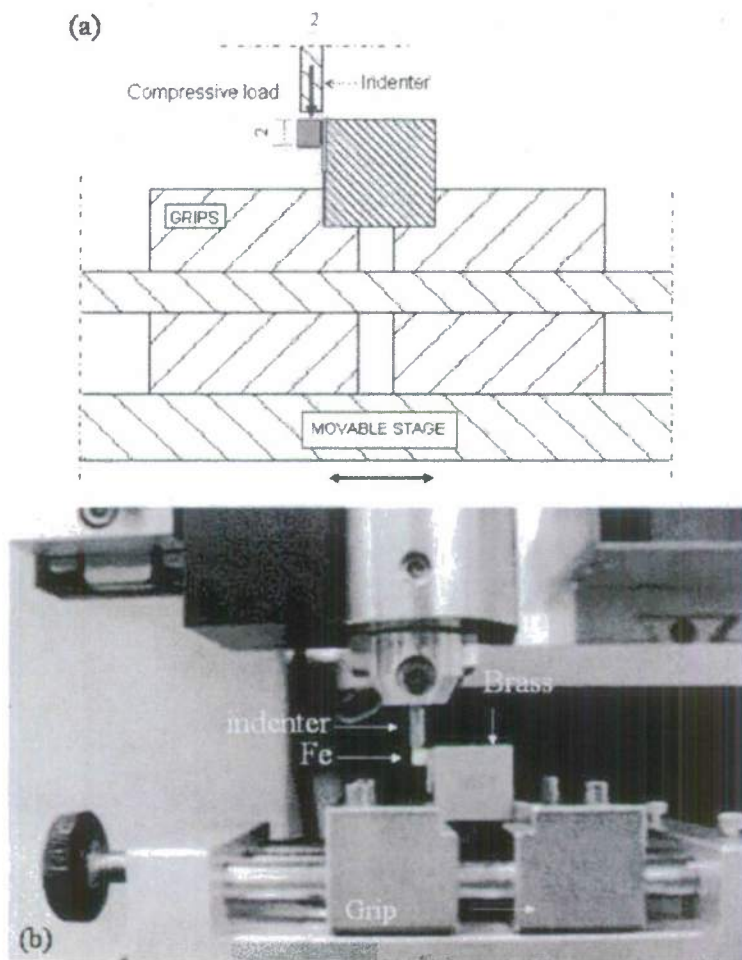
Figure 46. MHT set-up: (a) scheme of the test, (b) picture of a sample during testing.
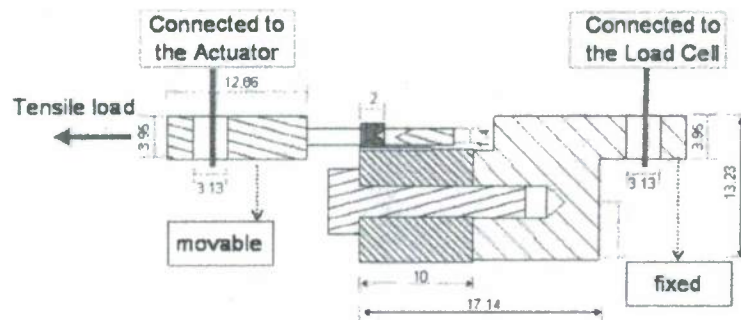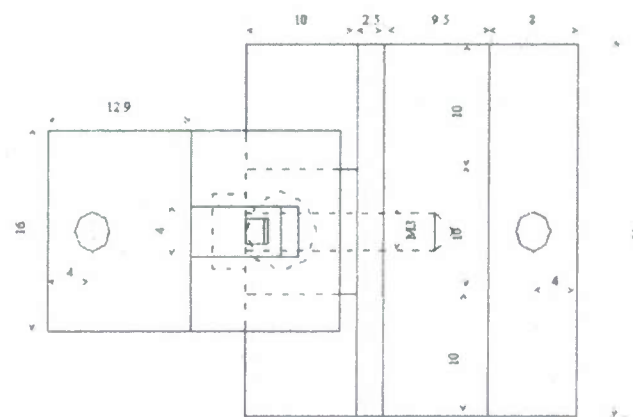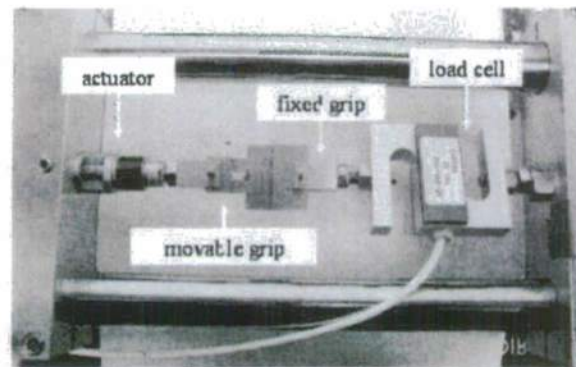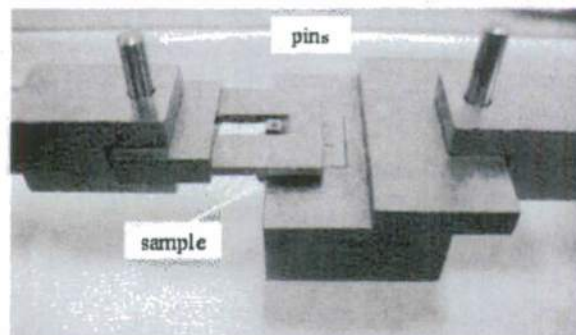
Figure 47. Delaminator set-up: (a) scheme of the features design and test set-up, (b) picture of the Delaminator components during testing, (c) higher magnification of the sample and test set-up during testing.
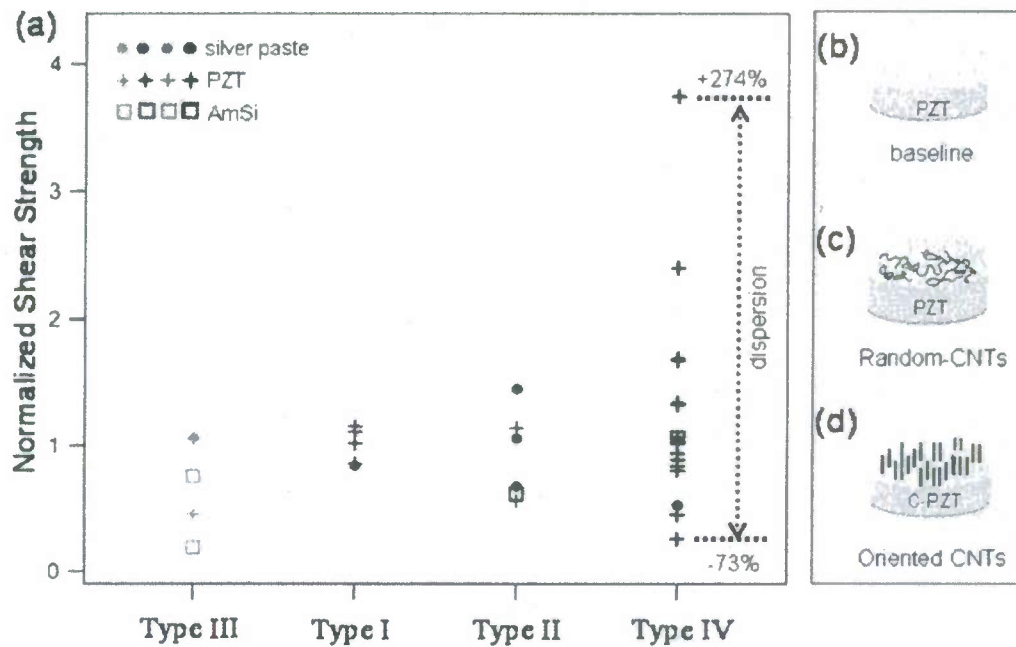
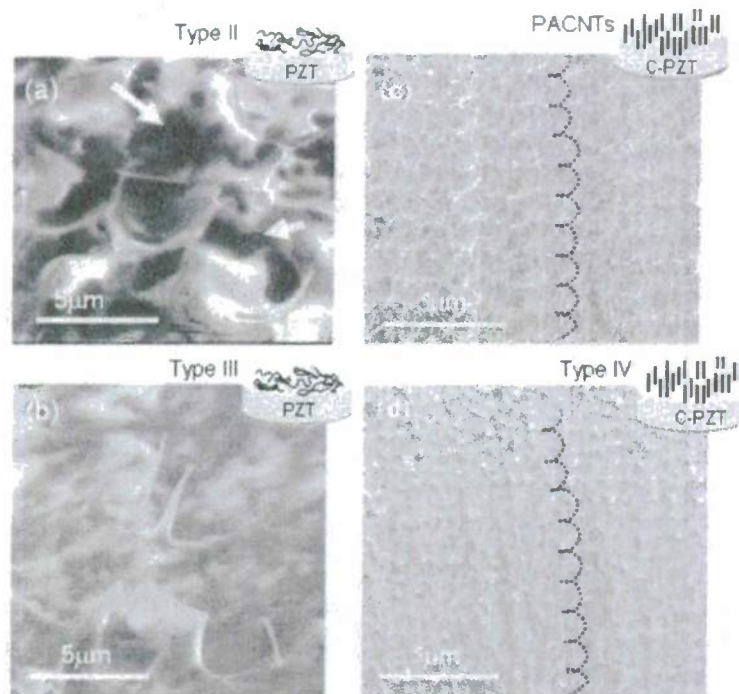**Figure 48.** (a) Shear strength vs. adhesive composition, (b), (c) and (d) adhesive compositions.

Figure 49. SEM images of samples with different adhesive compositions: (a) adhesive mixed with random CNTs (Type II), (b) adhesive mixed with random CNTs (Type III), (c) side view of adhesive integrated with a high density array of oriented CNTs (Type IV).
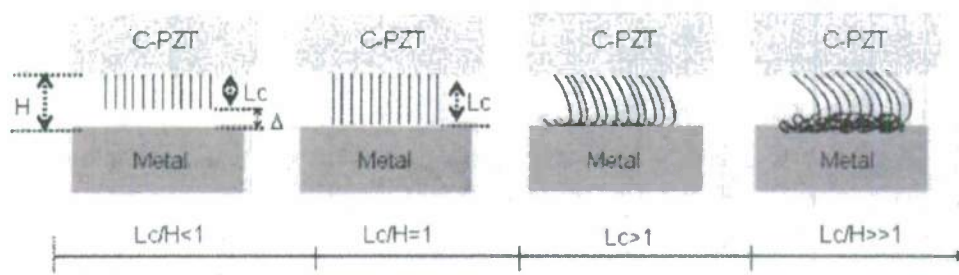
Figure 50. Different bondline microstructures for increasing Lc/H ratio.
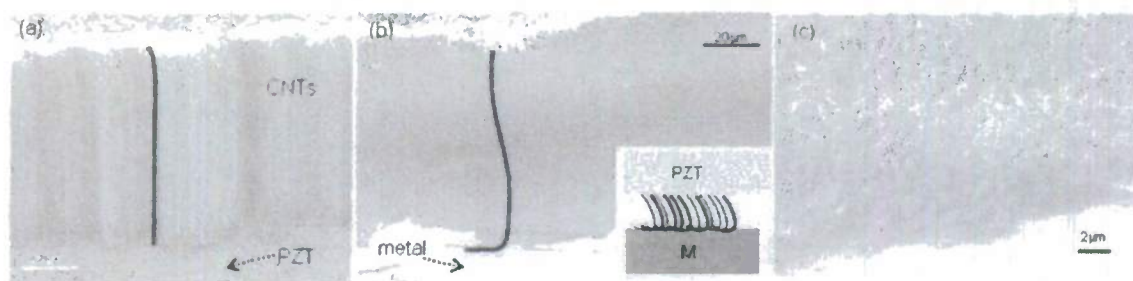

Figure 51. Bonding effect, SEM pictures: (a) PACNTs prior embedding, (b) side view of a bond, (c) folding effect. The sample in analysis has a ratio 1.1.
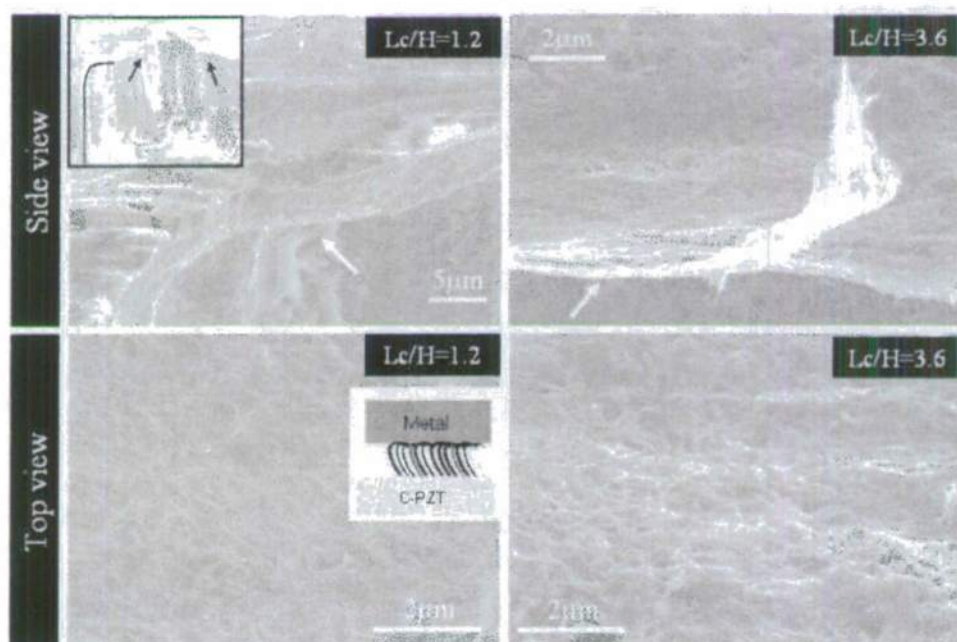
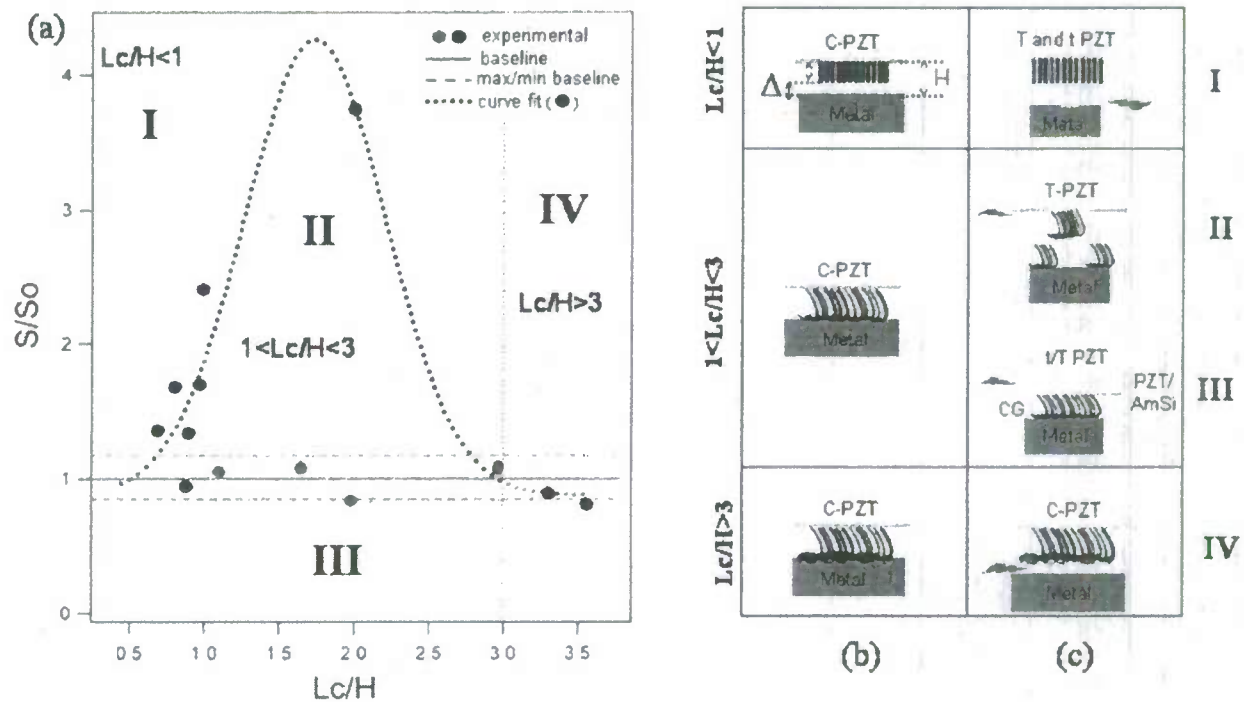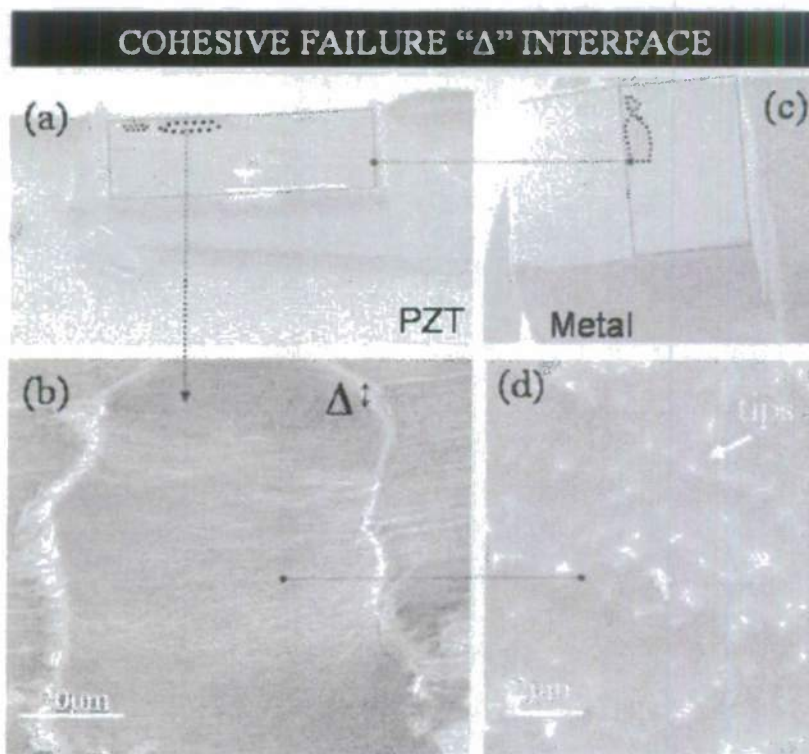**Figure 52.** SEM images of the folding effect increase for higher Lc/H ratios.

**Figure 53.** a) Normalized Shear strength vs. Lc/H. (b) Sample types, (c) failure modes corresponding to each sample type.

Figure 54. Cohesive failure for samples with Lc/H<1: (a) SEM image of the PZT surface, (b) fracture of the Δ interface, (c) iron cube, (d) higher magnification of the adhesive inside the fractured area.
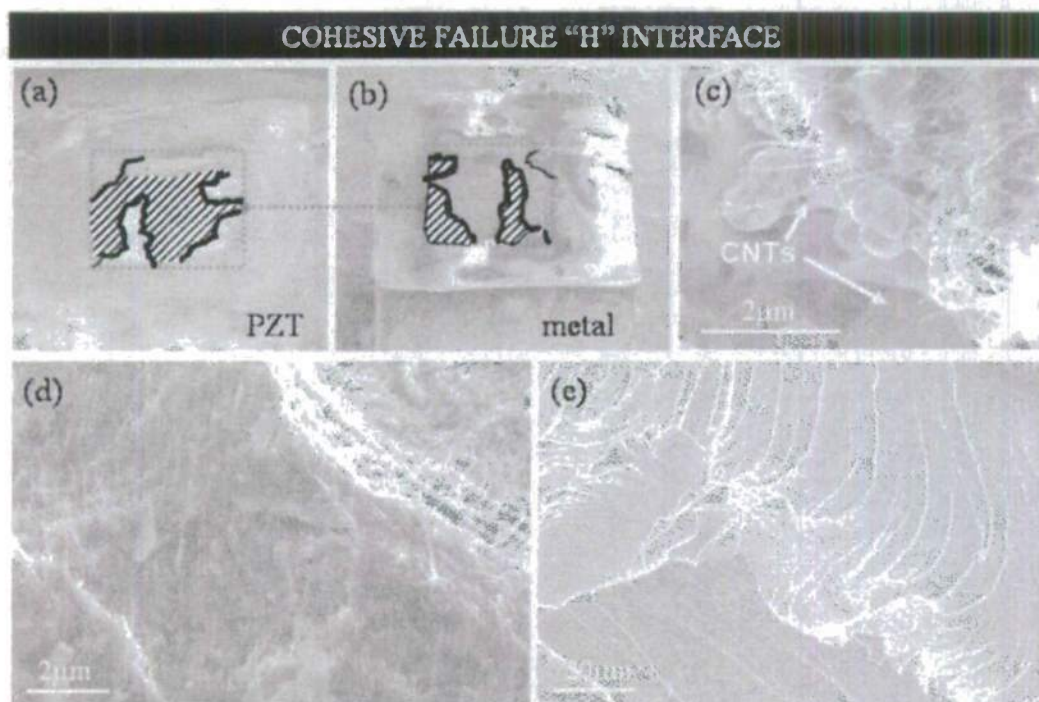
Figure 55. SEM images of a sample characterized by cohesive failure of the "*H*" interface: a) PZT surface, (b) metal surface, (c) CNTs tips sticking out of a fractured surface, (d) multidirectional fractured surfaces, (e) fractured surface.
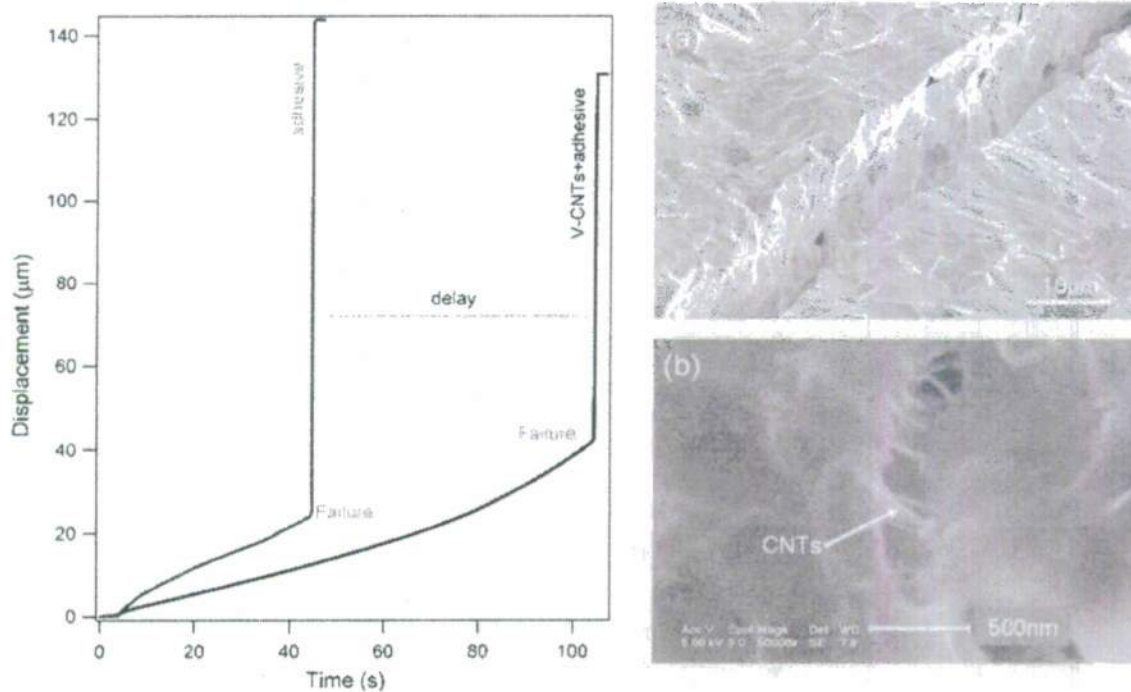
Figure 56. Displacement vs. time curve for a baseline adhesive polymer and for a nanocomposite polymer integrated with oriented CNTs. (a) SEM image of a fracture propagating in a baseline adhesive, (b) SEM image of a fracture propagating in an adhesive polymer integrated with CNTs.
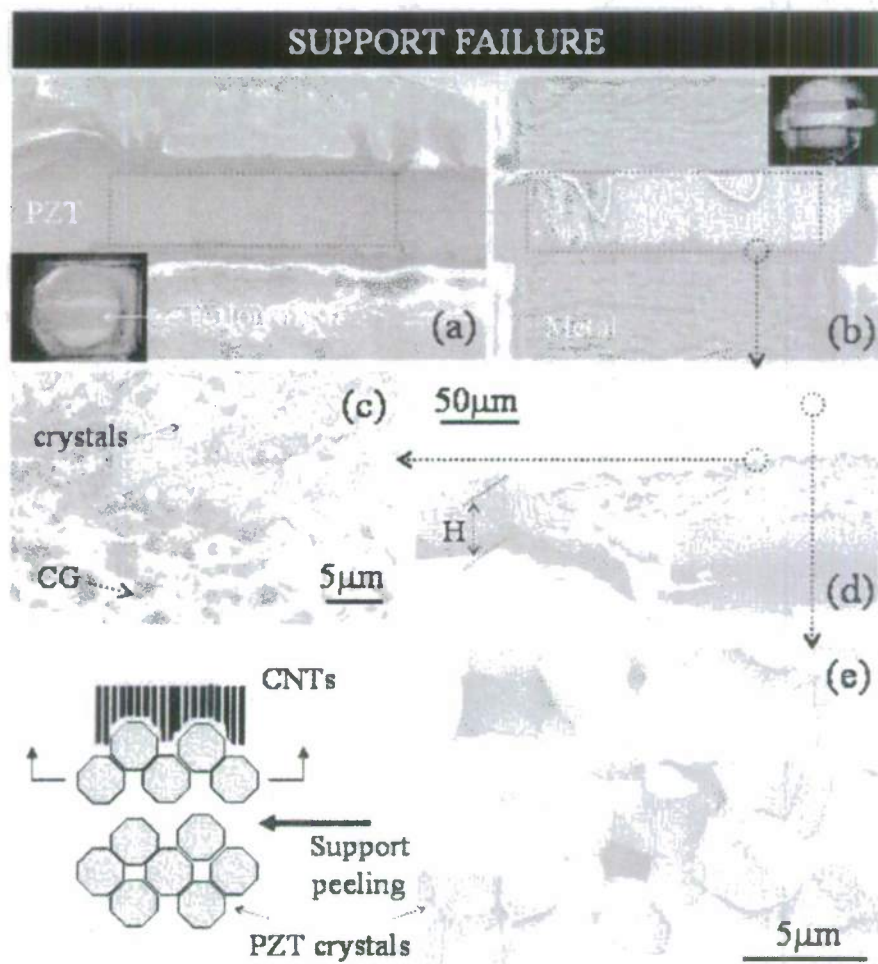
Figure 57. Support failure mechanism: (a) SEM image of the PZT surface, (b) SEM image of the metal surface, (c) top view of the interface in contact with the PZT, (d) 45° view of the nanocomposite bond left on the metal surface, (e) higher magnification of the PZT crystals peeled from the PZT substrate and scheme of the peeling mechanism.
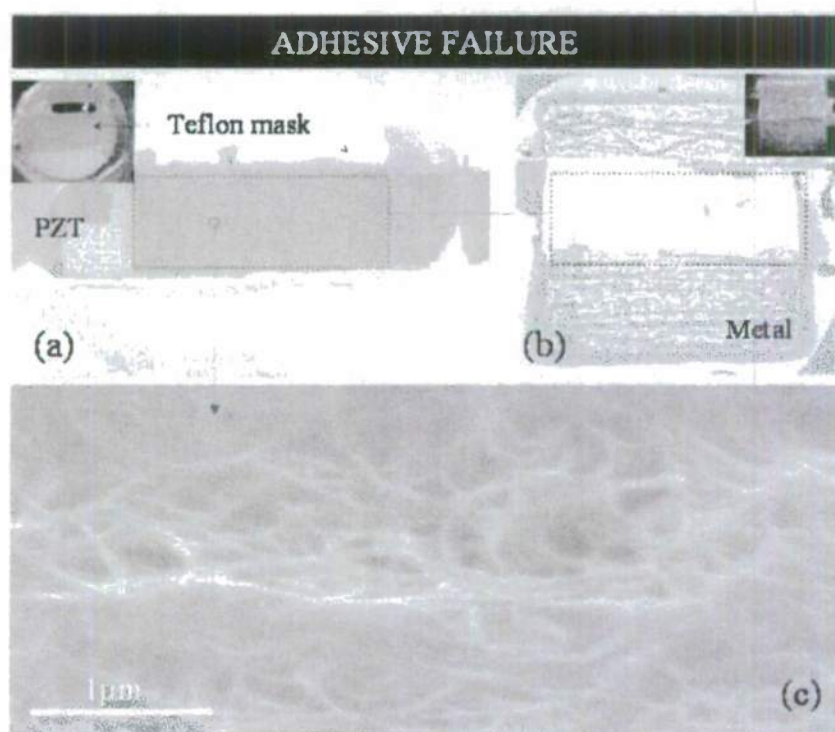
Figure 58. SEM images of the adhesive failure: (a) PZT surface, (b) metal surface, (c) contact interface metal-bond.

REFERENCES

[1] Roh, Y. S. and Chang, F. K., "Built-in Diagnostics for Identifying an Anormaly in Plate Using Wave Scattering," Ph.D. Dissertation, Aeronautics and Astronautics Dept., Stanford University, Stanford, CA, 1999.

[2] Kessler, S. S., Spearing, S. M., and Soutis, C., "Structural Health Monitoring in Composite Materials Using Lamb Wave Methods," *Smart Mater. Struct.,* Vol. 11, 2002, pp. 296-278.

[3] Ihn J. B. and Chang, F. K., "Detection and Monitoring of Hidden Fatigue Crack Growth Using a Built-in Piezoelectric Sensor/Actuator Network: I-Diagnostics; II-Validation Using Riveted Joints and Repair Patches," *Smart Mater. Struct.*, Vol. 13, 2004, pp. 609-630.

[4] Kehlenbach, M., Kohler, B., Cao, X., and Hanselka, H., "Numerical and Experimental Investigation of Lamb Wave Interaction with Discontinuities," *Proceedings of the 4th International Workshop on Structural Health Monitoring*, edited by Chang F. K., Stanford University, 2003, pp. 15-17.

[5] Mackerle, J., "Finite-element Modeling of Non-destructive Material Evaluation, an Addendum: A Bibliography (1997-2003)," *Modelling and Simulation in Material Science and Engineering*, Vol. 12, 2004, pp. 799-834.

[6] Su, Z., "Fundamental Lamb Mode-based Delamination Detection for CF/EP Composite Laminates Using Distributed Piezoelectrics," *Structural Health Monitoring*, Vol. 3, 2004, pp. 43-68.

[7] Lee, B. C. and Staszewski, W. J., "Modeling of Lamb Waves for Damage Detection in Metallic Structures: Part I Wave Propagation; Part II Wave Interactions with Damage," *Smart Mater. Struct.*, Vol. 12, 2003, pp. 804-824.

[8] Cho, Y., Hongerholt, D. D., and Rose, J. L., "Lamb Wave Scattering Analysis for Reflector Characterization," *IEEE Transactions on Ultrasonics, Ferroelectrics and Frequency Control*, Vol. 44, 1997, pp. 44-52.

[9] Mullen, R. and Belytschko, T., "Dispersion Analysis of Finite Element Semidiscretizations of The Two-dimensional Wave Equation," *Int. J. Num. Eng.*, Vol. 18, 1982, pp. 11-29.

[10] Patera, A. T., "A Spectral Element Method for Fluid Dynamics: Lamina Flow in A Channel Expansion," *J. Comput. Phys.*, Vol. 54, 1984, pp. 468-488.

[11] Dauksher, W. and Emery, A. F., "An Evaluation of The Cost Effectiveness of Chebyshev Spectral and P-finite Element Solutions to The Scalar Wave Equation," *Int. J. Num. Eng.*, Vol. 45, 1999, pp. 1099-1113.

[12] Priolo, R. G., Carcione, J. M., and Seriani, G., "Numerical Simulation of Interface Waves by High-order Spectral Modeling Techniques," *J. Acoust. Soc. Am.*, Vol. 95, 1994, pp. 681-693.

[13] Scriani, G. and Priolo, E., "Spectral Element Method for Acoustic Wave Simulation in Heterogencous Media," *Finite Elements in Analysis and Design*, Vol. 16, 1994, pp. 337-348.

[14] Komatitsch, D. and Vilotte, J. P., "The Spectral Element Method: An Efficient Tool to Simulate The Seismic Response of 2D and 3D Geological Structures," *Bulletin of the Seismologycal Society of America*, Vol. 88, 1998, pp. 368-392.

[15] Komatitsch, D., Barnes, C., and Tromp, J., "Simulation of Anisotropic Wave Propagation Based upon A Spectral Element Method," *Geophysics*, Vol. 65, 2000, pp. 1251-1260.

[16] Ostachowicz, W., Krawczuk, M., Cartmell, M., and Gilchrist, M., "Wave Propagation in Delaminated Beam," *Computer & Structures*, Vol. 82, 2004, pp. 475-483

[17] Doyle, J. F., *Wave Propagation in Structures*, Springer-Verlag, New York, 1997.

[18] Hughes, T. J. R., *The Finite Element Method: Linear Static and Dynamic Finite Element Analysis*, Prentice Hall, Englewood Cliffs, 1987.

[19] Ha, S. K., Keilers, C., and Chang, F. K., "Finite Element Analysis of Composite Structures Containing Distributed Piezoceramic Sensors and Actuators," *AIAA Journal*, Vol. 30, 1992, pp. 772-780.

[20] Roache, P. J., "Quantification of Uncertainty in Computational Fluid Dynamics," *Annual Review of Computational Fluid Dynamics*, Vol. 29, 1997, pp. 123-160.

[21] Ihlenburg, F. and Babuska, I., "Finite Element Solution of The Helmholtz Equation with High Wave Number Part II: The H-p Version of The FEM,"*SIAM Journal on Numerical Analysis*, Vol. 34, 1997, pp. 315-358.

[22] W.J. Staszewski, G. Tomlinson, C. Boller, "Health monitoring of aerospace structures: smart sensor technologies and signal processing", New York: Wile. 2003.

[23] M. Lin, X. Qing, A. Kumar, S. Beard, "SMART layer and smart suitcase for structural health monitoring applications", Proceedings of SPIE on smart structures and material systems, SPIE Optical Engineering Press, 2001.

[24] J. Blackshire, A. Cooney, "Characterizatoin of bonded piezoelectric sensor performance and durability in simulated aircraft environments", 32nd Review of progress in quantitative NDE, Brunswick, ME, 2005.

[25] J. Blackshire, S. Martin, A. Cooney, "Characterization and modeling of bonded piezoelectric sensor performance and durability in simulated aircraft environments", 3rd European workshop on structural health monitoring, Granada, Spain, 2006.

[26] J. Blackshire, V. Giurgiutiu, A. Cooney, J. Doane. "Characterization of sensor performance and durability for structural health monitoring systems", Proceeding of SPIE 12th International Symposium on Smart structures and materials, San Diego, CA, 2006.

[27] J. Blackshire, A. Cooney, "Evaluation and improvement in sensor performance and durability for structural health monitoring systems", Proceeding of SPIE 13th International Symposium on Smart structures and materials, San Diego, CA, 2006.

[28] G. Park, H. Sohn, C. Farrar, D.J. Inman, "Overview of piezoelectric impedance-based health monitoring and path forward. Schock Vibration Diagnostics, 35 (6): 451-63, 2003.

[29] D. Peair, G. Park, D.J. Inman, Improving Accessibility of the Impedance-based structural health monitoring method", Journal of Intelligent Material Systems and Structures, 15: 129-39, 2004.

[30] S. Kessler, S. Spearing, C. Soutis, "Damage detection in composite materials sing Lamb wave methods", Smart Materials and Structures, 11:269-78, 2002.
[31] V. Giurgiutiu, A. Zagrai, "Characterizatoin fo piezoelectric wafer active sensors", Journal of Intelligent Material Systems and Structures, 11:959-75, 2000.

[32] P.X. Qing, S.J. Beard, A. Kumar, P. Yu, H.L. Chan, D. Zhang, T.K. Ooi, S.A. Marotta, "Practical requirements for implementation and usage of SHM systems on aerospace structures", Proceedings of the fifth international workshop on structural health monitoring, Stanford University, CA, 1502-9, 2005.

[33] B.C. Lee, W.J. Staszewski, "Modeling of lamb wave for damage detection in metallic structures: Part II. Wave interactions with damage", Smart Materials and Structures, 12:815-24, 2003.

[34] Y. Kim, S. Ha, F.-K. Chang, "The spectral element method in time domain to analyze lamb wave propagation in structures with piezoelectric sensor networks, Unpublished.

[35] R. Dugnani, "A modified global-local analysis model of a PZT disk transducer bonded to a host structure", Proceedings of the sixth international workshop on structural health monitoring, Stanford University, CA, 859-868, 2007.

[36] S.A. Martin, J.L. Blackshire, "Effect of adhesive properties on elastic wave generation by bonded sensors", Proceedings of SPIE, 6530, 65300J, 2007.

[37] J.K. Na, J.L. Blackshire, "Investigation of Bond Quality effects on Piezoelectric sensing impact damage", Proceedings of SPIE, 6530, 653012, 2007.

[38] D.N. Kumar, S. Raja, T. Ikeda, "Active vibration control of smart plates with partially debonded multylayered PZT actuators", Smart Materials and Structures, 16:1584-1594, 2007.

[39] W. J. Staszewski, G. Tomlinson, C. Boller., "Health monitoring of aerospace structures: smart sensor technologies and signal processing", New York: Wiley; 2003.

[40] R. Seydel and F.K. Chang, "Impact identification of stiffened composite panels: II. Implementation Studies", Smart Materials and Structures, 10, 370-379, 2001.

[41] G. Lanzara, Y. Yoon, F.K. Chang, "Influence of the interface on the performance of piezoelectric elements", Unpublished.

[42] G. Lanzara, J. Feng, K. Huang, R. Dinyari, J. Y. Kim, P. Peumans, F.-K. Chang, "Stretching of a Monolithic Silicon-based Sensor Network for Large Area Embedded Structural Health Monitoring", 6th International Workshop on Structural Health Monitoring, Stanford, September 2007.

[43] K. Huang, R. Dinyari, J.Y. Kim, G, Lanzara, J. Feng, F.-K. Chang, P. Peumans, "Large-area electronics from monolithic silicon," IEDM 2007, December 2007, Washington, DC.

[44] J. N. Coleman, U. Khan, Y. K. Gun'ko, "Mechanical Reinforcement of Polymers Using Carbon Nanotubes", Advanced Materials, 18, 689-706, 2006.

[45] S. Iijima, "Helical microtubules of graphitic carbon," Nature, 354: 56, 1991.

[46] X.-Lin Xie, Y.-W. Mai, X.-P. Zhou, "Dispersion and alignment of carbon nanotubes in polymer matrix: A review", Materials Science and Engineering: R: Reports, 49, 4, 19, 89-112, 2005.

[47] E.T.Thostenson, Z. Ren, T.W. Chou, "Advances in the science and technology of carbon nanotubes and their composites: a review", Composite Science Technology, 61:1899–912, 2001.

[48] X.-Lin Xie, Y.-W. Mai, X.-P. Zhou, "Dispersion and alignment of carbon nanotubes in polymer matrix: A review", Materials Science and Engineering: R: Reports, 49, 4, 19, 89-112, 2005.

[49] E.T.Thostenson, Z. Ren, T.W. Chou, "Advances in the science and technology of carbon nanotubes and their composites: a review", Composite Science Technology, 61:1899–912, 2001.

[50] J. Liu, A.G. Rinzler, H. Dai, J. H. Hafner, R. K. Bradley, P.J. Boul, A. Lu, T. Iverson, K. Shelimov, C.B. Huffman, F. Rodriguez-Macias, Y.-S. Shon, T.R. Lee, D.T. Colbert, R.E. Smalley, "Fullerene Pipes", Science 280 1253, 1998.

[51] D. Qian, E.C. Dickey, R. Andrews, T. Rantell, "Load transfer and deformation mechanisms in carbon nanotube-polystyrene composites", Applied Physics Letters, 76, 2868, 2000.

[52] J. Sandler, M.S.P. Shaffer, T. Prasse, W. Bauhofer, K. Schulte, A.H. Windle, "Development of a dispersion process for carbon nanotubes in an epoxy matrix and the resulting electrical properties", Polymer 40, 5967, 1999.

[53] G.S. Zhuang, G. X. Sui, Z. S. Sun, R. Yang, "Pseudoreinforcement Effect of Multiwalled Carbon Nanotubes in Epoxy Matrix Composites", Journal of Applied Polymer Science, Vol. 102, 3664-3672, 2006.

[54] Y.H. Liao, O. Marietta-Tondin, Z. Y. Liang, C. Zhang, B. Wang, "Investigation of the dispersion process of SWNTs/SC-15 epoxy resin nanocomposites", Material Science Engineering A,385:175–81, 2004.

[55] K. Q. Xiao, L. C. Zhang, "Effective separation and alignment of long entangled carbon nanotubes in epoxy", Journal of Materials Science 40, 6513-6516, 2005.

[56] Y. Dror, W. Salalha, R.L. Khalfin, Y. Cohen, A.L. Yarin, E. Zussman, "Embedded Carbon Nanotubes in Oriented Polymer Nanofibers by Electrospinning", Langmuir 19, 17:7012-7020, 2003.

[57] F. Ko, Y. Gogotsi, A. Ali, N. Naguib, H. Ye, G. Yang, C. Li, P. Wills, "Electrospinning of Continuous Carbon Nanotube-Filled Nanofiber Yarns", Advanced Materials, 15, 1161-1165, 2003.

[58] R. Sen, B. Zhao, D. Perea, M.E. Itkis, H. Hu, J. Love, E. Bekyarova, R.C. Haddon, "Preparation of Single-Walled Carbon Nanotube Reinforced Polystyrene and Polyurethane Nanofibers and Membranes by Electrospinning", Nano Letters, 4, 459, 2004.

[59] J.B. Gao, A.P. Yu, M.E. Itkis, E. Bekyarova, B. Zhao, S. Niyogi, R.C. Haddon, "Large-Scale Fabrication of Aligned Single-Walled Carbon Nanotube Array and Hierarchical Single-Walled Carbon Nanotube Assembly", Journal of the American Chemical Society, 126, 16698, 2004.

[60] J.J. Ge, H.Q. Hou, Q. Li, M.J. Graham, A. Greiner, D.H. Reneker, F.W. Harris, S.Z.D. Cheng, "Assembly of Well-Aligned Multiwalled Carbon Nanotubes in Confined Polyacrylonitrile Environments: Electrospun Composite Nanofiber Sheets", Journal of the American Chemical Society, 126, 15754, 2004.

[61] T. Kimura, H. Ago, M. Tobita, "Polymer Composites of Carbon Nanotubes Aligned by a Magnetic Field", Advanced Materials, 14, 1380, 2002.

[62] E.S. Choi, J.S. Brooks, D.L. Eaton, M.S. Al-Haik, M.Y. Hussaini, H. Garmestani, D. Li, K. Dahmen, "Enhancement of thermal and electrical properties of carbon nanotube polymer composites by magnetic field processing", Journal of Applied Physics, 94, 6034, 2003.

[63] T. Takahashi, K. Yonetake, K. Koyama, T. Kikuchi, "Polycarbonate Crystallization by Vapor-Grown Carbon Fiber with and without Magnetic Field", Macromolecular Rapid Communications, 24, 763, 2003.

[64] R. Haggenmuller, H.H. Gommans, A.G. Rinzler, J.E. Fischer, K.I. Winey, "Aligned single-wall carbon nanotubes in composites by melt processing methods", Chemical Physics Letters, 330, 219, 2000.

[65] L. Jin, C. Bower, O. Zhou, "Alignment of carbon nanotubes in a polymer matrix by mechanical stretching", Applied Physics Letters, 73, 1197, 1998.

[66] L. J. Lanticse, Y. Tanabe, K. Matsui, Y. Kaburagi, K. Suda, M. Hotcida, M. Endo, E. Yasuda, "Shear-induced preferential alignment of carbon nanotubes resulted in anisotropic electrical conductivity of polymer composites", Carbon, 44, 3078-3086, 2006.

[67] E.T. Thostenson, T.W. Chou, "Aligned Multi-Walled Carbon Nanotube-Reinforced Composites: Processing and Mechanical Characterization", Journal of Physics D: Applied Physics 35 (16), L77, 2002.

[68] B. Safadi, R. Andrews, E.A. Grulke, "Multiwalled carbon nanotube polymer composites: Synthesis and characterization of thin films", Journal of Applied Polymer Science, 84, 2660, 2002.

[69] G. Lanzara, Y. Yoon, F.-K. Chang, "Carbon Nanotubes Coated Piezoelectric Actuators Part II- Testing and Characterization", Submitted.

[70] G. Lanzara, "Realization and Analysis of Carbon Nanotube Carpet Microstructures", PhD Thesis, University of Rome "La Sapienza", 2005.

[71] G. Lanzara, Y. Yoon, F.K. Chang, "Influence of interface degradation on the performance of piezoelectric actuators", Submitted.

[72] G. Lanzara, Y. Yoon, F.-K. Chang , "Carbon Nanotubes Coated Piezoelectric Actuators Part I- Design and Fabrication", Submitted.

[73] G. Lanzara, "Realization and Analysis of Carbon Nanotube Carpet Microstructures", PhD Thesis, University of Rome "La Sapienza", 2005.

[74] G. Lanzara, F.-K. Chang, "Reinforcing Piezoelectric Actuator Interface through Carbon Nanotubes", 14th International SPIE Symposium on Behavior and Mechanics of Multifunctional and Composite Materials, 18-23 Marzo 2007, San Diego, CA, Paper number: 6526-54.

[75] G. Lanzara and F.-K. Chang, "Nano-Reinforced Interfaces of Piezoelectric Actuator/Sensor Networks", 48th AIAA/ASME/ASCE/AHS/ASC Structures, Structural Dynamics and Materials Conference, 23-26 April 2007, Honolulu, Hawaii, USA. Paper number: AIAA2007-2167.

[76] K. Hsiao, J. Alms, S. Advani, "Use of epoxy/multiwalled carbon nanotubes as adhesive to join graphite fibre reinforced polymer composite," Nanotechnology, 14: 791-793, 2003.